Beta-particle Dosimetry in Radiation Synovectomy and Use of the $^{10}B(n,\alpha)$ Nuclear Reaction to Examine the Pathology of Rheumatoid Arthritis

by

Leigh Scott Johnson, S.M.

Submitted to the Department of Nuclear Engineering
in partial fulfillment of the requirements for the degree of

Doctor of Philosophy in Nuclear Engineering

at the

MASSACHUSETTS INSTITUTE OF TECHNOLOGY

May 1994

Author .....
Department of Nuclear Engineering
May 12, 1994

Certified by .....
Jacquelyn C. Yanch
Associate Professor
Thesis Supervisor

Certified by .....
Sonya Shortkroff
Thesis Reader

Accepted by .....
Allan F. Henry
Chair, Departmental Committee on Graduate Students

Beta-particle Dosimetry in Radiation Synovectomy and Use of the $^{10}B(n,\alpha)$ Nuclear Reaction to Examine the Pathology of Rheumatoid Arthritis

by

Leigh Scott Johnson, S.M.

Submitted to the Department of Nuclear Engineering
on May 12, 1994, in partial fulfillment of the
requirements for the degree of
Doctor of Philosophy in Nuclear Engineering

Abstract

Beta-particle dosimetry in radiation synovectomy, which is a radiation therapy to treat rheumatoid arthritis, was evaluated using Monte Carlo radiation transport simulation in a mathematical model of the treated joint and using experiments in joint phantoms and the knees of cadavers. Radiachromic film dosimeters and reactor-produced radionuclides were used in the experiments. Results of the dosimetry evaluation are presented as absorbed dose factors (cGy-cm^2/MBq-s) at depth in bone, articular cartilage, the fluid-filled joint capsule, and synovium, and can be used to extrapolate beta dose distributions in treated joints. Next, use of the $^{10}B(n,\alpha)$ nuclear reaction as a probe to examine the pathology of rheumatoid arthritis was developed. The approach is to use the nuclear reaction to determine whether killing the surface layer of synovial lining cells alone is sufficient to arrest the progression of RA in the joint, or whether killing the entire synovium is required. While the question was not answered here, preliminary studies of ^{10}B uptake in excised samples of human rheumatoid synovium were completed. Prompt gamma neutron activation analysis was used to demonstrate and quantify the temporal distribution of boron particulate and boric acid uptake in the samples; substantial uptake was seen to occur within the first hour of incubation. Neutron-induced alpha-track autoradiography was used to in an attempt examine the spatial distribution. Although the autoradiography experiments did not reveal the desired spatial distribution, other information was obtained.

Thesis Supervisor: Jacquelyn C. Yanch
Title: Associate Professor

Thesis Reader: Sonya Shortkroff

Acknowledgments

There are a number of individuals whose time, assistance, and support I would like to acknowledge. In particular, I would like to thank the three members of my thesis committee, Professors Jacquelyn Yanch, Otto Harling, and Sidney Yip, for the opportunities, instruction, and guidance each of them has provided me during my years as a graduate student at MIT. For always treating me with respect and for challenging and inspiring me, not only to do my best, but also to strive to improve, I thank you.

Next, I would like to acknowledge the contributions of my collaborators at Brigham and Women's Hospital, Dr. Clement Sledge, Sonya Shortkroff, and Christina. Without their help in planning and conducting the cadaver and *in vitro* experiments, much of the work in this thesis would not have been possible. Thank you for sharing your facilities, time, and experience. I look forward to continuing to work with you in the future.

I also would like to acknowledge the assistance of a number of other individuals: Dr. Guido Solares for helping me to complete the autoradiography experiments, Dr. Ronald Rogus for demonstrating the prompt gamma facility, Dr. Naengnoi Limpa-Amara for sharing her laboratory space, Brett Mattingly for the scanning electron micrographs, and my two undergraduate research assistants, Ruth Lim and Bridget Hanser, for their help in a variety of tasks.

Finally, I would like to acknowledge the support, humor, and patience of my friends, both at MIT and at home. Lisa, thank you for your help and encouragement over the past few weeks. Chris, Joe, Jason, and Andrew thank you for laughing at my jokes, putting up with my attitude, and keeping me in line. Because of you four, I know that, in the very near future, I will look back on this time in Boston and miss it dearly.

Contents

List of Figures

List of Tables

Chapter 1

Introduction

The aims of this thesis are: to evaluate beta-particle dosimetry in radiation synovectomy, which is a radiation therapy to treat rheumatoid arthritis, using Monte Carlo radiation transport simulation, experiments in joint phantoms, and experiments in the knees of cadavers; to provide a rationale for the use of the $^{10}B(n,\alpha)$ nuclear reaction to examine the pathology of rheumatoid arthritis; and to determine the temporal and spatial distribution of ^{10}B uptake in excised samples of live, human rheumatoid synovium. Presentation of the thesis is organized as follows. In this chapter, background information regarding motivation for the work is provided, and theoretical and experimental techniques used to complete it are introduced. In Chapter 2, rheumatoid arthritis and radiation synovectomy are reviewed. Rheumatoid arthritis is a painful degenerative disease affecting the synovial joints. Treatments for the disease, including radiation synovectomy, are described, as are the synovial joints and the effects of rheumatoid arthritis on those joints.

Evaluating beta-particle dosimetry in radiation synovectomy is a difficult problem for a variety of reasons (see below). The approach taken in this thesis was to evaluate the dosimetry in 3 different ways: through Monte Carlo simulation of radiation transport in a mathematical model of the rheumatoid joint, through experiments in joint phantoms using radiachromic film dosimeters and reactor-produced radionuclides, and through experiments in the knees of fresh, human cadavers using radiachromic film dosimeters and reactor-produced ^{165}Dy.

In Chapter 3, the Monte Carlo computer code used to simulate radiation transport in a mathematical joint model is introduced. `EGS4` is the code which was used, and a complete description of the code's approach to electron transport simulation is presented. In Chapter 4, use of `EGS4` as a tool to evaluate the dosimetry of 8 beta-emitting radionuclides of interest in radiation synovectomy is described. The results of the computer simulations can be used to estimate absorbed dose distributions in treated joints.

In Chapter 5, experiments aimed at verifying the accuracy of the Monte Carlo predictions of beta-particle dosimetry in radiation synovectomy are presented. As mentioned above, experiments were conducted in both joint phantoms and the knees of cadavers using radiachromic film dosimeters and reactor-produced radionuclides. Comparisons of the experimental results with the EGS4 results are made.

In the remainder of the thesis, the focus is shifted from beta-particle dosimetry in radiation synovectomy to use of the $^{10}B(n,\alpha)$ nuclear reaction to examine the pathology of rheumatoid arthritis. Chapter 6 is devoted to presenting data which support the hypothesis that killing the surface layer of synovial lining cells in rheumatoid joints is sufficient to temporarily arrest the progression of rheumatoid arthritis in the joint and provide patients with symptomatic relief of the disease. Use of the $^{10}B(n,\alpha)$ nuclear reaction as a probe to test the hypothesis is developed. The $^{10}B(n,\alpha)$ nuclear reaction was chosen specifically because the range of the emitted particles is short, on the order of 10 μm. The reaction thus can be used to selectively damage and kill only boronated cells and their nearest neighbors. While the hypothesis itself is not tested in this thesis, preliminary studies of ^{10}B uptake in excised samples of live, human rheumatoid synovium are presented in Chapter 7. Prompt gamma neutron activation analysis is used to quantify the temporal distribution of ^{10}B uptake in the samples, while neutron-induced alpha-track autoradiography is used in an attempt to determine the spatial distribution.

Finally, in Chapter 8 important conclusions drawn from the work of this thesis are reviewed and recommendations for future research are made. The recommendations include descriptions of *in vitro* and *in vivo* experiments aimed at determining the thickness of synovium which must be killed to arrest the progression of rheumatoid arthritis and provide patients with symptomatic relief of the disease, *i.e.*, is it sufficient to kill only the lining cells or must the entire synovium be killed. The possible development of neutron capture therapy as novel treatment for the disease also is presented.

1.1 Beta-particle Dosimetry in Radiation Synovectomy

Radiation synovectomy is a radiation therapy to treat rheumatoid arthritis, a painful, degenerative disease affecting the synovial joints. The procedure consists of the injection of a short-lived, low-energy beta-emitting radionuclide into the joint capsule where it comes into direct contact with the diseased tissue (rheumatoid synovium) [1]. Phagocytic cells along the tissue surface quickly absorb radioactive particulate from the joint capsule [2, 3, 4]. Then as the radionuclide decays, radiation absorbed dose is imparted to the rheumatoid synovium. Provided the amount of radioactivity injected

is sufficiently large to deliver a therapeutic dose to the tissue, it will be killed. Tissue which regenerates over time is expected to be free of disease for 2 to 5 years, and the progression of rheumatoid arthritis in the joint is thereby temporarily arrested [1].

It is important to realize from the start that there is no cure for rheumatoid arthritis and that the radiation therapy—like other treatments—is aimed instead at slowing the progression of the disease and relieving its signs and symptoms. Up to 100% of patients treated with radiation synovectomy are reported to experience relief of pain, reduced joint swelling, and increased joint mobility at 6 months, 1 year, and 2 years after injection [5]. Improvement however is dependent on a variety of factors, including the condition of the joint before treatment and whether or not a therapeutic radiation dose is delivered to all the rheumatoid joint tissue. At the same time, one wants to ensure that other, healthy, joint components located nearby (*e.g.*, bone and articular cartilage) are not subjected to an unnecessary radiation hazard. It is for these reasons that beta-particle dosimetry in radiation synovectomy is of interest. Before discussing approaches to beta-particle dosimetry however, it is instructive to review the concept of absorbed dose and the role of dosimetry in radiation therapy.

Concept of absorbed dose

The ultimate radiobiological effects of beta-emitting radionuclides injected into rheumatoid joints are initiated by processes in which atoms and molecules of the joints' tissues are ionized or excited. Some of the ionization events result in the production of chemically active species, *i.e.*, free radicals, in regions near the paths traversed by the emitted particles. Free radical production is the direct result of energy deposition in the tissues and their presence is recognized as playing a central role in the generation of a wide variety of biological damage, and other changes, from which subsequent radiobiological effects evolve. In general, as the number of ionization events increases, so does the production of free radicals, and therefore the production of biological damage.

Over a wide range of conditions, it is considered an excellent approximation to assume that the average number of ionizations and excitations in the volume of interest is proportional to the amount of energy deposited in the volume [6]. The absorbed dose, *i.e.*, the average amount of energy imparted per unit mass, therefore is of central importance for the production and evaluation of the radiobiological effects of radiation synovectomy.

Role of dosimetry in radiation therapy

The role of dosimetry in radiation therapy is to provide quantitative information regarding absorbed dose distributions in patients. In particular, it is of interest to know accurately the absorbed dose imparted to target tissues and whether or not

the incidental irradiation of other, "non-target," tissues subjects the patient to an unnecessary or undesirable radiation hazard. In beta-particle dosimetry in radiation synovectomy, the target tissue is rheumatoid synovium, and the other, non-target, tissues to be considered include bone and articular cartilage.

In general, there are 3 methods for estimating absorbed dose distributions in radiation synovectomy or any other radiation therapy. These include: (1) direct measurement in humans, (2) extrapolation from measured data in animals, phantoms, and cadavers, and (3) calculations based on mathematical models. Estimates of absorbed dose distributions also can be extrapolated from clinical results, but this "empirical" method lacks scientific rigor and is not considered here.

1.1.1 Calculations based on mathematical models

Typically in radiation dosimetry, the ranges of beta particles emitted from internally distributed radionuclides are small compared to the size of the tissues or organs containing the radioactivity. When this is the case, it has been considered permissible to assume that the entire kinetic energy of the emitted particles is deposited in the source [6]. This clearly is not a reasonable assumption in radiation synovectomy, however, since the ranges of the emitted beta particles (up to 10 mm depending on the radionuclide [1, 7, 8]) is large compared to the size of the source (less than 1 mm [9, 10, 11]). In addition, the radiation absorbed dose to other, "non-source," regions of the joint (*e.g.*, synovium at depth, bone, and articular cartilage) also are of interest in radiation synovectomy. Alternative approaches therefore must be used.

For beta-particle sources located at *or near* target tissues, beta dose point kernels have been developed to represent the distribution of absorbed dose in a tissue medium as a function of distance from a point-isotropic beta-emitting source. By suitable integration over the point kernels, dose distributions can be readily determined for a wide variety of source-to-target configurations.

The approach is best illustrated with the aid of an example. In 1973, Husak *et al.* [9] used the beta dose point kernel method to calculate beta-particle dosimetry in radiation synovectomy. Their approach was to assume that radionuclides injected into the rheumatoid joint are absorbed by the synovial surface and are uniformly distributed over it so that they form a thin plane source of activity.

The absorbed dose rate R (rad/s) at a distance s from a thin plane source of finite thickness d then is calculated as:

$$R(s) = \frac{1}{d}\int_{s}^{s+d} R_p(z)\,\mathrm{d}z, \tag{1.1}$$

where $R_p(z)$ is the absorbed dose rate at distance z from an infinitely thin plane

source of uniformly distributed beta-particles and is given by:

$$R_p(z) = 2\pi\sigma nkE_{avg}\int_z^{R_{max}} x\phi_\beta(x)\,\mathrm{d}x, \tag{1.2}$$

where σ is the number of disintegrations per cm^2 per second, n is the number of beta-particles emitted per disintegration, k is 1.6×10^{-8} g-rad/MeV, E_{avg} is the average energy of the emitted beta-particles (MeV), and R_{max} is the penetration range in tissue of the most energetic beta-particle emitted (cm). The symbol $\phi_\beta(x)$ represents the point isotropic specific absorbed fraction, *i.e.*, the fraction of the energy emitted from a point isotropic source that is absorbed at distance x per unit mass of tissue.

The specific absorbed fraction can be calculated using tabulated values of the dimensionless scaled absorbed dose distribution function $F_\beta(\xi)$ [12]. The function $F_\beta(\xi)$ and the specific absorbed fraction are related as follows:

$$F_\beta(\xi) = 4\pi\rho x^2 x_{90}\phi_\beta(x), \tag{1.3}$$

where $\xi = x/x_{90}$, x_{90} is the distance from the point isotropic source at which 90% of the emitted energy is absorbed (cm), and ρ is the density of the medium (g/cm^3). Now, if the expression $2\pi x\phi_\beta(x)$ in Eqn. 1.2 is replaced with $F_\beta(\xi)/2\rho x x_{90}$, the resulting expression is as follows:

$$R_p(z) = \frac{1}{2\rho x_{90}}\sigma nkE_{avg}\int_z^{R_{max}} \frac{F_\beta(\xi)}{x}\mathrm{d}x. \tag{1.4}$$

This equation can be solved by numerical integration using tabulated values of the function $F_\beta(\xi)$ [12].

Husak *et al.* have solved the equation. Their results present the dependence of absorbed dose in tissue on distance (up to 0.6 mm) from thin plane sources of ^{198}Au and ^{90}Y, two radionuclides which have been used extensively in clinical trials in radiation synovectomy (see Chapter 2).

But the point kernel method has been developed for homogeneous media only. As a consequence, the approach taken by Husak *et al.* was to approximate the joint as a homogeneous soft tissue volume and to neglect the incidental irradiation of other joint components, such as bone and articular cartilage. Doses to these other, "non-target," joint components were not calculated. As mentioned above however, one of the roles of dosimetry in radiation therapy is to provide the quantitative information necessary for radiotherapists to ensure that non-target tissues are not subjected to an unnecessary or undesirable radiation hazard. Doses to bone and articular cartilage in radiation synovectomy therefore must be considered. Absorbed dose to the bone surface (10 μm) is particularly of interest since the International Commission on Radiation Protection (Vienna, Austria) has identified this tissue region as one

of two principal radiosensitive targets to be protected in procedures involving bone irradiation [13].

In addition, the tabulated beta dose point kernels referenced above and used by Husak *et al.* to calculate beta dosimetry in radiation synovectomy are based on a model which neglects the production and transport of secondary electrons and the fluctuation of energy loss with distance [14, 15]. Prestwich *et al.* have reported Monte Carlo calculations of beta dose point kernels that do include the transport of secondary electrons and the effects of energy fluctuations [14]. Their approach shows a dose distribution for ^{90}Y in water that is 7% lower at the origin than that predicted by the above methods and significantly higher at distances greater than 5 mm from the source. While these results have shown improved agreement with experiment, a systematic error in the energy-loss straggling algorithm has been revealed [15], indicating yet another limitation of the accuracy of the point kernel method.

1.1.2 Other methods

As mentioned above, other methods for estimating absorbed dose distributions in radiation therapy are available. These include direct measurements in humans, which often can be difficult to obtain (see Chapter 5), and extrapolation from measured data in animals, phantoms, and cadavers. Other mathematical methods, *e.g.*, the Monte Carlo method, also can be used. The approach taken in this thesis was to evaluate beta-particle dosimetry in radiation synovectomy 3 different ways.

First, Monte Carlo simulations of radiation transport in a mathematical model of the rheumatoid joint were completed for 8 radionuclides of interest in radiation synovectomy. Each of these radionuclides either has been used in clinical trials or is of interest due to its favorable half-life, emission energies, and radiochemistry. Simulation begins by choosing a starting position, direction, and energy for the emission of a single beta-particle from within the radiation source region. The emitted particle is transported through the mathematical joint model by the Monte Carlo computer code. At each point in the particle's "life" where a choice of interaction type, scattering direction, distance to the next interaction, etc. has to be made, a random number is generated by the code and used to determine the event's outcome from known probability distributions which describe the likelihood of occurrence of each of the possible outcomes. Simulated interactions include all the major events, such as the production of secondary "knock-on" electrons and bremsstrahlung photons. "Continuous" energy loss and multiple scattering through minor interactions with atomic electrons also are accounted for. Simulation ends when the emitted beta-particle and all its secondaries no longer have enough energy to excite the absorbing media. At this point, a new beta-particle is "emitted" from within the radiation source region, and the process is repeated. The simulations are described in detail in Chapter 4.

Second, experiments were conducted in joint phantoms using radiachromic film dosimeters and reactor-produced radionuclides. The joint phantoms were built using aluminum as a substitute for bone and solid water (a specially formulated, commercially available plastic) as a substitute for soft tissue and articular cartilage. Both soft tissue and articular cartilage are composed primarily of water and their radiation absorption and scattering characteristics are well simulated with water substitutes. Planar radioactive sources of uniform activity (similar to those assumed by Husak *et al.* to exist in joints treated with radiation synovectomy) were made by soaking filter papers in liquid solutions of Dy_2O_3 (stable, natural Dy) and Ho_2O_3 (stable, natural Ho) dissolved in nitric acid. The wet filter papers then were dried, stacked and stitched together, and irradiated at the MIT Nuclear Reactor Laboratory, yielding thin plane sources of ^{165}Dy and ^{166}Ho which were inserted into the joint phantoms and allowed time to decay. Radiachromic film dosimeters were used to measure depth-dose data in the phantom. The experiments, dosimeters, and results are explained in detail in Chapter 5.

Third, experiments were conducted in the knees of fresh, human cadavers using radiachromic film dosimeters and reactor-produced ^{165}Dy. The knees were surgically opened and several dosimeters were stitched into strategic locations throughout the joints. The knees then were sewn tight and injected with a therapeutic dose of radioactivity. After allowing time for decay, the knees were reopened and the dosimeters were removed for analysis. These experiments also are explained in detail in Chapter 5.

1.2 Use of the ^{10}B(n,α) Nuclear Reaction to Examine the Pathology of Rheumatoid Arthritis

In Chapter 6, the focus of the thesis is shifted from beta-particle dosimetry in radiation synovectomy to the use of the ^{10}B(n,α) nuclear reaction to examine the pathology of rheumatoid arthritis. For the most part, radiation synovectomy can be described as attempting to kill the entire synovial membrane. Existing data suggest, however, that removal of only the surface layer of lining cells may be sufficient to arrest the progression of rheumatoid arthritis and provide patients with temporary, symptomatic relief of the disease. These data are presented in Chapter 6, along with a series of experiments aimed at testing the above hypothesis.

The proposed approach is to selectively irradiate and kill either the lining cells alone or the entire synovium using the ^{10}B(n,α) nuclear reaction. This reaction was chosen specifically because the range of the high-LET particles emitted is very short,

on the order of 10 μm. As a consequence, the resulting radiation damage is very cell-specific, restricted only to boronated cells and their nearest neighbors. While these experiments have not been attempted in this thesis, preliminary studies of ^{10}B uptake in excised samples of live, human rheumatoid synovium were completed.

Samples of rheumatoid synovium obtained from the operating room were incubated with either boron particulate or boric acid for varying periods of time. The boron particulate is hypothesized to be absorbed by the surface layer of lining cells only. These lining cells are phagocytic and have been shown to actively absorb a wide variety of particulate matter injected into synovial joints [2, 3, 4]. The boric acid, on the other hand, is a water soluble compound; and like other water soluble compounds, it is expected to diffuse freely and rapidly throughout the entire synovial membrane. Prompt gamma neutron activation analysis was used to quantify the temporal distribution of bulk ^{10}B uptake by human rheumatoid synovium, for both boron preparations. Neutron-induced alpha-track autoradiography was used to determine the spatial distribution. The experiments and results are presented in Chapter 7.

Finally, in Chapter 8 important conclusions drawn from the thesis are reviewed and recommendations for future work are made. In particular, *in vitro* and *in vivo* experiments aimed at determining the thickness of rheumatoid synovium which must be removed for successful therapy are presented. The possible development of neutron capture therapy as a novel treatment for rheumatoid arthritis also is described.

1.3 Conclusion

The aims of this thesis are: to evaluate beta-particle dosimetry in radiation synovectomy using Monte Carlo radiation transport simulation, experiments in joint phantoms, and experiments in the knees of cadavers; to provide a rationale for the use of the ^{10}B(n,α) nuclear reaction as a probe to examine the pathology of rheumatoid arthritis; and to determine the temporal and spatial distribution of ^{10}B uptake in excised samples of human rheumatoid synovium.

In this chapter, the framework of the thesis was outlined, and the theoretical and experimental techniques used to complete it were introduced. In the next chapter, rheumatoid arthritis and radiation synovectomy are reviewed.

Chapter 2

Rheumatoid Arthritis and Radiation Synovectomy

2.1 Introduction

One of the oldest diseases known to affect humans, rheumatoid arthritis is a chronic, autoimmune disease characterized by recurrent swollen, inflamed, and painful joints. Although rheumatoid arthritis has many clinical manifestations, its distinguishing characteristic is a persistent inflammation of the tissue (synovium) which lines the joint. Treatment is generally aimed at relieving the inflammation. In some patients, however, the inflammation may prove unresponsive to the conventional modes of treatment; and the synovium instead may be removed, or killed. Radiation synovectomy has been developed as an effective, quick, and low-cost means of killing rheumatoid synovium.

In this chapter the effects of rheumatoid arthritis on synovial joints are described. Conventional treatments for the disease are reviewed, and radiation synovectomy is introduced. Discussions of the importance of understanding beta dosimetry in radiation synovectomy and determining the thickness of tissue which must be removed for successful treatment also are included.

2.2 Synovial Joints

The joints of the human body often are classified into two main functional groups: synovial and non-synovial. The synovial joints comprise the majority of the body's articulations and are characterized by the extensive, almost frictionless movement of bones upon one another. Examples of synovial joints include the knee, shoulder, and hip. The non-synovial joints, *e.g.*, the suture joints of the skull, provide only limited

movement, if any.

2.2.1 Anatomy

In the synovial joint, the ends of the two articulating bones are ensheathed by a strong fibrocollagenous capsule and are separated from each other by a capillary thin layer of a highly viscous fluid, the synovial fluid. As shown in Fig. 2-1, the fluid is contained within a capsule that is defined by a specialized secretory epithelium, the synovium. Synovium lines the capsule everywhere except over the ends of the articulating bony surfaces [16].

The ends of the two bones are covered with a thin layer (0.5 to 3 mm depending on the size of the joint [17, 18]) of smooth, spongy articular cartilage. The articular cartilages are the actual load bearing surfaces of the joint and thus are designed to resist the repetitive rubbing and considerable deformation to which they are subjected over the years. Synovial fluid serves as a lubricant for the cartilages.

Structures around the joint, which provide strength, support, and stability, include collagenous ligaments and tendinous muscle attachments. In some complex joints (*e.g.*, the knee) there are also internal ligaments to prevent overstretching or twisting and fibrocartilaginous menisci to stabilize and guide gliding movements.

2.2.2 Synovium

Principal among structures found in synovial joints, the synovium performs at least three main functions. It provides an unobtrusive, low-friction lining for the joint. It is responsible for secreting and maintaining the lubricating synovial fluid. And it plays an important role in maintaining joint stability.

Synovium is composed of collagen fibers, elastic fibers, and synovial lining cells [19]. The collagen and elastic fibers form a wide-meshed network along the synovial surface and continue into the interior of the membrane where they are connected to underlying, loose connective tissues. Cauliflower-like protrusions of synovial lining cells near the surface emerge from beneath the superficial fibers.

Synovial lining cells often are divided into two major cell types, the macrophage-like type-A cells and the fibroblast-like type-B cells [19]. Type-A cells are phagocytic, *i.e.*, they have the ability to engulf and destroy particulate matter, as shown in Figure 2-2. These cells have elongated bodies and send processes mostly toward the joint capsule where they emerge and are available to remove waste from the synovial fluid. Type-B cells are secretory. They also send processes toward the joint capsule, and evidence has shown that these cells secrete proteoglycans and hyaluronic acid which play important roles in the metabolism of synovium and in the formation of synovial fluid. In some areas, both type-A and type-B lining cells may be absent.

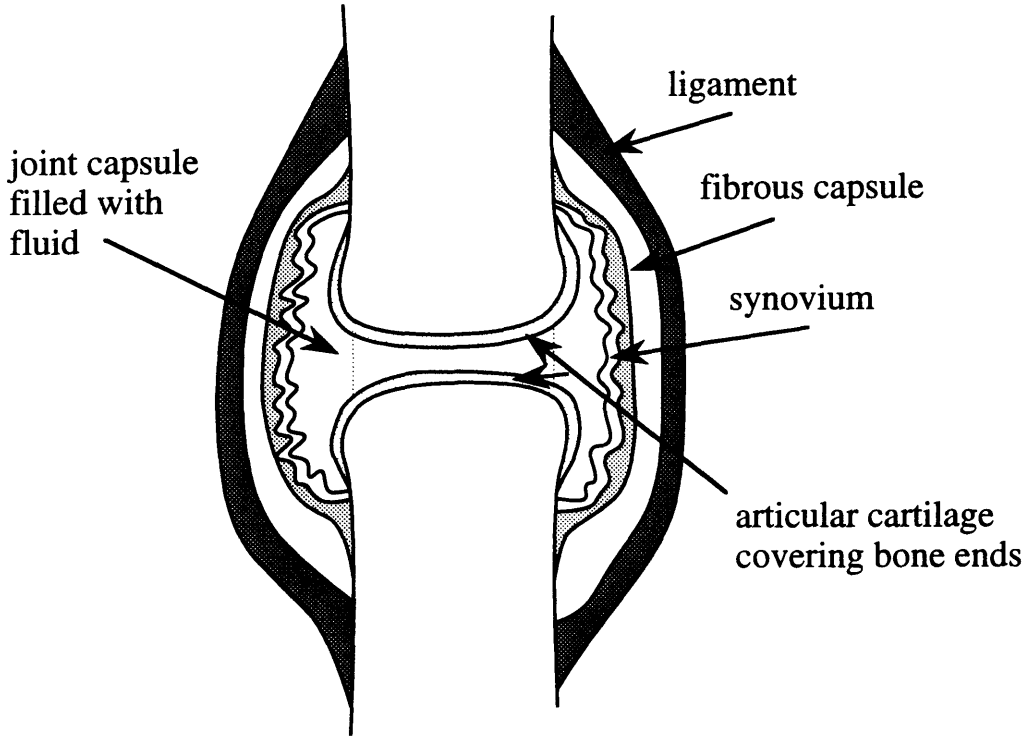

Figure 2-1: Diagram of a simple synovial joint showing the ends of the two articulating bones separated from each other by synovial fluid which is contained within the joint capsule.

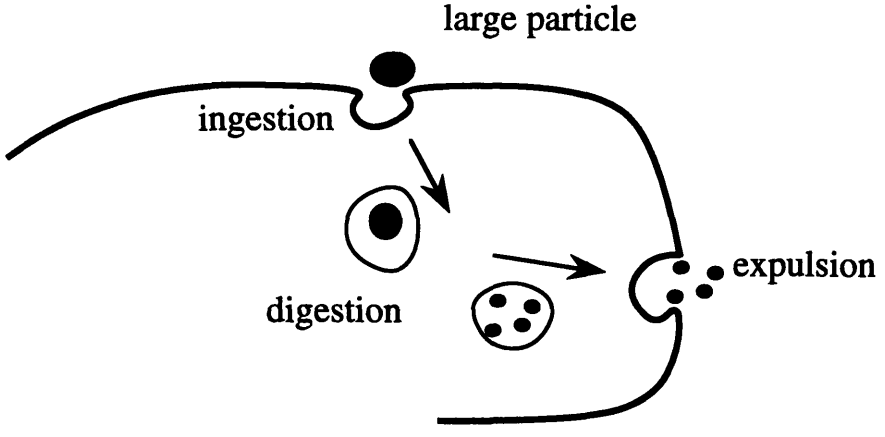

Figure 2-2: Phagocytosis refers to the process in which a cell's plasma membrane infolds around a large particle and forms a vesicle which then moves into the cell. The ingested particles typically are digested and expelled.

At these points, the underlying, loose connective tissue is exposed directly to the synovial fluid.

Other cells found in the synovium include mast cells, a variable number of fat cells, and fibroblasts, which are cells capable of generating collagen fibers. In addition, an abundant supply of capillaries and nerve fibers runs through the mesh of collagen and elastic fibers and underlying connective tissue [19].

2.3 Rheumatoid Arthritis

Rheumatoid arthritis is a chronic, autoimmune disease affecting the synovial joints. While its precise etiology remains a mystery, rheumatoid arthritis is known to begin as a persistent inflammation of the synovium [20, 21]. If left untreated, the inflammation eventually leads to significant pain, deformation, and disability. Despite its destructive potential, the course of rheumatoid arthritis can be quite variable. Some patients may experience only mild symptoms with minimal joint damage, while others may suffer relentless, progressive rheumatoid arthritis with marked deformity in several joints. Most patients will experience an intermediate course [20, 21].

2.3.1 Epidemiology

Approximately 1% of the adult population is affected by rheumatoid arthritis [21]. Women are affected approximately three times more often than men. The prevalence increases with age, and differences between the sexes diminish in the older age groups. Rheumatoid arthritis is seen throughout the world and affects all races. Onset of the disease typically is during the fourth or fifth decade of life, with 80% of all patients developing rheumatoid arthritis between the ages of 35 and 50 [21]. A small proportion eventually become severely disabled.

The first criteria for the classification of the disease were published in 1958. These criteria were used heavily for 30 years and then revised in 1988 [22]. Designed primarily for epidemiologic purposes and not for the diagnosis of individual cases, the criteria are intended to be useful guidelines for identifying the disease. They include: morning stiffness in and around joints lasting at least one hour before maximal improvement; swelling of the tissue around three or more joints; swelling of the proximal interphalangeal (finger), metacarpophalangeal (hand), or wrist joints; symmetric joint swelling; subcutaneous nodules; a positive test for rheumatoid factor; and radiographic evidence of bone erosions. To make a diagnosis of rheumatoid arthritis, at least the first four symptoms must have been present for six or more weeks [22].

2.3.2 Pathology

The precise cause of rheumatoid arthritis is unknown. Indeed, it is probable that many different stimuli can activate the inflammatory response, and more is known about the genetic susceptibility of individuals to the disease than about causitive agents. In any event, rheumatoid arthritis is known to begin as an inflammation of the synovium. Inflammation is a defense mechanism which aims to protect the host tissue from foreign invaders. Synovial inflammation which is allowed to persist over time, however, leads to a number of destructive structural changes in the joint. Development of the disease can be summarized as follows.

Onset

The first cells to be involved in the immune response are antigen-presenting cells, *e.g.*, macrophages or dendritic cells in the synovium. The antigen-presenting cells ingest, process, and present foreign protein antigens to the circulating T-lymphocytes of the immune system. The T-lymphocytes, in turn, initiate a cellular immune response and stimulate the differentiation of B-lymphocytes into antibody-secreting plasma cells.

Progression

As the immune response becomes organized, the increase in the number of T-cells, B-cells, and secreted antibodies evolves within an expanding scaffold of new blood vessels and an intensely active layer of highly proliferative synovial lining cells. The development of new blood vessels in the synovium is essential to the progression of rheumatoid arthritis, since they facilitate the delivery of nutrients to the rapidly increasing number of lining cells.

Each of the steps in the above progression is mediated by the presence of cytokines, which are small proteins secreted by the lining cells, immunocytes, and macrophages. While cytokines are known to have the ability to affect gene expression in cells, their activities are complex and poorly understood [21]. For example, one cytokine may stimulate the proliferation of cells under some conditions but inhibit its growth under others. Cells identified as targets of one cytokine also may be the cells responsible for secreting other cytokines. Different cytokines may serve similar functions, and their interactions may be synergistic, additive, or inhibitory. In spite of this complexity, there is little argument that cytokines play a central role in the amplification and perpetuation of chronic synovial inflammation and, as a consequence, in the eventual destruction of bone and articular cartilage [23].

Destruction

The precise mechanism by which bone and articular cartilage destruction occurs has yet to be completely resolved. Although the synovial fluid contains a number of enzymes potentially able to destroy bone and articular cartilage, the majority of the destruction typically occurs when the proliferating synovium becomes sufficiently organized to invade the affected joint. The organization is characterized by what often is referred to as an extravagant growth of synovial lining cells. The result is the development of an offensive front of tissue, which grows to form slender finger-like projections, or "pannus." Behaving much like a localized neoplasm, the developing pannus eventually grows to protrude into the joint capsule where it spreads to cover the articular cartilages [21].

Activated by the presence of various cytokines, the large number of synovial lining cells in the invading pannus begin to secrete high concentrations of enzymes capable of destroying articular cartilage and bone. It is important to realize that very little gross destruction of articular cartilage is necessary before its normal function is weakened to the point that progressive, irreversible disintegration follows in response to the normal movements of weight-bearing joints. Over time the disintegration can lead to the complete loss of articular cartilage in some areas, leaving the underlying subchondral bone exposed and vulnerable to erosion.

Once destruction of the articular cartilages is well underway, attempts to protect

Table 2.1: The histopathologic stages of rheumatoid arthritis. Adopted from Harris.

Stage	Pathology	Symptoms
1	Presentation of antigen to T cells	None
2	T cell, B cell, and vascular proliferation	Malaise, mild stiffness and swelling
3	Synovial proliferation without pannus,	Joint pain and swelling, morning stiffness, malaise and weakness
4	Formation of pannus, degradation of cartilage by enzymes	Same as stage 3
5	Erosion of bone, invasion of cartilage by pannus	Same as stage 3, loss of function and early deformity

affected joint from progressive, irreversible degradation generally are considered to be futile [23]. Treatments thus are aimed at delaying the onset of articular cartilage destruction, primarily through the relief of synovial inflammation. The above stages of rheumatoid arthritis are reviewed in Table 2.1 [21].

2.3.3 Treatment

The goals of treatment of rheumatoid arthritis are: (1) relief of pain, (2) reduction of inflammation, (3) preservation of joint function, (4) inhibition of the pathologic process, and (5) facilitation of healing [23]. There is a wide variety of medications available which are capable of providing pain relief and some reduction in inflammation in most patients. None of the medications are curative, and therefore all must be viewed as palliative, *i.e.*, aimed at relieving the signs and symptoms of the disease.

Medical management of rheumatoid arthritis involves 3 general approaches. The first is the use of aspirin and other nonsteroidal antiinflammatory drugs (*e.g.*, ibuprofen, fenoprofen, naproxen, and sulindac) to control the local inflammatory process. While these drugs are rapidly effective at alleviating the signs and symptoms of rheumatoid arthritis, they appear to have little effect on the progression of the disease. They also are associated with a wide spectrum of toxic side effects. Elderly patients are particularly at risk for certain toxic effects. None of these drugs has been shown to be more effective than aspirin in the treatment of rheumatoid arthritis [23].

The second approach is the use of disease-modifying drugs which appear to have the capacity to decrease elevated levels of certain reactants in treated patients and

thus are thought to modify the destructive capacity of the disease. This group includes gold compounds, D-penicillamine, antimalarials, and sulfasalazine. Unfortunately, each of these drugs is associated with considerable toxicity and, as a result, require careful patient monitoring. In addition, these drugs appear to have minimal antiinflammatory effects and therefore must be used in combination with the first group of drugs. It has been reported that as many as two-thirds of patients develop some clinical improvement after therapy with disease-modifying drugs [23]. Despite this result, there is minimal evidence that they actually delay the long-term development of bone erosions and the eventual loss of joint structure and function [23].

The third approach is the use of immunosuppressive and cytotoxic drugs. These have been shown to be effective in some patients, yet no more so than the disease-modifying drugs. They also appear to predispose some patients to the development of malignant tumors [23], and as a consequence, these drugs have been reserved for patients who have clearly failed to respond to other forms of treatment.

At the onset of disease, it is difficult to predict the natural course an individual patient's illness will take. The usual approach thus is to attempt to relieve the patient's symptoms and synovial inflammation with nonsteroidal antiinflammatory drugs. Some patients may have mild rheumatoid arthritis that requires no additional treatment. Other patients however may have symptoms that cannot be controlled adequately with this group of drugs.

At some point in *most* patients' course of illness, the use of nonsteroidal antiinflammatory drugs proves to be insufficient, and the use of disease-modifying drugs is entertained. It must be kept in mind however that all disease-modifying drugs essentially provide what can be described as an immuno-suppressive effect and require prolonged administration. Even with a successful response to the use of disease-modifying drugs, occasional synovial inflammation may persist in a limited number of joints in some patients; and problems associated with progressive loss of articular cartilage, bone erosions, or deformity may require additional treatment. As mentioned above, use of the third group of drugs generally is reserved only for the most severe cases, in which the possible delay of complete joint destruction is believed to outweigh the risk of inducing cancer.

In patients whose joints already have been severely damaged by progressive rheumatoid arthritis, drug treatments alone may prove insufficient. For relief of pain or modest functional improvement, some patients elect to have joint surgery. Total joint replacements, for instance, can be done on a number of joints, with the most successful procedures primarily carried out on hips and knees.

In addition, surgical synovectomy has proven to be useful in some patients with persistent rheumatoid arthritis in a single joint, especially the knee [24]. The procedure entails opening the joint to surgically remove the inflamed synovium and thereby

provide the patient with symptomatic relief of rheumatoid arthritis for 2 to 5 years [25]. Surgical synovectomy is however unavoidably associated with a variety of risks and disadvantages: from infection, hemorrhage, and anesthesia to the high cost of hospitalization and painful rehabilitation. In addition, it is technically difficult, if not impossible, to remove all the inflamed synovium lining the joint. It is for these reasons that alternative methods of treatment are desirable.

2.4 Radiation Synovectomy

Radiation synovectomy has been developed as an effective, low-cost alternative to surgery for patients who have proven unresponsive to the traditional modes of treatment [7, 8]. The procedure consists of the injection of a short-lived, low-energy beta-emitting radionuclide directly into the joint capsule where it is free to mix with the synovial fluid and migrate throughout the joint, as shown in Fig. 2-3. Phagocytic lining cells along the synovial surface quickly absorb some of the radioactive particulate from the capsule. Then as the radionuclide decays, kinetic energy is deposited in the rheumatoid synovium. Provided the amount of activity injected is sufficient to deliver a therapeutic dose to the tissue, it will be killed. Resulting histologic changes include regression of destructive pannus, reduced production of destructive enzymes and proinflammatory cytokines, and eventually sclerosis of the synovium [1]. The expectation is that the treated joint will be free of disease, at least temporarily, and the pain and symptoms of rheumatoid arthritis thereby temporarily alleviated.

Advantages over surgery include an increased likelihood of removing all the inflamed synovium, a reduced potential for the formation of blood clots and infection, a requirement for local anesthesia only, and the fact that the radiation treatment is much less costly and time consuming (see Table 2.2). Results of clinical trials, in general, are equally as appealing, with improvement having been reported in up to 100% of treated joints [5]. As with surgery however, the treatment is not curative and is aimed instead at relieving the pain and symptoms of rheumatoid arthritis. Since the inflamed synovium itself is removed, rather than the offending agent, the symptoms of the disease typically are expected to return, often within 2 to 5 years [26]. At which time, patients can be reinjected [27].

Radiation synovectomy is regularly practiced in Australia and Canada, and additionally used in a few European centers. On a global basis, it is not extensively performed. And in the US, the technique is virtually nonexistent. Resistance generally is held to be due primarily to concerns about excessive extraarticular irradiation due to leakage of radioactivity from the joint [7].

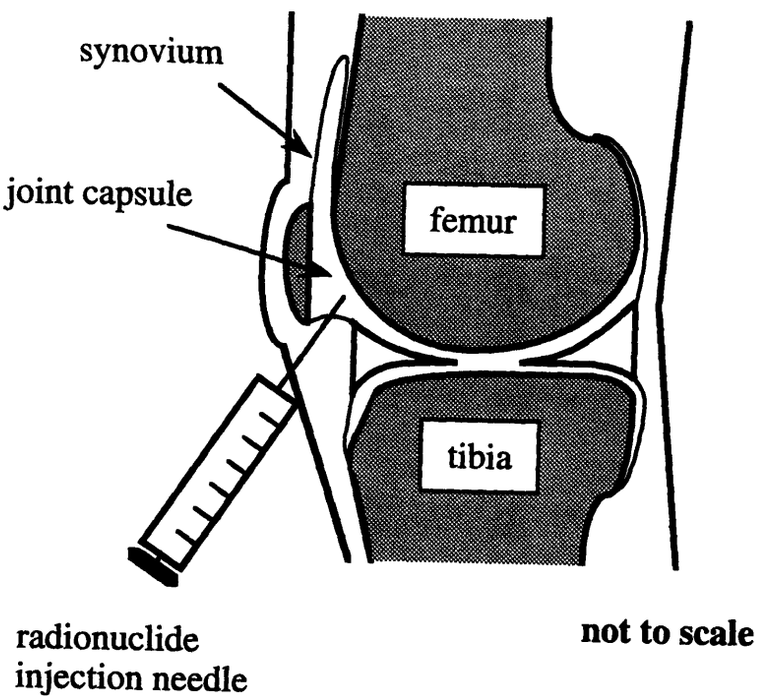

Figure 2-3: In radiation synovectomy, a beta-emitting radionuclide is injected directly into the joint capsule in order to kill rheumatoid synovium.

Table 2.2: Radiation synovectomy versus surgery. Adopted from Harling *et al.*

Item	Radiation synovectomy	Surgery
Cost	$2000-5000	$20,000-30,000
Time	Weeks to rehabilitate	Months with some hospitalization
Relief	2-5 y symptomatic relief	Same
Dangers	Extraarticular irradiation, radiation damage in healthy joint components	Infection, hemorrhage, anesthesia

Table 2.3: Radionuclides of interest in radiation synovectomy

Radionuclide	Max Energy	Half-life
^{32}P	1.71 MeV	346 h
^{90}Y	2.25	64.2
^{153}Sm	0.80	46.8
^{165}Dy	1.28	2.3
^{166}Ho	1.85	27
^{186}Re	1.07	90
^{188}Re	2.12	16.8
^{198}Au	0.96	64.8

2.4.1 Radionuclides of interest

Radionuclides of interest in radiation synovectomy are listed in Table 2.3. These 8 beta-emitters either have been used in clinical trials or are of interest due to their favorable half-lives, emission energies, and radiochemistry.

In the past, the "ideal" radionuclide for the treatment has been considered to be a short-lived low-energy beta-emitter with little or no coincident gamma-ray emission. Low-energy beta particles have been desirable because they typically deposit all of their kinetic energy within a few mm of tissue or less, a thickness which is on the order of the thickness of rheumatoid synovium. Short physical half-lives have been desirable since leakage of radioactivity from the joint requires time, and atoms which decay before leaking do not subject the patient to unnecessary extraarticular irradiation.

Before injection, these radionuclides usually are attached to larger molecules or particles to limit leakage of activity from the joint. The larger molecules or particles must be small enough to be phagocytized, but not so small as to allow rapid biological removal from the joint. The most appropriate size range is generally considered to be 2 to 5 μm [28]. In addition, the particles should be biodegradable and easily removed from the joint after radioactive decay.

In the past, the radiopharmaceuticals most commonly injected have been inorganic colloids. Unfortunately, leakage of these colloids from the joint has sometimes led to significant radiation doses to the liver, spleen, and draining inguinal lymph nodes [29]. Recent advances in radiopharmaceutical design and synthesis, however, could eventually lead to the generation of a new class of radiation synovectomy agents which will exhibit minimal leakage of activity from the treated joint [30, 31]. In the remainder of this section, previous clinical trials in radiation synovectomy using ^{198}Au, ^{90}Y, ^{32}P, and ^{165}Dy are discussed.

^{198}Au

The first radionuclide to be injected into rheumatoid joints was ^{198}Au (in Vienna, Austria in 1952) [32]. The decay of ^{198}Au results in the emission of a beta-particle (maximum energy 0.96 MeV) 98.6% of the time. Emission of the particle is always followed by a 411.7 keV gamma-ray.

In a later study (in London, England in 1963), Ansell *et al.* demonstrated improvement in 23 of 30 patients who had been injected with 185 to 370 MBq (5 to 10 mCi) ^{198}Au [33]. The patients were evaluated 12 months after injection, and improvement was loosely defined as an increase in joint movement or a reduction in pain or swelling. Similar results were reported by Topp *et al.* (in Toronto, Canada in 1970) [3] with 12 of 18 patients showing complete disappearance of effusion (*i.e.*, joint swelling due to an increased synovial fluid volume) at the end of one year and also by Virkkunen *et al.* [34] with 67 of 85 patients improving.

Although these and other studies [32, 33, 3, 34, 35] indicated that radiation synovectomy with ^{198}Au showed promise in the management of rheumatoid arthritis, they also noted leakage of ^{198}Au from the joint varying from 0-60% of the injected activity. In a patient group that otherwise could be regarded as healthy, the resulting extraarticular irradiation was considered to be unacceptable, and methods were sought to reduce the leakage.

^{90}Y

Throughout the 1970s, ^{90}Y gradually replaced ^{198}Au as the radionuclide of choice in radiation synovectomy. It is a pure beta-emitter (maximum energy 2.3 MeV) with a 64 h half-life. Because ^{90}Y does not emit a coincident gamma-ray, it generally was held to be safer for the patient. In addition, the greater penetration of its beta particles was believed to increase the likelihood of removing the entire volume of rheumatoid synovium [36, 37]. And the injected ^{90}Y radiocolloids (prepared as citrates, hyroxides, silicates, and resins) were found to be somewhat less likely to leak from treated joints [8].

Oka and Hypen (in Finland in 1974) [38] reported 60% improvement in 48 knees at one year after injection with 220 MBq (6 mCi) ^{90}Y resin colloid. Improvement again was loosely defined as an increase in joint movement or a reduction in pain or effusion.

A larger study, by Menkes *et al.* [39], included 1240 patients treated in a variety of synovial joints. They demonstrated a result similar to that of Oka and Hypen, with 50 to 60% of their patients showing improvement. In addition, Menkes *et al.* reported observing the best results in the knee.

Leakage of radioactivity from the joint remained a problem however. Although the overall leakage rates had been reduced, radiation doses to the draining lymph

nodes still were estimated to be often in excess of 100 Gy [40]. It was presumed that this excessive leakage was due primarily to the escape of very small particles, or "fines," from the treated joint [28].

^{32}P

^{32}P chromic phosphate in colloidal suspension also has been used in clinical trials. It, too, is a pure beta emitter (maximum energy 1.71 MeV) but has a much longer half-life of 14.3 d. Such a long half-life would seem to preclude the use of ^{32}P in radiation synovectomy, since it would appear to provide ample opportunity for injected radioactivity to leak from the joint before decay. In practice however research has indicated that the colloid tends to remain in the joint and is preferentially absorbed by the synovial lining cells. Because of the longer half-life, the amount of injected activity also is reduced, generally down to 37 to 110 MBq (1 to 6 mCi) ^{32}P.

In a study of 112 knees of patients at varying stages of rheumatoid arthritis, Onetti *et al.* [41] reported a good result in 73% of their patients treated at the early stages and in 31% of those treated at the advanced stages. Biopsies collected from 8 patients revealed decreases in the number of lining cells and lymphocytes in the synovium after treatment.

^{165}Dy

Finally, use of ^{165}Dy currently is in clinical trials under the direction of Sledge at Brigham and Women's Hospital (Boston, MA). ^{165}Dy has a 2.3 h half-life and decays by beta-particle emission (maximum energy 1.3 MeV) with a coincident 95 keV gamma-ray emitted in 3.6% of the decays.

In a study of 138 knees evaluated at 12 months after injection of 11 GBq (300 mCi) ^{165}Dy, Sledge *et al.* reported a good result in 63% of the patients, a fair result in 24%, and a poor result in 13% [7]. Patients with a good result were reported to have complete, or almost complete, relief of pain in the treated joints; little or no effusion; and an improved or maintained range of motion. Patients with a fair result were reported to have partial relief of pain; a diminished, or small, effusion; and to have maintained their pretreatment range of motion. Patients with a poor result were reported to have derived no benefit from the treatment, as evidenced by continued pain, effusion, and a limited range of motion. A second injection was given to the 13% of the patients who did not demonstrate improvement after the first injection. Of those who returned for follow-up, 54% demonstrated improvement after the second injection [27].

The radiopharmaceutical used in clinical trials by Sledge *et al.* is ^{165}Dy ferric hydroxide macroaggregate. The ^{165}Dy is produced at the MIT Nuclear Reactor Laboratory (Cambridge, MA) by thermal neutron activation of natural dysprosium ni-

trate dissolved in 3% nitric acid. The irradiations are performed with a thermal neutron flux of $\approx 8\times10^{12}$ n/cm^2-s and require 6 h to complete. Roughly 37,000 MBq (1000 mCi) ^{165}Dy is produced. The radionuclide then is mixed with 1 mg ferrous sulfate in 0.5 ml 0.1 N hydrochloric acid. One ml 0.2 N sodium hydroxide is added to precipitate the ^{165}Dy ferric hydroxide macroaggregate which is washed twice with polyvinylpyrrolidone to remove any small particles, or fines. The average size of the resulting particles is 3 to 10 μm [42].

In combination with the short half-life, the fairly large ^{165}Dy ferric hydroxide macroaggregate resulted in a significantly reduced radiation hazard for the injected patients [8]. By scanning for the 95 keV gamma-ray, Sledge *et al.* demonstrated that the mean uptake of radioactivity in the liver was less than 1% of the injected dose. The resulting absorbed dose to the liver was estimated to be 3.2 cGy [43]; similar studies conducted using ^{198}Au or ^{90}Y colloids typically have reported liver doses of 5.4 to 40 cGy [44]. Uptake of radioactivity in the inguinal lymph nodes also was evaluated by Sledge *et al.* They estimated that leakage of ^{165}Dy ferric hydroxide macroaggregate from injected joints results in an absorbed dose to the lymph nodes of roughly 17 cGy [43]. As a comparison, lymph node doses due to the leakage of ^{198}Au or ^{90}Y colloids typically are estimated to be between 270 and 6300 cGy [45].

2.4.2 Beta-particle dosimetry in radiation synovectomy

Empirical dosimetry

Previous attempts to evaluate beta-particle dosimetry in radiation synovectomy are limited, both in number and completeness. Most often, the approach has been empirical. In numerous clinical trials conducted over the past 40 years, several patients have been injected with a given dose of one particular radionuclide. Then at regular time intervals after injection, follow-up reports on reductions in pain and swelling or increases in joint movement are evaluated to determine whether or not the selected radionuclide and the amount of injected activity were appropriate.

Definite data on the absorbed dose required for successful treatment have not been established [8]. Difficult to determine, the absorbed dose depends not only on the radionuclide (its half-life and the energy spectrum of the emitted particles) and the amount of injected radioactivity, but also on the spatial and temporal distribution of the radionuclide in the joint. The distribution of activity varies from patient to patient and from joint to joint, however, as does the volume of tissue irradiated which is influenced by the thickness of pannus and the way the synovium is thrown into folds [1]. It is because of these difficulties that previous approaches to the dosimetry in radiation synovectomy typically have been empirical.

Analytical dosimetry

Nonetheless, analytical calculations of synovial dose have been reported [9, 3, 46]. As described in Chapter 1, analytical approaches to beta dosimetry often involve the use of tabulated values of beta-dose point kernels [47, 48]. The beta dose point kernels have been developed to represent the distribution of absorbed dose in tissue as a function of distance from a point-isotropic beta-emitting or monoenergetic electron source. By suitable spatial integration of the kernels, absorbed dose distributions can be calculated for a variety of source-to-target configurations [47, 48]. Tables published by Cross *et al.* [47] or Berger [48] provide beta dose point kernels for a number of electron sources in several media, and these data have been used extensively in beta dosimetry.

The most detailed of the analytical calculations of beta dosimetry in radiation synovectomy, by Husak *et al.*, applied the beta dose point kernel method to determine the dependence of absorbed dose in tissue on distance (up to 0.6 mm) from thin plane sources of ^{198}Au and ^{90}Y [9]. The point kernel method, however, is based on a model which neglects the production and transport of secondary electrons and the fluctuation of energy loss with distance [14, 15].

Prestwich *et al.* have reported Monte Carlo calculations of beta dose point kernels that do include the transport of secondary electrons and the effects of energy fluctuations [14]. Their approach shows a dose distribution for ^{90}Y in water that is 7% lower at the origin than predicted by the above methods and significantly higher at distances greater than 5 mm from the source. While these results have shown improved agreement with experiment, a systematic error in the energy-loss straggling algorithm has been revealed [15].

More important than this inaccuracy is the fact that the point kernel method is applicable only to homogeneous media, *i.e.*, homogeneous with respect to both elemental composition and density. For beta-particle dosimetry in heterogeneous media (*e.g.*, synovial joints), other approaches must be used, especially if doses to other, "non-target," tissues are of interest. In radiation synovectomy, absorbed doses to bone and articular cartilage are particularly of interest.

Other approaches

Other methods for evaluating beta dose distributions in radiation synovectomy are available. These include direct measurements in humans, which often can be difficult to obtain (see Chapter 5), and extrapolation from measured data in animals, phantoms, and cadavers. Other mathematical methods, *e.g.*, the Monte Carlo method, also can be used. The approach taken in this thesis was to evaluate beta-particle dosimetry in radiation synovectomy 3 different ways.

In Chapter 4, Monte Carlo estimates of beta-particle dosimetry in radiation syn-

ovectomy are presented. And in Chapter 5, experiments aimed at measuring absorbed dose distributions in joint phantoms and the knees of fresh, human cadavers are described.

2.4.3 What thickness of synovium should be removed?

An unanswered question in radiation synovectomy is what thickness of synovium should be removed in order to arrest progression of rheumatoid arthritis and provide patients with symptomatic relief of the disease. For the most part, current treatments using low-energy beta-emitters or surgery can be described as attempting to remove the entire synovial membrane. Existing data suggest however, that removal of only the surface layer of lining cells may be sufficient (see Chapter 6). Because it is the lining cells which are responsible for secreting high concentrations of proinflammatory cytokines thought to play a central role in progressive bone and articular cartilage degradation, it is hypothesized that removing the lining cells alone would eliminate the source of the cytokines, slow the progressive destruction of bone and cartilage, and thereby provide patients with symptomatic relief of rheumatoid arthritis for 2 to 5 years. In Chapter 6, the rationale for a series of experiments aimed at testing this hypothesis *in vitro* and *in vivo* is presented.

The proposed approach is to selectively irradiate and kill either the lining cells alone or the entire synovium using the $^{10}B(n,\alpha)$ nuclear reaction. This reaction has been chosen specifically because the range of the high-LET particles emitted is very short, on the order of 10 μm. As a consequence, the resulting radiation damage is very cell-specific, restricted only to boronated cells and their nearest neighbors. While these experiments have not been attempted in this thesis, preliminary studies of ^{10}B uptake in excised samples of live, human rheumatoid synovium were completed and are described in Chapter 7.

2.5 Conclusion

Rheumatoid arthritis is a progressive, autoimmune disease characterized by recurrent swollen, inflamed, and painful joints [23]. While the precise cause of rheumatoid arthritis remains uncertain, it is known to begin as a persistent inflammation of the synovium. If left untreated, the inflammation eventually leads to deformation, disability, and complete loss of joint structure and function.

Traditional treatments for rheumatoid arthritis generally are aimed at relieving the inflammation, both to slow progression of the disease and to provide patients with relief of pain, swelling, and stiffness [21]. Most patients respond to the conventional forms of treatment. For those who prove unresponsive, however, alternatives are needed. Radiation synovectomy has been developed as a quick, effective, low-cost

means of treating these patients. The procedure consists of the injection of a short-lived, low-energy beta-emitting radionuclide into the affected joint where it makes direct contact with the rheumatoid synovium. Provided the amount of radioactivity injected is sufficient to deliver a therapeutic radiation dose to the tissue, it will be killed. At the same time, one wants to ensure that other, healthy, joint components located nearby (*e.g.*, bone and articular cartilage) are not subjected to an unacceptable radiation hazard. It is for these, and other, reasons that the dosimetry in radiation synovectomy is of interest.

In Chapter 4, theoretical estimates of the dosimetry obtained using Monte Carlo radiation transport simulation in a mathematical model of the synovial joint are presented. And in Chapter 5, these Monte Carlo estimates are compared with experimental data measured in joint phantoms and the knees of cadavers using radiachromic film dosimeters and reactor-produced radionuclides. Before the dosimetry in radiation synovectomy is addressed, however, the thesis continues with a discussion of the approach used to generate the theoretical estimates, namely, the Monte Carlo simulation of electron transport in absorbing media.

Chapter 3

EGS4 Monte Carlo Transport of Electrons

3.1 Introduction

In this chapter, the EGS4 Monte Carlo transport of electrons is described. EGS4 is the Monte Carlo computer code used in this thesis to evaluate beta dose distributions in a mathematical model of the treated joint. A complete description of the code's approach to electron transport simulation is presented. Particular emphasis is given to the code's approach to low-energy electron transport simulation (kinetic energy below 2 MeV) since it is the dosimetry of low-energy beta-emitting radionuclides that is of interest in radiation synovectomy (see Section 2.4.1).

The chapter begins with general discussions of the Monte Carlo method itself and the mathematical tool used in all Monte Carlo calculations to solve a wide variety of problems, namely the sampling of random variables. Then the condensed history method of electron transport is reviewed. Condensed history transport has been developed to avoid direct simulation of the exceedingly large number of interactions that electrons undergo while slowing down in an absorbing medium. To reduce the number of computations required, the *cumulative* effects that multiple interactions have on electrons are simulated instead. The approaches used in EGS4 to estimate the cumulative effects that multiple scattering and continuous energy loss have on transported electrons are described. Finally, the chapter concludes with discussions of the code's approaches to the production of secondary particles, the handling of boundaries, and the scoring of deposited energy.

3.2 Monte Carlo method

The Monte Carlo method is a powerful and versatile tool useful for solving problems that are difficult or impossible to adequately solve using other mathematical techniques [49, 50, 51]. While the method now is used in a wide variety of applications, it originally was developed to solve neutron and photon radiation transport problems, and it is fair to say that it is in the field of radiation transport simulation that the method has made it greatest impact [51]. For the purposes of presenting an introduction to the method, the approach taken here thus is to restrict treatment of the method to its application in radiation transport simulation.

The basic form of the Monte Carlo method is as follows: using a computer, one conducts a radiation transport "experiment" by simulating the actual physical processes that govern the real particle's behavior [51]. The approach is to create a series of *life histories* of the source particles by using random sampling techniques to sample the probability laws that describe the real particle's behavior. Step by step, each particle is tracked through the simulation geometry until it can no longer contribute useful information to the problem at hand. Then, tracking of the current particle is terminated, and a "new" particle is generated from within the radiation source.

For example, suppose it is of interest to predict the probability that a photon emitted from a given radiation source region is absorbed in a particular target volume. In this instance, the principal aim of following the life histories is to count, or score, the number of photons that terminate in the specified volume. Then after all the photons have been processed, the score is divided by the total number of source particles initiated, yielding an estimate of the probability in question based on the average behavior of the transported photons. These two concepts are key features of the method: (1) determining each transported photon's contribution to the score, and (2) analyzing the accumulated data to obtain a description of the average particle behavior in the system of interest.

Since the Monte Carlo method is based on statistical concepts, the answers it provides are not unique. Rather, they are statistical in nature and subject to the laws of chance. This aspect of Monte Carlo is a drawback, but not a fatal one since one can determine how precise the answer is, and obtain more precise answers, if desired, by conducting more experiments. The degree of precision is inversely proportional to the square of the total number of experiments, or life histories.

3.2.1 Sampling random variables

As described above, the life history of a particle is constructed from a knowledge of its path through the system of interest. The particle originates from some point within the source with a known direction and energy. Then it has a free flight until

it collides with an atom of the absorbing medium. The collision could result in the absorption of the particle and the immediate termination of its history. Or it could result in a scattering interaction, in which case transport of the particle continues with a new direction and a change of energy. The change of direction and energy is a statistical process, *i.e.*, there is not a unique direction and energy that results after scattering. Rather, there is a distribution of probable outcomes for each of these two variables. To choose an outcome during simulation, the Monte Carlo method relies on the *sampling* of known *probability density functions* that describe the likelihood of occurrence of each of the possible outcomes.

The sampling of a probability density function can be described as picking a sequence of values (*i.e.*, "random variables") which, when taken together, obey the given function. As is shown below, the problem of sampling at random from an arbitrary probability density function can be conveniently reduced to the problem of choosing numbers at random from the rectangular distribution, *i.e.*, numbers which are uniformly distributed on the interval (0,1). Numbers chosen from the rectangular distribution are called random numbers ξ. Two procedures for using random numbers to sample random variables is described next.

Probability density functions

Consider an arbitrary probability density function $f(x)$ defined such that the probability that x takes a value between x_1 and x_2 is given by:

$$P\{x_1 < x < x_2\} = \int_{x_1}^{x_2} f(x)\mathrm{d}x. \tag{3.1}$$

As shown in Figure 3-1, it is assumed that x may take any value between the limits a and b, either of which may be minus or plus infinity, respectively. Corresponding to $f(x)$, there is a *cumulative probability distribution* $F(x)$ defined by:

$$F(x) \equiv \int_a^x f(x')\mathrm{d}x'. \tag{3.2}$$

The probability that the randomly selected value of x is less than x_1, $P\{x < x_1\}$, is thus given by $F(x_1)$. The function $F(x)$ can be said to be monotonically increasing with x if $f(x)$ is a properly normalized probability density function between a and b, with $F(a) = 0$ and $F(b) = 1$.

Sampling methods

Direct sampling method. A number of computer algorithms are available for generating a large number of random numbers ξ uniformly distributed between 0 and

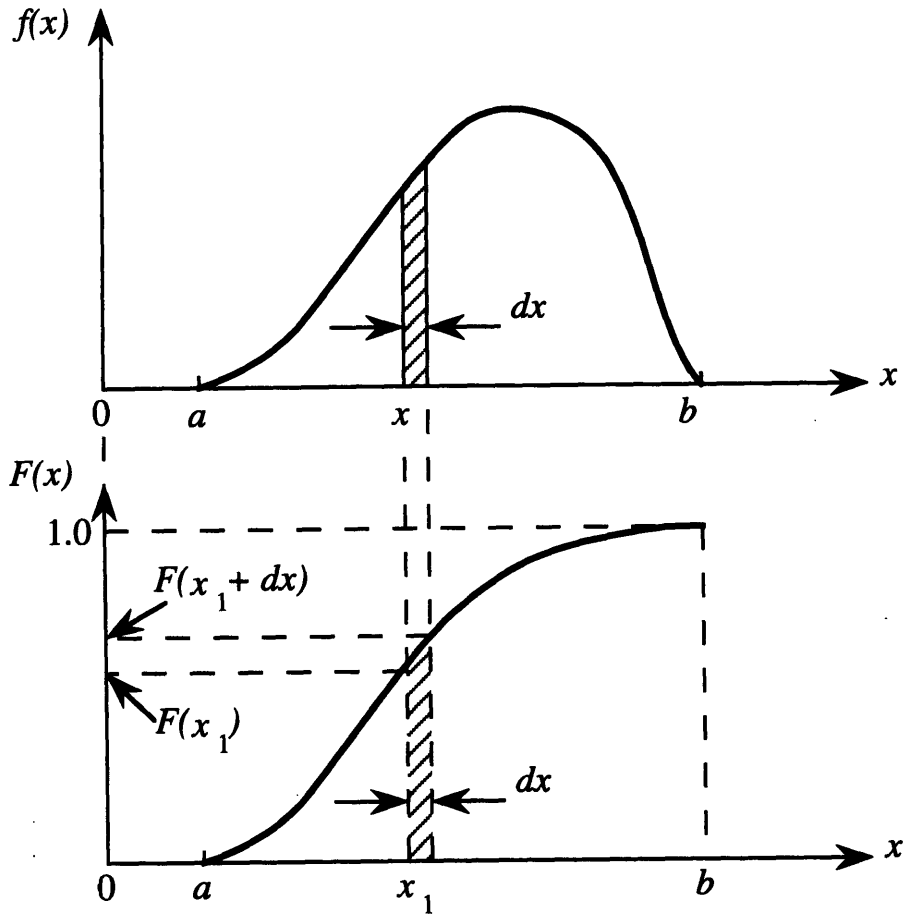

Figure 3-1: Graph of a probability density function, above, and its corresponding cumulative density function, below.

1 [52, 53, 50]. The procedure to use these random numbers ξ to directly sample random values of the variable x then is accomplished by the following algorithm:

1. select a random number ξ between 0 and 1
2. set $F(x) = \xi$, and calculate $x = F^{-1}(\xi)$.

As an example, consider a photon moving away from a given interaction point in a certain direction through a medium of constant interaction properties (*i.e.*, constant μ) [50]. The physical law governing the distance to the next interaction is the exponential probability law. That is, the probability that no interaction occurs for a photon travelling a distance x is $e^{-\mu x}$, where μ is the total linear attenuation coefficient, and $\mu e^{-\mu x} dx$ is the probability that an interaction occurs in the distance x to $x + dx$. The cumulative probability distribution is:

$$F(x) = \int_0^x \mu e^{-\mu x'} dx' = 1 - e^{-\mu x}. \tag{3.3}$$

A random sample x_i is obtained by generating a random number ξ_i, $(0 < \xi_i < 1)$, and solving the equation $\xi_i = 1 - e^{-\mu x_i}$ for x_i:

$$x_i = -\frac{\ln(1 - \xi_i)}{\mu}. \tag{3.4}$$

Rejection sampling technique. The direct method presents difficulties if the probability density function $f(x)$ cannot be integrated to obtain $F(x)$ or if $F^{-1}(\xi)$ is difficult to obtain analytically. Alternate sampling methods then are needed. One widely-used alternate method is the rejection sampling technique.

Consider two probability density functions $f(x)$ and $g(x)$, where $f(x)$ is assumed to be difficult to work with and $g(x)$ is assumed to be similar but simpler, as shown in Figure 3-2. The latter function is taken to have an easily obtainable cumulative distribution function $G(x)$, which can be inverted to yield $G^{-1}(\xi)$. Note that:

$$F(x) = \int_a^x h(x')g(x')dx', \tag{3.5}$$

where the ratio $h(x)$ is defined by:

$$h(x) \equiv \frac{f(x)}{g(x)}. \tag{3.6}$$

Now, if $g(x)$ represents a close approximation to $f(x)$, $h(x)$ remains close to unity. Regardless, it can be required that $g(x)$ be chosen so that $h(x)$ does not exceed some maximum bounding value h_{max} in the interval a to b.

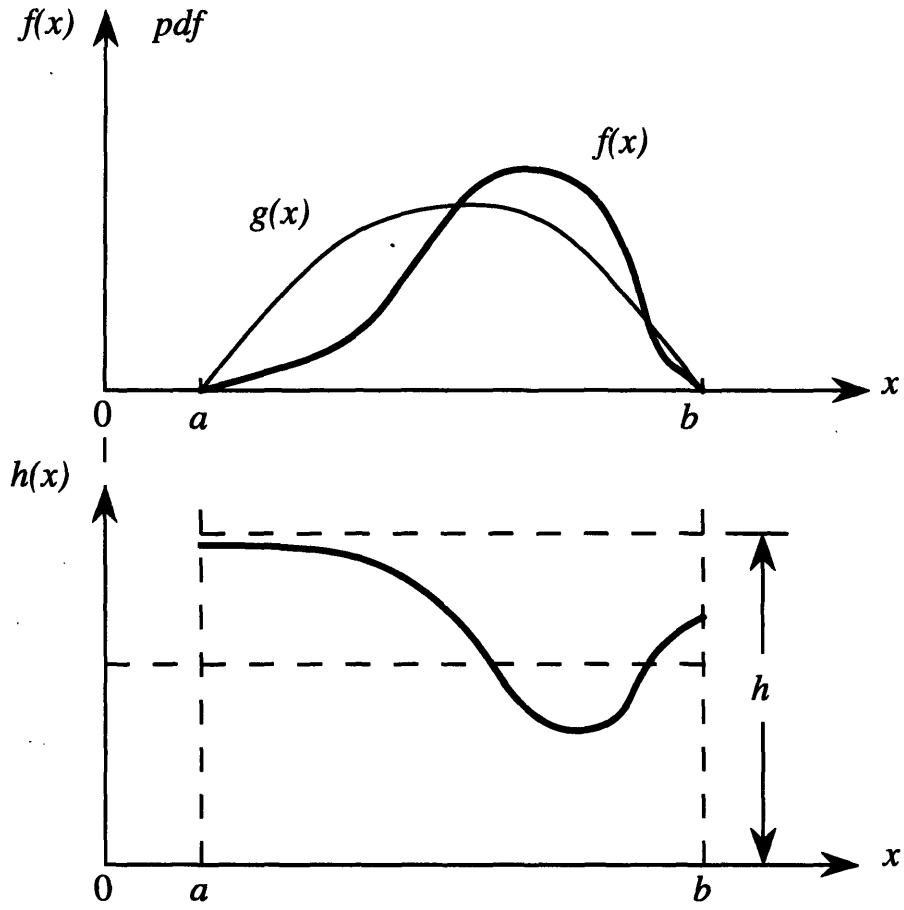

Figure 3-2: Graphs of a difficult probability density function $f(x)$ and an easier probability density function $g(x)$ which approximates $f(x)$. The ratio $h(x) = g(x)/f(x)$ is plotted in the lower figure. Here h_{max} is any finite upper bound for $h(x)$.

The rejection technique then proceeds as follows:

1. select a random number ξ_i between 0 and 1
2. calculate a tentative value of x from $x_i = G^{-1}(\xi_i)$
3. select another random number ξ_{i+1} between 0 and 1
4. if $\xi_{i+1} > h(x_i)/h_{max}$, then *reject* the value of x_i and return to step 1, else *accept* x_i.

It is through the use of these and other sampling methods that Monte Carlo can be used to deduce the average behavior of all the particles in a particular system by sampling at random the behavior of some.

3.3 EGS4 code

Developed in 1978 at the Stanford Linear Accelerator Center (Stanford, CA), EGS4 (Electron-Gamma Shower, Version 4) is one of a few widely-used Monte Carlo codes capable of simulating electron and photon transport through materials [54]. It originally was written to study high-energy electromagnetic cascade showers, such as those generated at accelerator facilities, but in recent years has undergone a number of revisions to extend its useful range to include lower energies[54].

Other Monte Carlo electron transport codes also are available in the public domain. These include the ETRAN (Electron TRANsport) [55] and ITS (Integrated Tiger Series) codes [56]. Important differences between EGS4 and these two codes include their approaches to the simulation of multiple scattering (see Section 3.4.3), the creation of secondary particles (see Section 3.5), and the handling of boundaries (see Section 3.6) [57]. For example, the ETRAN and ITS codes use the Goudsmit-Saunderson theory of multiple scattering [58] in their approaches to electron transport simulation, whereas the multiple scattering theory of Moliére [59, 60] is used in EGS4. The Moliére theory has been derived using a small angle approximation (see Section 3.4.3); the Goudsmit-Saunderson theory has not. While it is generally held that, as a consequence, the Goudsmit-Saunderson theory is more accurate, Bethe has shown that with some modification of the Moliére formalism, results of the two theories are nearly equivalent [61].

Compared to the other codes, EGS4 has the advantage of having a high degree of flexibility in its operation. To run the code, users must write their own coding of the simulation geometry and algorithms responsible for scoring any quantities of interest, *e.g.*, the number of photons which terminate in a particular target volume. The EGS4 code package itself is equipped to simulate only the physics of electron and

photon transport through materials, *i.e.*, it does not set up the simulation geometry or tabulate a standard collection of output. As a consequence, the code can be customized for use in a wide variety of applications. The **ETRAN** code, on the other hand, while easier to use, has been described as being virtually impossible to adapt [57].

Installed and operational in the Whitaker College Biomedical Imaging and Computation Laboratory at MIT (Cambridge, MA), **EGS4** is the code used here to complete Monte Carlo simulations of radiation transport in a mathematical model of the rheumatoid joint (see Chapter 4). Beta-particles (electrons) "emitted" from within the model's radiation source region were transported through the model by the code, and deposited energy was scored. In the remainder of this chapter, the code's approach to electron transport simulation is presented.

3.4 Condensed History Electron Transport

In Monte Carlo radiation transport simulation, particle tracks are generated by simulating the random nature of individual particle interactions with the medium. To carry out the simulation, all one needs are complete mathematical descriptions of the probability relationships which govern: the distance from one interaction point to the next; the choice of an interaction type at each interaction point; if the interaction is of a scattering type, the choice of a new energy and a new direction; and the possible production of additional particles. With this information, the entire life history of a particles, from the time it leaves its source to the time it is absorbed or passes out of the system, can be simulated directly. And in the Monte Carlo simulation of neutron and photon transport, where the total number of interactions each particle experiences is relatively small, this is an accurate description of what occurs. For example, not more than 30 Compton scatterings are likely to occur in the reduction of a photon's energy from 5 MeV to 50 keV [50].

In the case of electron transport, the situation is more complicated. Since electrons can suffer thousands of collisions and lose only a fraction of their incident energy, direct simulation of every interaction event would be extremely time-consuming. When electrons are scattered through gold, for instance, a typical electron can be expected to experience more than 100,000 collisions in slowing down from 50 to 20 keV [62]! For this reason, direct simulation of every interaction is not considered a viable method in the majority of electron transport problems. The *condensed history method* was developed as an alternative.

Described by Berger in his classic review of Monte Carlo charged particle transport [62], the approach is to simulate the cumulative effects that multiple interactions have on a transported electron's energy, location, and direction. The electron's walk is idealized as a zig-zag path, consisting of free flights interrupted by sudden collisions

in which its energy and direction are changed. Since each free flight, or step, in a condensed history random walk can represent hundreds of individual interactions, the method is hundreds of times faster than direct simulation. Energy and direction probability density functions for multiscattered electrons are used to determine the electron's state at the end of each step.

According to Berger the condensed history method can be classified in two procedures:

Class I. The simpler of the two, it relies entirely on the grouping of all interactions.

Class II. In a more realistic approach, this procedure relies only on the grouping of *minor* interactions, *i.e.*, those in which energy losses or deflections are small. Occasional *major* events, or 'catastrophic' collisions, in which energy losses or deflections are very large, are treated separately by conventional random sampling according to the single-scattering cross sections. EGS4 uses the Class II approach in an electron transport logic which is summarized in Section 3.4.2.

3.4.1 Transport step sizes

Transport step size can be defined as the distance travelled, or energy lost, between two points of *catastrophic* interaction (see below). In a condensed history random walk, transport step sizes are chosen according to conflicting requirements. On one hand, the steps should be *long* enough so that: (1) the number of collisions per step is sufficiently large to justify the use of probability density functions for multiscattered electrons (see Section 3.4.3) and (2) the number of steps per electron is sufficiently small that a large number of walks can be simulated in a reasonable period of time. On the other hand, the steps should be *short* enough so that: (1) for the most part, the electron transport takes place as if in an infinite medium and (2) the average energy loss and angular deflection per step are kept small. When these last two conditions are not satisfied, the assumptions used to derive energy and direction probability density functions for multiscattered electrons become invalid.

In EGS4, the process of transport step size selection begins with the electron's total (angle integrated) cross section σ_t which is dependent on both the electron's kinetic energy and the medium in which it is travelling. The cross section σ_t represents the sum of the individual contributions due to elastic Coulomb scattering off the nucleus, inelastic scattering off atomic electrons, and bremsstrahlung production. Threshold energies are used to distinguish major, or catastrophic, interactions from those which are to be grouped together as minor interactions and treated as part of a continuous energy loss process. The approach is to divide the electron's history into a series of sections, or steps, within which no catastrophic collisions occur and in which continuous slowing down (see Section 3.4.4) is assumed. Each step is terminated by a catastrophic interaction.

The threshold energies used in EGS4 are given by the variables AE, for electrons, and AP, for photons. An interaction, for instance, which produces a knock-on electron having a total energy greater than or equal to AE is considered to be a *major* event and is directly included in the simulation. Interactions resulting in a transfer of energy below the threshold, on the other hand, are considered to be minor and grouped together as part of the 'continuous' process. Minor interactions primarily include weak interactions with atomic electrons (excitations and ionizations), multiple Coulomb scattering off nuclei, and the production of *soft* bremsstrahlung, *i.e.*, bremsstrahlung photons with energy less than AP.

The above considerations complicate electron transport in several ways. The introduction of continuous energy loss, for instance, causes the simulated electron's total cross section σ_t to vary along its path, as it loses energy. In addition, the path of the simulated electron undergoing continuous energy loss between points of catastrophic interaction is assumed to remain straight, whereas it is not straight in reality.

To account for a change in cross section along the electron's path, the following *trick* is used in EGS4. An additional, fictitious interaction is introduced which results in straight-ahead scattering, *i.e.*, no interaction at all. It is assumed that the magnitude of the cross section for this fictitious interaction σ_{fict} is such that the total cross section $\sigma_{t,real}$ remains constant along the path, that is:

$$\sigma_{t,real}(x_0) = \sigma_{t,real}(x) + \sigma_{fict}(x) = \sigma_{t,fict}(x), \tag{3.7}$$

where x_0 and x are the electron's initial and final positions, respectively.

The transport step size, *i.e.*, the distance to the next catastrophic interaction, is then selected by sampling an equation similar to Eqn. 3.4, where μ, the photon attenuation coefficient, has been replaced by $1/\lambda_{fict}$, where λ_{fict} is the electron's fictitious mean free path, given by the relation:

$$\lambda_{fict} = \frac{M}{N_A \rho \sigma_{t,fict}}, \tag{3.8}$$

where M is the molecular weight of the medium, ρ is its density, N_A is Avogadro's number, and $\sigma_{t,fict}$ is the electron's total, fictitious cross section.

After the electron is transported to the point of interaction, a random number is generated and compared to the ratio $\sigma_{t,real}(x)/\sigma_{t,real}(x_0)$. If the random number is larger than the ratio, then the interaction is considered to be fictitious, and transport continues from that point without interaction. Otherwise, the interaction is considered to be real and handled as described later.

This trick can be shown to work correctly as long as the total cross section decreases with decreasing energy. For very low values of AE however, *e.g.*, AE < 580 keV

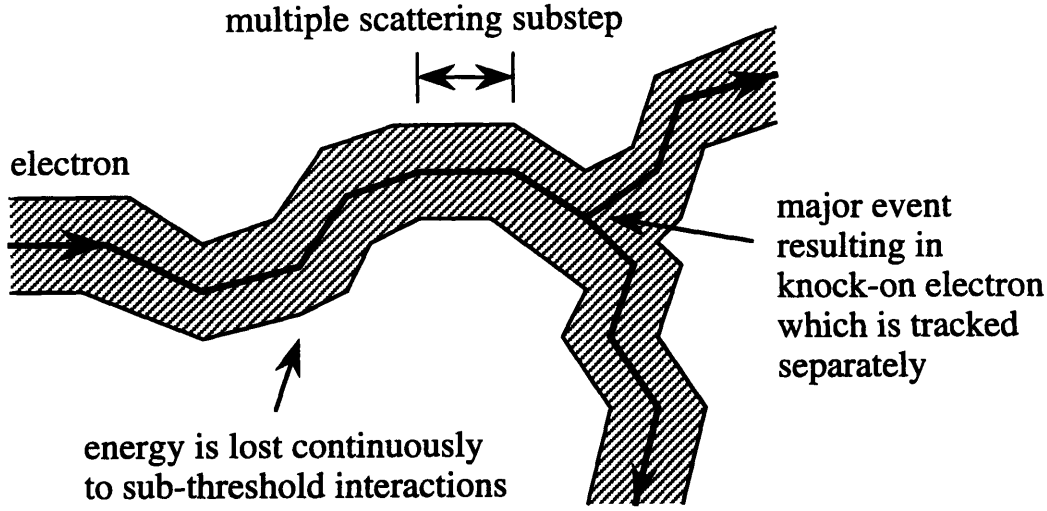

Figure 3-3: Typical electron track as simulated by EGS4. The electron's path is broken into a number of small multiple scattering substeps. Along each substep, the electron is assumed to travel in a straight line. At each substep's end, changes in the electron's energy and direction due to sub-threshold interactions are determined using probability density functions for multiscattered electrons. When a point of catastrophic interaction is reached, it is treated separately by conventional random sampling according to the single-scattering cross sections.

total energy (70 keV kinetic energy) in low-Z materials, this is not the case. As a consequence, a systematic error is introduced in low-energy, low-Z problems because the number of catastrophic interactions is underestimated [63]. The effect is usually small however, leading to, at most, a 4% error in an electron's total energy loss for a typical worst case situation [63].

To account for the fact that the simulated electron's straight-line path between catastrophic interactions does not reflect that of reality, multiple scattering theory is used to divide the path from one interaction to the next into a number of *smaller* multiple scattering "substeps," as shown in Figure 3-3. Along each substep, the electron is *assumed* to travel in a straight line. At each substep's end, change in the electron's direction due to sub-threshold interaction events is determined using the multiple scattering theory of Moliére [59, 60] (see Section 3.4.3); energy loss is determined using the continuous slowing down approximation (see Section 3.4.4).

3.4.2 Electron transport logic

Figure 3-4 is a schematic flow chart showing the essential features of the electron transport logic used in EGS4. To begin, imagine that an electron has been "emitted" at some point within the source region of a given radiation transport problem, and its initial parameters (*i.e.*, energy, position, direction, etc.) are available at the top of the EGS4 particle parameter stack. The electron transport routine ELECTR reads these parameters and uses them to determine whether or not the electron's total energy is large enough to authorize transport. If the electron's energy is greater than the user determined transport cutoff energy ECUT, then ELECTR initiates transport. On the other hand, if it is not, then the electron is immediately *discarded*, meaning that the EGS4 scoring routines are informed that the current particle is being removed from the transport stack (see Section 3.6), and another electron is "generated" for simulation.

Assuming that the original electron's energy is large enough to initiate transport, ELECTR determines: (1) the distance to the next point of major, or catastrophic, interaction as described in Section 3.4.1, (2) the maximum multiple scattering step size as described in Section 3.4.3, and (3) the straight-line distance in the current direction to the nearest boundary. The electron is then transported the shorter of the three distances. At the end of the step, the net angular deflection and energy loss resulting from subthreshold interaction events are sampled using the multiple scattering theory of Moliére (see Section 3.4.3) and calculated stopping power data (see Section 3.4.4), and the electron's direction and energy are adjusted accordingly. Lost energy is deposited in the current region. The term region is used to describe any of the various scoring volumes which define a simulation geometry.

If, as a result of this transport step, the electron has reached the nearest boundary, then it is handled as described in Section 3.6. On the other hand, if the electron has not reached a boundary, its energy (now reduced due to continuous energy loss occurring along the step) is tested once again by ELECTR to determine whether or not it has fallen below the cutoff. If the energy has fallen below the cutoff, the electron is discarded and its energy is deposited in the current region. If not, the simulation continues and ELECTR must determine whether or not a point of major interaction has been reached. If a point of major interaction has not been reached, then a new multiple scattering step is simulated. In most electron-transport simulations, this innermost loop undergoes the heaviest use since many multiple scattering steps often occur between points of catastrophic interaction. On the other hand, if a point of major interaction has been reached, then the type of interaction is chosen and the relevant physical processes are simulated. Parameters for secondary particles (*i.e.*, knock-on electrons or bremsstrahlung photons) which result are stored on the particle stack for subsequent transport simulation. Once transport of the primary particle is complete, transport of any secondaries is initiated, one particle at a time. A typical electron track as simulated by EGS4 is shown in Figure 3-3.

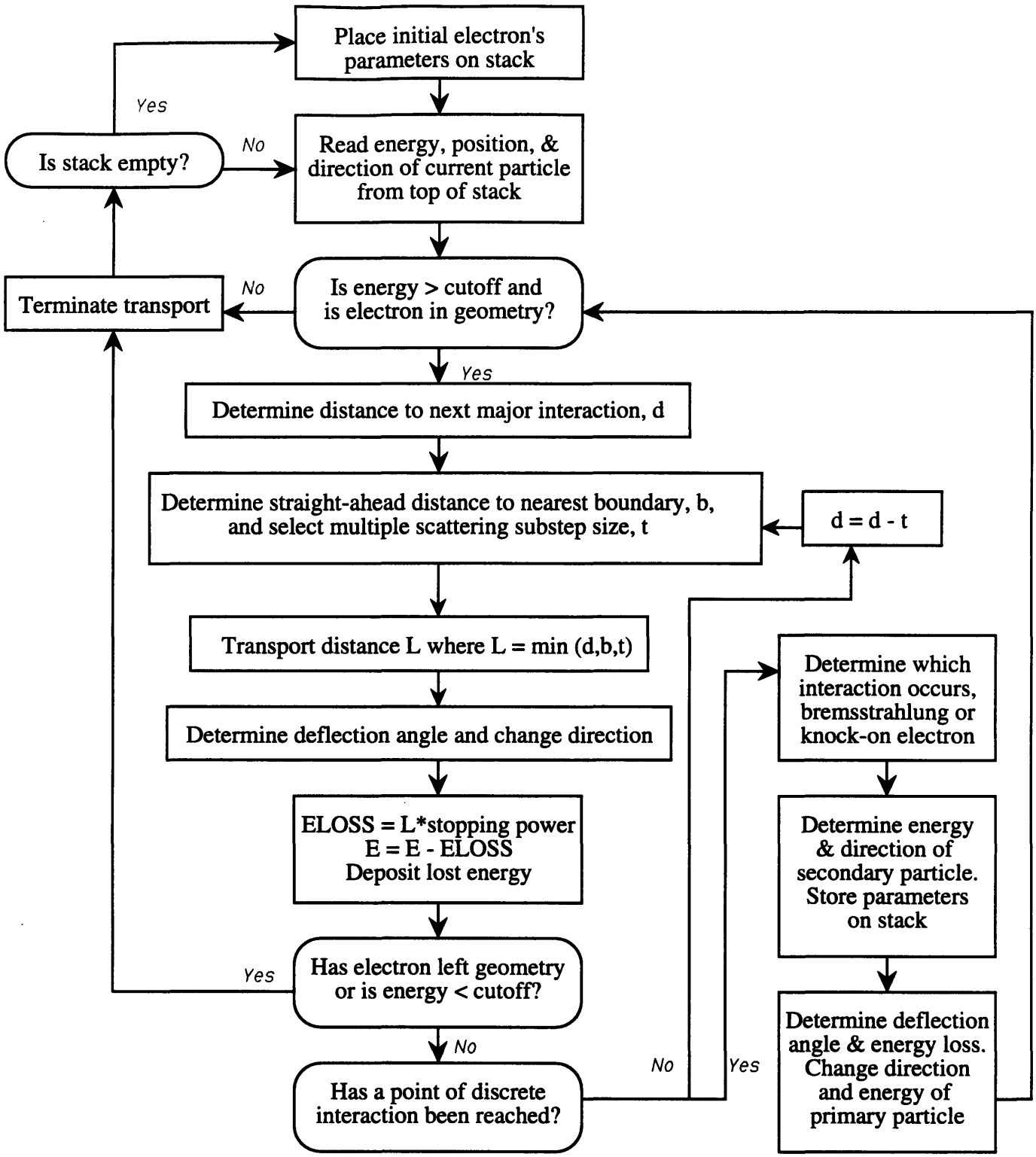

Figure 3-4: Flow chart describing the electron-transport logic used in EGS4.

3.4.3 Multiple scattering

In reality, a single multiple scattering substep is characterized by the length t of curved path an electron takes in moving from its starting point a to an end point b, as shown in Figure 3-5. Associated with the substep are the projected distance s of deflection in the original direction and the projected distance ρ of deflection in the lateral direction. In **EGS4** the lateral deflection occurring along the course of the substep is ignored, and the multiply-scattered electron is transported a distance s in the original direction only. At the end of the substep, the angular deflection θ from the original direction is sampled using the Moliére theory of multiple scattering [59, 60], and the electron's direction is adjusted accordingly. The scattering angle θ is dependent on the transport material, the length of curved path t, and the electron energy E.

It is important to note that, while ignoring the lateral deflection may introduce problems for electrons allowed by some codes to take large transport steps, in **EGS4** this problem is avoided by breaking the transport history into a number of small multiple scattering substeps and deflecting the electron at the end of each substep. As a result, lateral transport of the electron is effectively accomplished [54, 64]. Most electron transport codes incorporate this approach of using small step sizes to overcome the lack of direct lateral transport simulation [64].

The Moliére theory of multiple scattering can be described beginning with the following parameters:

$$\Omega_0 = b_c t/\beta^2, \tag{3.9}$$

$$\chi_c^2 = \chi_{cc}^2 t/E^2\beta^4, \tag{3.10}$$

where b_c and χ_{cc} are constants that depend only on the material in which the transport takes place, β is the ratio of the electron's speed to the speed of light, E is the electron's total energy, and t is the total curved pathlength of the electron substep. The parameter Ω_0 can be interpreted as the number of atoms that participate in the multiple scattering. Moliére considered his theory valid for $\Omega_0 > 20$ atomic interactions [59, 60].

The Moliére multiple scattering angle distribution is given by the following:

$$f(\theta)\theta \mathrm{d}\theta = f_r(\phi)\phi \mathrm{d}\phi, \tag{3.11}$$

where θ is the scattering angle and ϕ is the reduced angle. They are related by:

$$\phi = \theta/\chi_c B^{1/2}, \tag{3.12}$$

where $B - \ln B = b = \ln \Omega_0$. From this definition of B and b, one sees that there is a lower limit, $\Omega_0 = 2.718$ atomic interactions, below which Moliére's formalism breaks

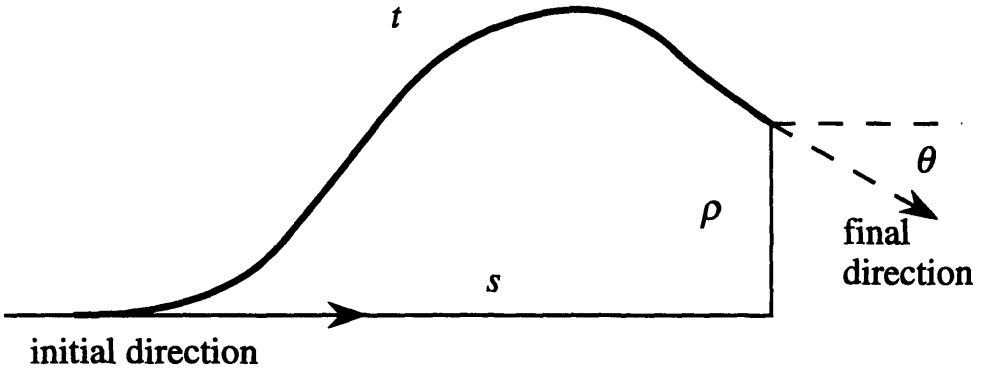

Figure 3-5: A single multiple scattering substep of a real electron. In EGS4 only the straight-ahead portion of the substep is simulated; the lateral deflection is ignored. It is important to note, however, that by breaking the transport history into small multiple scattering substeps and deflecting the electron at the end of each substep, lateral transport of the electron is effectively accomplished.

down mathematically. It is interesting to note that the theory often is used in EGS4 below this limit and still produces reliable answers [54, 64].

The angular distribution can be expanded in a power series in $1/B$:

$$f_r(\phi) = f^{(0)}(\phi) + \frac{f^{(1)}(\phi)}{B} + \frac{f^{(2)}(\phi)}{B^2} + ..., \tag{3.13}$$

where

$$f^{(0)}(\phi) = 2e^{-\phi^2} \tag{3.14}$$

and $f^{(1)}$ and $f^{(2)}$ are given by Bethe [61]. The expansion is strictly valid only for $B > 1$ ($\Omega_0 > 2.718$ atomic interactions). This restriction essentially imposes an absolute lower limit on the substep size. Using the criterion $\Omega_0 = 2.718$, one sees from Eqn. 3.9 that the minimum substep size is given by:

$$t_{min} = e\beta^2/b_c. \tag{3.15}$$

For water, t_{min} is approximately 4×10^{-4} cm over a wide range of energies. For other materials, the relative dependence is approximately governed by a $\rho/\beta^2 Z_{avg}$ factor, where ρ is the density and Z_{avg} is the average atomic number of the transport material. This is an exceedingly small distance for many practical purposes.

In EGS4, the default value for t_{min} is chosen using $\Omega_0 = 1$ atomic interaction, not 2.718 as assumed by Bethe. Below $\Omega = 2.718$ an extrapolation is performed to relate B and Ω since the theory is mathematically valid only above $\Omega = 2.718$. It is important to note that at these small substep sizes EGS4 *turns off* the simulation of multiple scattering, and elastic scattering of electrons off nuclei is ignored (see Section 3.4.5 for more on this problem).

An upper limit on the electron substep size has been derived by Bethe [61], who has shown that Moliére's theory (initially derived as a small angle theory) and the theory of Goudsmit and Saunderson [58] (which does not rely on a small angle approximation) are nearly equivalent as long as the following condition is satisfied:

$$\chi_c^2(t)B(t) \leq 1. \tag{3.16}$$

The quantity $\chi_c^2 B$ can be interpreted as the mean-square scattering angle. After some manipulation, the maximum substep size can be written as follows:

$$t_{max} = \frac{E^2\beta^4}{\chi_{cc}^2 \ln(b_c E^2\beta^2/\chi_{cc}^2)}. \tag{3.17}$$

The upper limit t_{max} varies in the same fashion as t_{min} for different materials, roughly by a relative $\rho/\beta^2 Z_{avg}$ factor.

The limitations of Moliére's theory, therefore, include the following:

1. It is a *multiple*-scattering theory and thus many atomic collisions are assumed to contribute to the electron's angular deflection. This assumption effectively places a lower limit on the substep size.

2. It is based on a small-angle approximation ($\sin\theta \approx \theta$) and thus angular deflections are assumed to be small. This approximation effectively places an upper limit on the substep size.

3. It has been derived only for infinite or semi-infinite homogeneous media. Electron transport in the vicinity of material interfaces must therefore be treated very carefully (see Section 3.6).

4. It is only an angular deflection theory. Continuous energy loss due to multiple scattering is not included.

The principal advantage of Moliére's theory is that the multiple scattering distribution is expressed as a function of the deflection angle. As a result, the distribution is easily sampled to select multiple scattering deflections for randomly sampled pathlengths.

3.4.4 Continuous energy loss

In **EGS4** energy loss due to multiple scattering is determined using the continuous slowing down approximation, *i.e.*, it is assumed to equal the distance traveled t times the stopping power S which expresses the mean energy lost by an electron per unit length in the transport material. In other words, the statistical fluctuations of energy losses in successive interactions are disregarded, and electrons are assumed to lose energy along their tracks in a deterministic, continuous manner, at a rate given by the stopping power. The losses are due primarily to weak interactions with atomic electrons and the production of soft bremsstrahlung, *i.e.*, bremsstrahlung photons with energy less than **AP**.

The stopping power S for continuous energy loss can be separated into two components:

$$S = -\frac{\mathrm{d}E}{\mathrm{d}x} = -\frac{\mathrm{d}E}{\mathrm{d}x}\Big|_{\textit{weak col}} - \frac{\mathrm{d}E}{\mathrm{d}x}\Big|_{\textit{soft brem}}, \tag{3.18}$$

where $\mathrm{d}E$ is the mean energy lost per unit length $\mathrm{d}x$.

Weak collisions. The weak collision component includes all energy losses associated with the excitation and ionization of atoms or molecules. It can be rewritten as

the product of the amount of energy transferred in a single collision T and the differential cross section for transferring that amount of energy to an atomic electron $\frac{d\Sigma}{dT}$, integrated over the range of energy transfers which result in sub-threshold secondary electrons, that is:

$$-\frac{dE}{dx}|_{weak\ col} = \int_0^{\mathbf{AE}} T\frac{d\Sigma}{dT}dT. \tag{3.19}$$

For energy transfers on the order of atomic excitation energies, integration of the expression is quite complicated. However when the energy transfer is large compared to the binding energy of the target electron, it is a good approximation to treat the collision as obeying the Møller cross section [65], which has been derived using the assumption that the target electron is free and initially at rest.

If T_{med} is defined as a value of T sufficiently above the atomic excitation level but still small compared to **AE**, then Eqn. 3.19 can be rewritten as:

$$-\frac{dE}{dx}|_{weak\ col} = \int_0^{T_{med}} T\frac{d\Sigma}{dT}dT + \int_{T_{med}}^{\mathbf{AE}} T\frac{d\Sigma_{Moller}}{dT}dT. \tag{3.20}$$

In the first interval, binding of the atomic electrons must be taken into account, and the Møller cross section cannot be used. Instead, the integral can be evaluated using the Bethe-Bloch theory of charged particle interactions [66, 67]. In the second interval, integration over the Møller cross section can be completed. When the two results are combined, the resulting expression for the weak collision component of the stopping power is as follows:

$$-\frac{dE}{dx}|_{weak\ col} = \frac{2\pi e^4}{mv^2}NZ\left[\ln(\frac{2(\tau+2)}{I/m}) + F(\tau,\Delta) - \delta\right], \tag{3.21}$$

where,

$$F(\tau,\Delta) = -1-\beta^2+\ln[(\tau-\Delta)\Delta] + \frac{\tau}{\tau-\Delta} + \frac{\Delta^2}{2\gamma^2} + \frac{2\tau+1}{\gamma^2}\ln\left[1-\frac{\Delta}{\tau}\right], \tag{3.22}$$

and where e is the charge of an electron, m is the mass of the transported electron and v is its velocity, N is the number of target atoms per cm^3, Z is the atomic number of the transport material, τ is kinetic energy of the transported electron in units of rest mass, I is the mean ionization potential, Δ is the maximum energy transfer, and δ is a correction factor to account for the density effect, *i.e.*, reduction of the mean energy loss caused by polarization of the medium. In the default version of **EGS4**, the Sternheimer [68, 69] treatment of the density effect is used, but this treatment can be overridden by interested users.

Soft bremsstrahlung. The soft bremsstrahlung component of the stopping power, *i.e.*, the second term on the right-hand side of Eqn. 3.18, takes into account energy losses due to the emission of bremsstrahlung photons with energy below the production threshold **AP**. It can be rewritten as the product of the bremsstrahlung photon energy k and the differential cross section for creating a photon of that energy $\frac{d\Sigma_{brem}}{dk}$, integrated over the range of energies resulting in the production of sub-threshold bremsstrahlung photons, that is:

$$-\frac{dE}{dx}|_{soft\ brem} = \int_0^{AP} k\frac{d\Sigma_{brem}}{dk}dk. \tag{3.23}$$

The bremsstrahlung cross section, differential in emitted photon energy, $\frac{d\Sigma_{brem}}{dk}$ is given in Section 3.5.1. Assumptions and approximations used to derive the cross section are described there.

It is worth noting that users have the *option* to modify the above calculation and normalize the bremsstrahlung cross sections used in the code so that the calculated soft bremsstrahlung stopping power data are identical to the radiative stopping power data for electrons given in *ICRU-37* [70, 71]. The stopping powers tabulated in *ICRU-37* generally are considered to be the most accurate radiative stopping power data available [72].

3.4.5 Subtep size restrictions

The procedure for sampling substep sizes is subject to several restrictions as described in Section 3.4. In particular, the Moliére theory of multiple scattering places a number of limitations on the size of each substep (see Section 3.4.3). These include the fact that its size must not exceed the maximum limit t_{max}, otherwise the small angle approximation used in the derivation of Moliére's theory becomes invalid [61]. Other restrictions independent of multiple scattering theory include the facts that the substep size must not exceed the range of the electron or the distance to the next catastrophic interaction or boundary.

Substep size restrictions have been incorporated in **EGS4** to account for these limitations. In particular, the subroutine **FIXTMX** has been introduced to limit the amount of energy an electron may lose along each step or substep to a fixed fraction, **ESTEPE**, of the electron's total energy. This technique is similar to the step size algorithms used in other electron transport codes, such as **ETRAN** [73]. One must ensure, however, that the physical quantity of interest is not significantly influenced by the choice of **ESTEPE**. To avoid this step size dependence, users are advised to continually decrease the size of **ESTEPE** until the quantity of interest is no longer significantly affected by the changes. In **EGS4** the total pathlength t per multiple scattering substep is deduced from the straight-line pathlength s using a multiple

scattering approximation to account for curvature in the path. As smaller and smaller substep sizes are used, the difference between t and s decreases and the accuracy of the procedure increases. In many cases, it is this change in t as a function of s which can lead to an **ESTEPE** dependence in calculated results [63].

Users also are cautioned against choosing too small a value for **ESTEPE**, otherwise multiple scattering may not be simulated. This *turning off* of multiple scattering can lead to remarkable artefacts in calculated results since the elastic scattering of electrons off nuclei is ignored. Users are therefore advised to monitor the number of times multiple scattering is not simulated. The **EGS4** variable **NOSCAT** has been included for this purpose. Each time multiple scattering is turned off, the variable is incremented by 1. It is worth noting that this turning off of multiple scattering typically is done *first* for the lowest energy electrons. As a result, the fraction of **NOSCAT** substeps can be relatively large (on the order of 1%) before the calculated results are affected [63].

3.5 Major Interactions

When a point of major, or catastrophic, interaction is reached, **EGS4** must choose which one of the competing processes is to occur. The probability that a given process occurs is proportional to its cross section. For instance, suppose that at a point of major interaction, there are j possible types of interaction numbered from 1 to n, such that the total interaction cross section σ_t is given by:

$$\sigma_t = \sum_{j=1}^{n} \sigma_j, \tag{3.24}$$

where σ_j is the cross section for the j^{th} type of interaction.

The number i of the chosen process can be said to be a random variable having the cumulative distribution function:

$$F(i) = \frac{1}{\sigma_t} \sum_{j=1}^{i} \sigma_j \tag{3.25}$$

The interaction number i is then determined by choosing a random number ξ, $(0 < \xi < 1)$, and finding the i which satisfies the relation:

$$F(i-1) < \xi < F(i). \tag{3.26}$$

3.5.1 Bremsstrahlung production

In EGS4 bremsstrahlung production refers to the creation of secondary photons with energy above the user-supplied threshold AP by electrons undergoing acceleration in the electric field of an atom. Two types of interaction are actually possible. The predominant mode of interaction is a two-body process in which the electron is accelerated in the electric field of a nucleus. The second interaction is a three-body process in which the electron is accelerated in the field of an atomic electron, setting three bodies in motion: the initial electron, a recoiling atomic electron, and the bremsstrahlung photon. In EGS4 the three-body process is not included directly in the simulation. Rather, it is included indirectly as a correction factor to the bremsstrahlung cross section for the two-body process.

The theory used in EGS4 for bremsstrahlung production in the electric field of a nucleus was initially developed by Bethe and Heitler [74]. Derived for the screened nucleus using the first Born approximation, the cross section, differential in emitted photon energy, is written as follows:

$$\frac{\mathrm{d}\sigma_{brem}(Z,E_0,k)}{\mathrm{d}k} = \frac{A'(Z,E_0)r_0^2\alpha Z\{Z+\xi(Z)\}}{k} \times \left\{\left(1+(E/E_0)^2\right)\left[\phi_1(\delta)-\frac{4}{3}\ln Z-(4f_c(Z) \text{ if } E_0>50 \text{ MeV})\right] - \frac{2}{3}\frac{E}{E_0}\left[\phi_2(\delta)-\frac{4}{3}\ln Z-(4f_c(Z) \text{ if } E_0>50 \text{ MeV})\right]\right\}, \quad (3.27)$$

where k is the emitted photon energy, Z is the atomic number of the transport material, E_0 is the electron energy before interaction, E is the electron energy after interaction, $A'(Z,E_0)$ is an empirical correction factor described below, r_0 is the classical electron radius (2.82×10^{-13} cm), α is the fine-structure constant (1/137), $\xi(Z)$ is a correction factor to account for the three-body process, $f_c(Z)$ is a theoretical Coulomb correction valid only at high energies (>50 MeV) [75], and $\phi_1(\delta)$ and $\phi_2(\delta)$ are screening functions. Using the Thomas-Fermi form factors, $\phi_1(\delta)$ and $\phi_2(\delta)$ have been evaluated by Butcher and Messel [76] and are given by:

$$\phi_1(\delta) = (20.867-3.242\delta+0.625\delta^2 \text{ if } \delta\le 1, \text{ otherwise } 21.12-4.184\ln(\delta+0.952)) \quad (3.28)$$

and

$$\phi_2(\delta) = (20.029-1930\delta-0.086\delta^2 \text{ if } \delta\le 1, \text{ otherwise } 21.12-4.184\ln(\delta+0.952)), \quad (3.29)$$

where

$$\delta = 136Z^{-1/3}\frac{km_0c^2}{E_0E}. \quad (3.30)$$

Bethe obtained the bremsstrahlung cross section in Eqn. 3.27 using a high-energy approximation, *i.e.*, assuming that the energy of the transported electron both before and after the bremsstrahlung event is large compared to m_0c^2. At lower energies, *i.e.*, for $E_0 < 50$ MeV, an empirical correction factor $A'(Z, E_0)$ has been added to the high-energy cross section to get improved agreement with experiment. In the default version of **EGS4**, the correction factor is crudely evaluated using very sketchy data from curves found in Koch and Motz [77]. However, users now have the option [71] of replacing these old $A'(Z, E_0)$ values by a more extensive set that is based on data presented in *ICRU-37* [70]. At $E_0 > 50$ MeV, $A'(Z, E_0) = 1$.

It should be noted that only the energy distribution of newly created bremsstrahlung photons is determined using the cross section in Eqn. 3.27. The angular distribution has been treated separately. In the default version of **EGS4**, the algorithm currently employed is to set all newly created photons in motion at a fixed angle with respect to the transported electron direction. This fixed angle has the form $\theta = 1/E_0$, where θ is the scattering angle (radians) and E_0 is the total energy of the transported electron in units of m_0c^2. The angle represents an estimate of the expected *average* scattering angle.

Realizing that the angular sampling may be oversimplified for some applications, Bielajew *et al.* have written an improved angular sampling routine [78]. It is based on the following cross section, differential in photon energy and angle, from Koch and Motz [77]:

$$\frac{\mathrm{d}^2\sigma_{brem}}{\mathrm{d}k\mathrm{d}\theta} = \frac{4Z^2r_0^2}{137}\frac{\mathrm{d}k}{k}y\mathrm{d}y\left\{\frac{16y^2E}{(y^2+1)^4E_0} - \frac{(E_0+E)^2}{(y^2+1)^2E_0^2} + \left[\frac{E_0^2+E^2}{(y^2+1)^2E_0^2} - \frac{4y^2E}{(y^2+1)^4E_0}\right]\ln M(y)\right\}, \tag{3.31}$$

where k is the energy of the emitted photon, θ is the angle between the outgoing photon and the incoming electron directions (radians), Z is the atomic number of the transport material, r_0 is the classical electron radius, E_0 and E are the initial and final energies of the transported electron, $y = E_0\theta$, and

$$\frac{1}{M(y)} = \left(\frac{k}{2E_0E}\right)^2 + \left(\frac{Z^{1/3}}{111(y^2+1)}\right)^2. \tag{3.32}$$

The suitability of Eqn. 3.31 for use over a wide range of energies in high and low Z materials remains to be proven. Essential approximations used to derive the cross section include: (1) an approximate screening potential, (2) the Born approximation, (3) a small angle approximation, and (4) an extreme relativistic assumption. Koch and Motz present encouraging data that demonstrate agreement between experiment

and Eqn. 3.31 for 4.5 MeV electrons on Au [77]. Although use of the equation violates all 4 constraints in the cases they showed, the deviation was at worst 10% (at large angles) and usually much better [77].

Other important approximations used to model the production of bremsstrahlung in **EGS4** include the following:

1. The electron is not deflected by the bremsstrahlung interaction.
2. Electrons and positrons are treated equally with respect to bremsstrahlung production. Actually, at low energies, positron bremsstrahlung is suppressed relative to electron bremsstrahlung.
3. Electrons are not allowed to convert all their kinetic energy into bremsstrahlung.

3.5.2 Knock-on electron production

The production of knock-on electrons, in **EGS4**, refers to the creation of secondary electrons with energy above the user-supplied threshold **AE**. The knock-on electrons result from collisions with atomic electrons in which the energy transfer is sufficient to eject the target electron the atom. If the ejected electron energy is below **AE**, then it is not "created," and the collision is treated instead as part of the continuous energy loss process. However, if the ejected electron energy is above the threshold, then the secondary particle is created and the energy and direction of the primary electron are adjusted accordingly. For the primary electron, the final energy E_f is given by:

$$E_f = E_0 - tS - E_{knock-on}, \tag{3.33}$$

where E_0 is the initial energy, t is the length of curved path taken by the electron, S is the energy-averaged stopping power which accounts for energy lost during the step to sub-threshold events, and $E_{knock-on}$ is the energy transferred to the knock-on electron.

The knock-on collision is treated as obeying the Møller cross section [65], which has been derived on the assumption that the target electron is free and initially at rest. When the energy transfer is large compared to the binding energy of the atomic electron, this is a good approximation. The differential cross section is given by:

$$\frac{\mathrm{d}\Sigma_{Moller}}{\mathrm{d}E_{knock-on}} = \frac{2\pi e^4}{mv^2(E_{initial} - mc^2)^2} NZ \left[C_1 + \frac{1}{\varepsilon}\left(\frac{1}{\varepsilon} - C_2\right) + \frac{1}{\varepsilon'}\left(\frac{1}{\varepsilon'} - C_2\right)\right], \tag{3.34}$$

where e is the charge of an electron, m is the mass of the transported electron, v is its velocity, $C_1 = [(\gamma-1)/\gamma]^2$ and $C_2 = (2\gamma-1)/\gamma^2$ with γ equal to E_0/m, and where ε is the fraction of the primary electron kinetic energy lost to the knock-on electron, and ε' is the fraction of primary electron kinetic energy remaining.

By convention, the slower of the two electrons after the collision is considered to be the secondary electron. The minimum and maximum energies it may be created with are AE and $(T_0/2 + m)$, respectively. The total discrete Møller cross section is then obtained as follows:

$$\Sigma_{Moller} = \int_{AE}^{(T_0/2+m)} \frac{d\Sigma_{Moller}}{dE_{knock-on}} dE_{knock-on}. \tag{3.35}$$

The scattering angles of both electrons are determined using conservation of energy and momentum relations.

3.6 Boundary Crossing and Scoring

At this point, it is worth repeating that users of EGS4 are responsible for writing their own coding of boundary crossing and scoring algorithms. As described in Section 3.3, the code itself is equipped to simulate only the physics of electron and photon transport, *i.e.*, it does not set up the simulation geometry or tabulate a standard collection of output data. The reader therefore is advised that the following discussion on boundary crossing and scoring is restricted to the L-EGS *user code* [79] operational in the Whitaker College Biomedical Imaging and Computation Laboratory at MIT (Cambridge, MA) and may not apply to other user codes.

With that said, boundaries in EGS4 are used to define the interfaces between regions composed of different materials and the interfaces between scoring regions, even if they are made of the same material. As a result, boundaries are encountered in EGS4 in both homogeneous and heterogeneous media.

As described in Section 3.4.2, a single electron transport step size is chosen as the minimum of: (1) the distance d to the next catastrophic interaction (randomly sampled using the total cross section σ_t), (2) the maximum multiple scattering substep size (limited by the Moliére theory to be less than t_{max} and possibly by the user to be less than ESTEPE), and (3) the straight-line distance in the current direction to the nearest boundary.

Given that the minimum distance is that to the next catastrophic interaction or that limited by either t_{max} or ESTEPE, then the transport is handled as described in Section 3.4.2. If, instead, the minimum distance is that to the nearest boundary, then the electron is transported to the boundary and the simulation proceeds as follows. Energy lost by the electron due to subthreshold interactions occurring along its step to the boundary is deposited in the current region. In addition, the electron's direction is adjusted to account for multiple scattering along the step. (It is worth noting that this adjustment requires a multiple scattering algorithm which can be applied—during simulation—to sample the angular deflection for any one of a range

Chapter 4

Monte Carlo Estimates of Beta Dosimetry

4.1 Introduction

In general, Monte Carlo radiation transport codes provide information on particle "histories," and users of the codes may use this information to produce any of a wide variety of results. A particle history contains sufficient information to describe in detail all the changes a particle undergoes while travelling through an absorbing medium. For example, a history includes information on the energy and direction of the particle at the end of each step in its "walk" through the simulation geometry, as described in Chapter 3. A history also includes information on the positions at which secondary radiations are formed and the changes they undergo while travelling through the system. In principle, the history information can be used to address a variety of problems that are of interest in dosimetry.

In this chapter, use of the **EGS4** Monte Carlo radiation transport code to evaluate beta dosimetry in radiation synovectomy is described. The chapter begins with a presentation of the mathematical joint model used in the simulations and includes discussions of various simulation parameters and the approach used to convert raw **EGS4** output to data which are of dosimetric interest. Investigations of backscatter contributions to synovial dose and the effect of disease progression on dosimetry in radiation synovectomy also are discussed.

point; energy and direction probability distribution functions for multiply-scattered electrons; and the possible production of bremsstrahlung photons and knock-on electrons. With this information, the entire experience an electron undergoes from the time it is created to the time it is absorbed or passes of the system can be simulated. In the next Chapter, use of Monte Carlo electron transport simulation to estimate the beta-particle dosimetry of various radionuclides of interest in radiation synovectomy is described.

PAGES (S) MISSING FROM ORIGINAL

PAGE 63

4.2 Materials and Methods

4.2.1 Mathematical joint model

The mathematical model developed for the Monte Carlo simulations is a planar model of the rheumatoid joint. It is shown in Figure 4-1 along with an inset which illustrates the juxtaposition and relative size of synovial joint tissues in the region of interest. Dimensions in the model (*e.g.*, thickness of articular cartilage, thickness of joint capsule, etc.) were selected to correspond with those typically found in larger joints (*e.g.*, the knee, shoulder, or hip) since these are the joints which have been most commonly treated with radiation synovectomy [8]. Each of the dimensions is described below.

In the model, bone (lined at the surface with 1 mm articular cartilage) is separated by the joint capsule from soft tissue, which represents synovium. The synovium is sub-divided into a surface layer of lining cells and underlying sub-synovium. Distances in the model are defined in relation to the articular cartilage-joint capsule interface.

Prior to administration of radioactivity, rheumatoid joints to be treated with radiation synovectomy generally are aspirated of all fluid [17]. Radioactivity, held in a liquid suspension, then is injected into the joint capsule where it makes direct contact with inflamed synovium [1]. Phagocytic lining cells along the synovial surface quickly absorb radioactive particulate from the capsule. Autoradiographs of the tissue lining in knees injected with various radionuclides have shown a reasonably even distribution of radioactivity in these cells for several days after injection [2, 3, 4]. The ends of the articulating bony surfaces, capped with articular cartilage, do not absorb the radioactive particulate however since the cells along these surfaces are not phagocytic [46].

In the model, the radiation source lies uniformly distributed throughout both the joint capsule and lining cells regions. The joint capsule was modeled as a 0.44 mm thick slab of water between the articular cartilage and synovium. The layer of lining cells along the synovial surface was modeled as a 0.30 mm thick slab of tissue. In healthy synovial joints, the lining cells generally are arranged at the surface in a layer 1 to 3 cells thick. In rheumatoid joints, their numbers are greatly increased, occasionally reaching a thickness of 10 to 20 cells [80]. In the model, a layer 15 cells thick is assumed. A diameter of 20 μm per cell yields a thickness of lining cells in the model equal to 0.30 mm.

It is worth noting that, since the range of the emitted beta-particles typically used in radiation synovectomy is so short (average range in tissue < 5 mm), it is not necessary to model the three-dimensional structure of the entire synovial joint. Instead, only the structures located within the range of the emitted particles (*e.g.*, the first few mm of bone, the layer of articular cartilage, the joint capsule, and the first few mm of synovium) need to be modeled. Total tissue volumes are taken into

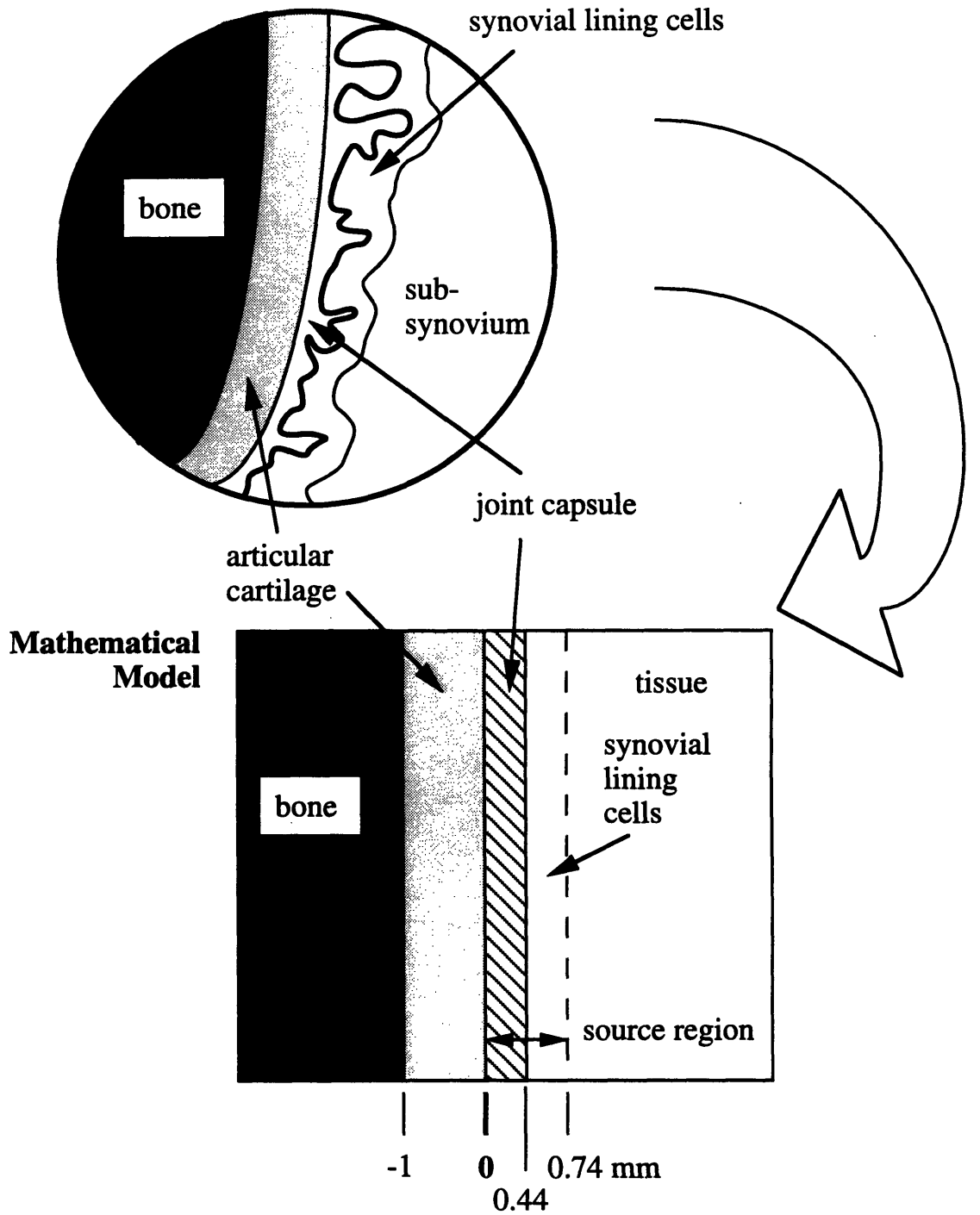

Figure 4-1: Mathematical model of the rheumatoid synovial joint.

Table 4.1: Elemental compositions and densities of the four absorbing media used in the joint model. Adopted from *ICRU-44*.

Element	Bone	Art cart	Tissue	Joint fluid
H	3.4%	9.6	10.0	11.1
C	15.5	9.9	14.9	–
N	4.2	2.2	3.5	–
O	43.5	74.4	71.6	88.9
Na	0.1	0.5	–	–
Mg	0.2	–	–	–
P	10.3	2.2	–	–
S	0.3	0.9	–	–
Ca	22.5	–	–	–
Cl	–	0.3	–	–
ρ	1.92 g/cm^3	1.1 g/cm^3	1.0 g/cm^3	1.0 g/cm^3

account, however, in extrapolating beta dose distributions in treated joints from the Monte Carlo results (see Section 4.2.5.

4.2.2 Tissue cross sections

Because Monte Carlo radiation transport calculations often tend to be very time consuming, the EGS4 code comes equipped with a preprocessor, PEGS4, which uses theoretical (and sometimes empirical) formulas to compute numerous physical quantities, *e.g.*, cross section data and branching ratios for each of the absorbing media [54]. The elemental compositions and densities required by PEGS4 to compute these data for the model's tissues were adopted from *ICRU-44: Tissue substitutes in radiation dosimetry and measurement* [81] and are listed in Table 4.1.

Use of the preprocessor requires the user to input values for various parameters. All the PEGS4 data described here were prepared with the list of parameter values shown in Table 4.2. For instance, tissue cross section data for electrons and photons were prepared over the kinetic energy range 1 keV to 10 MeV. In addition, the flag IAPRIM was set equal to 1, instructing the preprocessor to normalize the cross sections for bremsstrahlung production so that the calculated radiative stopping power data are identical to the data presented in *ICRU-37* [70, 71], as described in Section 3.4.4. The radiative stopping power data tabulated in *ICRU-37* generally are considered to be the most accurate data available [72].

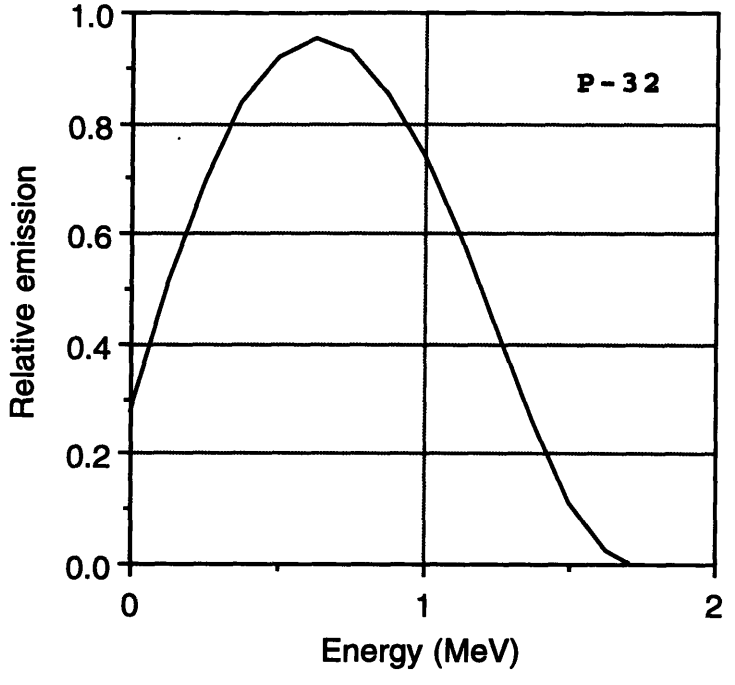

Figure 4-2: Beta spectrum for ^{32}P. Adopted from Hogan *et al.*

Table 4.2: Parameter values used in PEGS4 to compute tissue cross section data.

Parameter	Value used
Lower energy for electron data (AE)	1 keV
Lower energy for photon data (AP)	1 keV
Upper energy for electron data (UE)	10 MeV
Upper energy for photon data (UP)	10 MeV
IAPRIM	1

4.2.3 Radionuclide spectra

The radionuclides investigated in this work include all those listed in Table 2.3 as being radionuclides of interest in radiation synovectomy. As mentioned in Section 2.4.1, these 8 beta-emitters either have been used in clinical trials or are of interest due to their favorable half-lives, emission energies, and radiochemistry.

The beta-spectral characteristics of the 8 radionuclides are well documented by Hogan *et al.* [82] and are shown in Figures 4-2 through 4-9. During the Monte Carlo simulations, initial kinetic energies of starting beta-particles (see below) were determined by randomly sampling the appropriate spectrum. Although some of the radionuclides decay with accompanying gamma-ray emission, the corresponding photon dose to the tissues represented in the model was not calculated. For the small volume under investigation however, the absorbed dose due to the emitted photons is expected to be very small compared to that due to beta particles.

4.2.4 Computer simulations

Using EGS4 and the mathematical joint model shown in Figure 4-1, beta-particle emission from within the radiation source region and subsequent transport of the emitted particles through the joint model was simulated, one radionuclide at a time. Simulation begins by choosing a starting position, direction, and energy for the emission of a single beta-particle from the decaying radionuclide. The starting position is a point randomly selected from the 0.74 mm thick radiation source region (0.30 mm joint capsule region plus 0.44 mm lining cells region). The starting direction is chosen at random over 4π space. The initial kinetic energy of the emitted beta-particle is determined by randomly sampling the radionuclide's decay spectrum.

The emitted beta-particle then is transported through the joint model by the EGS4 code, as described in Chapter 3. During the transport simulation, the code keeps track of the amount of energy deposited by the particle and all its secondaries in each of the 4 absorbing media: bone, articular cartilage, the fluid-filled joint capsule, and tissue

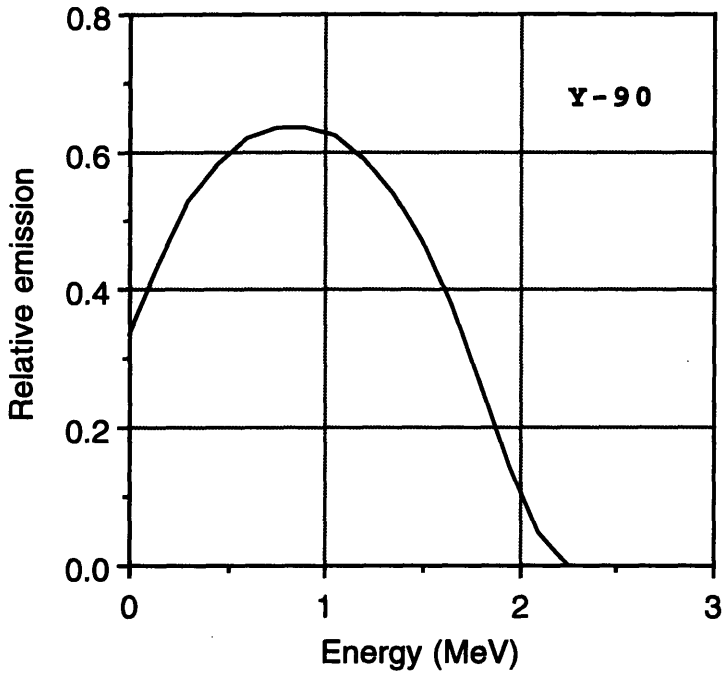

Figure 4-3: Beta spectrum for ^{90}Y. Adopted from Hogan *et al.*

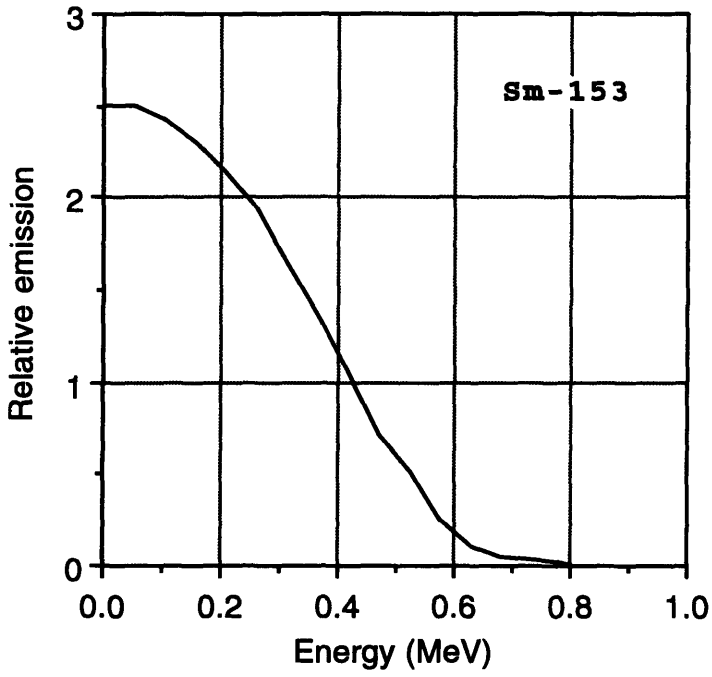

Figure 4-4: Beta spectrum for ^{153}Sm. Adopted from Hogan *et al.*

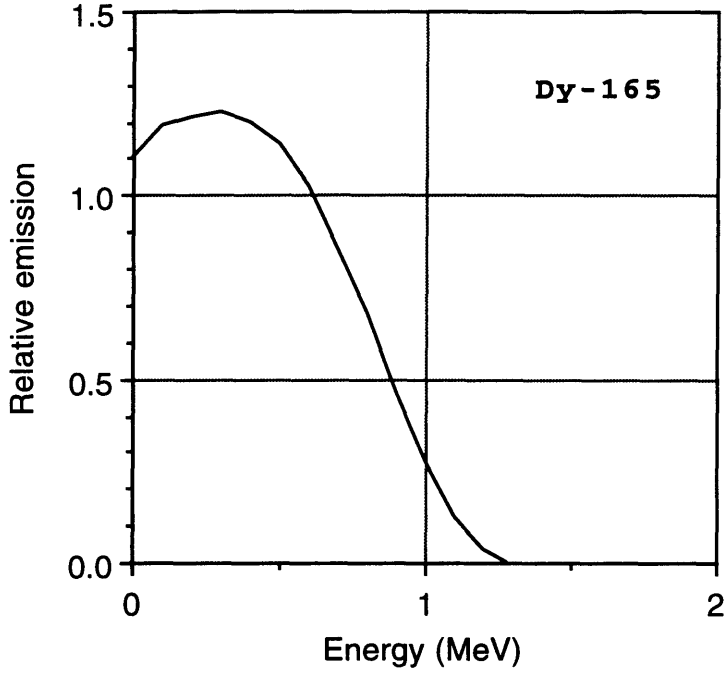

Figure 4-5: Beta spectrum for ^{165}Dy. Adopted from Hogan *et al.*

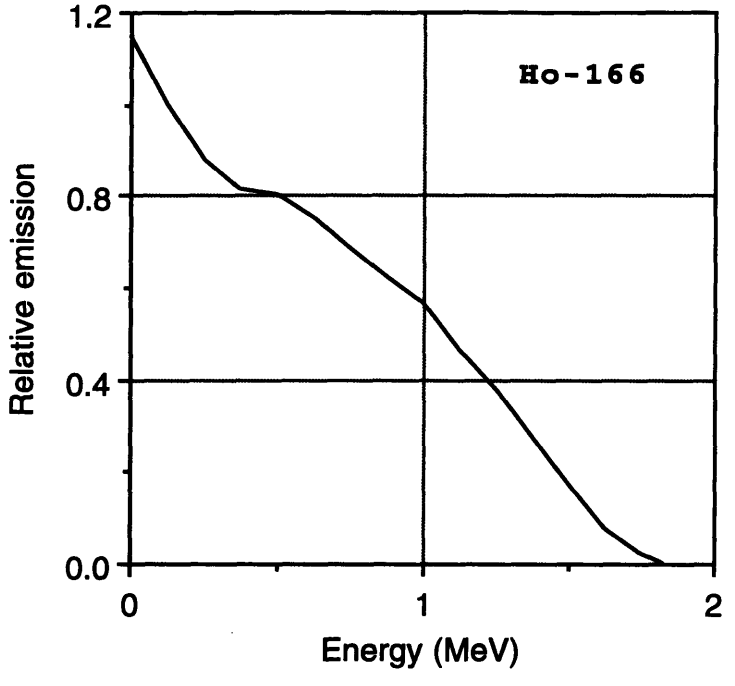

Figure 4-6: Beta spectrum for ^{166}Ho. Adopted from Hogan *et al.*

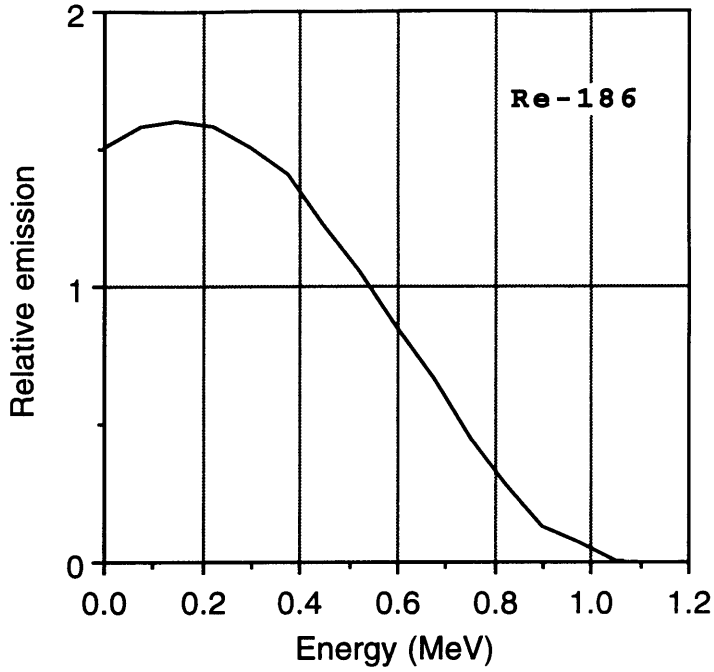

Figure 4-7: Beta spectrum for ^{186}Re. Adopted from Hogan *et al.*

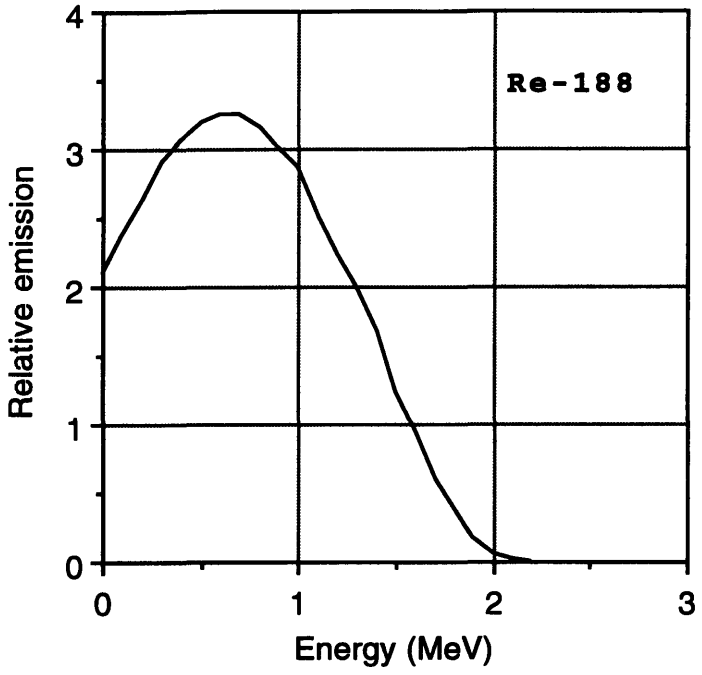

Figure 4-8: Beta spectrum for ^{188}Re. Adopted from Hogan *et al.*

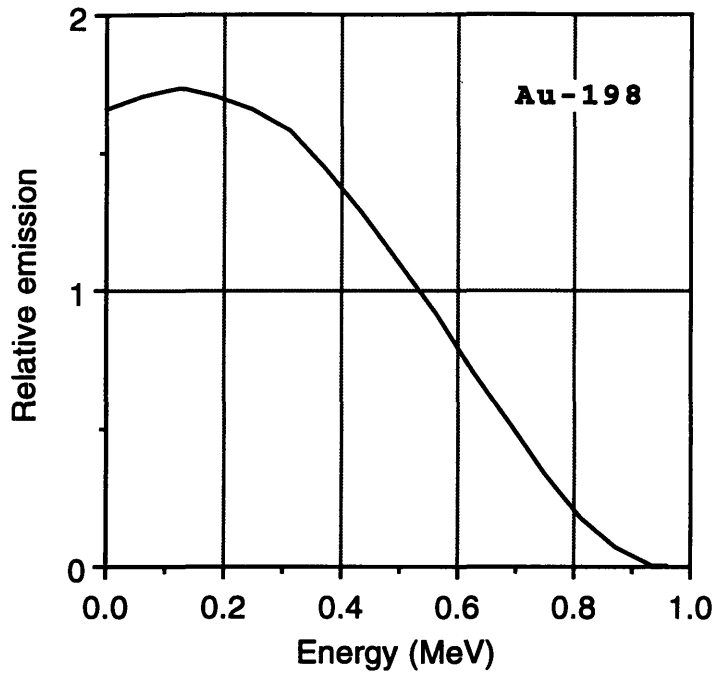

Figure 4-9: Beta spectrum for ^{198}Au. Adopted from Hogan *et al.*

(synovium). To increase the usefulness of the results, the 4 absorbing media were sub-divided into 50 smaller bins. Total energy deposited by the transported particles was tallied separately for each bin (see Section 3.6).

Deposited energy was converted to an absorbed dose factor for each bin according to the following relation:

$$F_i = \Delta E_i \frac{\kappa}{\Delta T_i \rho_i N}, \tag{4.1}$$

where F_i is the absorbed dose factor for the i^{th} bin (cGy-cm^2/MBq-s), ΔE_i is the energy deposited in the bin (MeV), κ is a unit conversion constant, ΔT_i is the thickness of the bin (cm), ρ_i is the density of the absorbing medium in the bin (g/cm^3), and N is the number of nuclear disintegrations, integrated over time (MBq-s). Nuclear disintegrations which do not result in the emission of a beta-particle were taken into account.

The outermost bins were each 0.025 cm thick, while the innermost bins generally were 0.020 cm thick. Two exceptions are the 2 joint capsule bins which each are 0.022 cm thick and the lining cells bin which is 0.030 cm thick.

4.2.5 Dose estimates

Radiation doses throughout treated joints can be estimated as a function of time using the absorbed dose factors described above. For any location in the joint model and at any time t after injection, the beta dose from injected radioactivity is calculated as the product of the cumulated activity $\tilde{A}(t)$ in the source region and the bin's absorbed dose factor F_i divided by an estimate of the joint's total synovial surface area S_{syn}, so that:

$$D_i(t) = \frac{\tilde{A}(t) F_i}{S_{syn}}. \tag{4.2}$$

The cumulated activity after time t is given by:

$$\tilde{A}(t) = \frac{A_0}{\lambda_P}(1 - e^{-\lambda_P t}), \tag{4.3}$$

where A_0 is the activity initially deposited in the source region and λ_P is the injected radionuclide's physical decay constant, given by:

$$\lambda_P = \frac{\ln 2}{T_P}, \tag{4.4}$$

where T_P is the physical half-life of the radionuclide.

For a very long time relative to the half-life, Eqn. 4.3 reduces to $\tilde{A}(t) = A_0 \div \lambda_P$,

and the total radiation dose D_i becomes:

$$D_i = \frac{A_0 F_i}{\lambda_P S_{syn}}. \tag{4.5}$$

A very long time relative to the half-life, for most purposes, can be taken to mean any time t greater than six half-lives, which for the short-lived emitters commonly used in radiation synovectomy is on the order of 1 to 20 days.

Although leakage of radioactivity from the joint was not included in the Monte Carlo simulations directly, accommodations for leakage can be made in the dose estimates. For instance, to accommodate a reduction in dose due to leakage of activity from the joint, the physical decay constant in Eqn. 4.3 can be replaced with an effective decay constant λ_E given by:

$$\lambda_E = \ln 2 \left[\frac{T_P + T_B}{T_P T_B}\right], \tag{4.6}$$

where T_B is the biological half-life of the radionuclide in the joint. Physically, T_B represents the length of time required for one-half the radioactivity present to be removed through leakage. The resulting equation for estimating absorbed dose distributions in treated joints as a function of time then is given by:

$$D_i(t) = \frac{A_0 F_i}{\lambda_E S_{syn}}(1 - e^{-\lambda_E t}). \tag{4.7}$$

The activity required to deliver a prescribed synovial dose to the i^{th} bin $D_i(t)$ (accommodating leakage) can be determined by solving Eqn. 4.7 for A_0.

4.2.6 Dose rate estimates

Dose rates throughout treated joints also can be estimated using the absorbed dose factors described above. For instance, the initial dose rate $\dot{D}_i(0)$ from injected radioactivity to any location i in the joint model is calculated as:

$$\dot{D}_i(0) = \frac{A_0 F_i}{S_{syn}}. \tag{4.8}$$

And the dose rate at a later time t is given by:

$$\dot{D}_i(t) = \frac{A_0 F_i}{S_{syn}}(1 - e^{-\lambda_E t}), \tag{4.9}$$

where λ_E is the effective decay constant.

4.2.7 Backscatter contributions to absorbed dose

In a related investigation, the joint model was used to evaluate the contribution of radiation backscatter to total synovial dose. Backscattered dose can be defined as the absorbed dose deposited in the synovium resulting from radiation that is scattered back from bone into the synovium.

To calculate the backscattered dose, the simulation was run once as described above with bone, articular cartilage, joint capsule, and tissue (synovium) in place and again with the bone and articular cartilage regions replaced by soft tissue, yielding a more homogeneous structure. Doses in bins of the tissue-on-tissue model were subtracted from those in corresponding bins of the tissue-on-bone model. The resulting backscattered dose was divided by the dose from the tissue-on-tissue simulation to yield a percentage backscatter figure, given by:

$$B_i = \left[\frac{D_{b,i} - D_{h,i}}{D_{h,i}}\right] \times 100\%, \tag{4.10}$$

where B_i is the percent increase in dose to synovium in the i^{th} bin due to radiation backscattered from bone, $D_{b,i}$ is the dose to synovium in the i^{th} bin when the bone and articular cartilage regions are present, and $D_{h,i}$ is the dose to synovium in the i^{th} bin when the bone and articular cartilage have been replaced by tissue, yielding the more homogeneous structure.

4.2.8 Effect of disease progression on dosimetry

Monte Carlo simulation also was used to evaluate the effect of disease progression on beta dose distributions in radiation synovectomy. As with other forms of therapy, the likelihood of clinical success has been shown to decrease as the extent of rheumatoid arthritis progression in the joint prior to treatment increases [26]. To determine whether the correlation can be attributed to structural changes in the joint which result in less effective absorbed dose distributions, additional simulations were run using models developed to represent rheumatoid joints at varying stages of disease progression.

In all, three stages of rheumatoid arthritis progression were modeled. They are distinguished by different volumes of fluid in the joint capsule and different numbers of lining cells along the synovial surface, as shown in Table 4.3. The increasing joint fluid volumes result in a thicker and thicker joint capsule, from 0.35 mm in a stage 1 joint, to 0.44 mm at stage 2, to 0.53 mm at stage 3. The increasing numbers of lining cells result in a thicker and thicker lining cells region. Assuming a cell diameter of 20 μm, corresponding thicknesses of the lining cells regions are 0.20 mm in a stage 1 joint, 0.30 mm at stage 2, and 0.40 mm at stage 3.

Table 4.3: Characteristics of the three stages of advancing rheumatoid arthritis used in the computer simulations.

Stage	Fluid volume	Lining cells
1	4 cm^3	10 cells
2	5	15
3	6	20

Table 4.4: Parameter values used in the EGS4 simulations.

Parameter	Value used
Maximum energy loss per step (ESTEPE)	0.02 (2%)
Electron cutoff energy (ECUT)	10 keV
Photon cutoff energy (PCUT)	10 keV
Number of histories	100,000
IRAYL	1

4.2.9 Simulation parameters

Use of the EGS4 code requires the user to input values for various parameters. All simulations described here were run with the list of parameters values shown in Table 4.4.

The simulations were performed on SunSparc workstations in the Whitaker College Biomedical Imaging and Computation Laboratory at MIT (Cambridge, MA). For each of the 8 radionuclides investigated, 100,000 starting particles were generated and followed to completion in the joint model. The maximum energy loss per electron transport step (ESTEPE) was limited to 2% of the electron's total energy. As recommended in Section 3.4.5, an investigation was conducted to ensure that the amount of energy deposited in each of the scoring bins was not affected by this choice of ESTEPE.

The transport cutoff energy for both electrons (ECUT) and photons (PCUT) was 10 keV. Although photons emitted by decaying radionuclides (*e.g.*, the 95 keV gamma-ray emitted in 3.6% of ^{165}Dy decays) were not included in the simulations, bremsstrahlung photons were both produced and transported. The photon transport continued until: (1) the photons left the simulation geometry, (2) they were absorbed, or (3) their energy fell below the low-energy cutoff PCUT. In addition, the flag IRAYL was set equal to 1, instructing the code to include Rayleigh, or coherent, scattering of photons.

Typical estimates of uncertainty in the calculated values of F_i were 1-2% in the

bins nearest (within 2 mm of) the source region and 5-10% in the bins farther (greater than 2 mm) from the source region. The uncertainty was estimated by dividing the total number of source particles into four equal groups. Energy deposition for each group was scored separately. At the end of simulation, the results were used to calculate an average absorbed dose factor and associated standard deviation for each bin.

4.3 Results

Results are presented in Figures 4-10 through 4-17 as absorbed dose factors (cGy-cm^2/MBq-s) versus depth in bone, articular cartilage, the joint capsule, and synovium. Analogous to the volumetric "S" factor used in MIRD calculations [83], the absorbed dose factors also lend themselves to clinical application. For example, consider the injection of 270 MBq (10 mCi) ^{198}Au into the knee, one of the earliest treatments reported to provide a beneficial effect in clinical trials [33]. If uniform distribution along 250 cm^2 of synovium is assumed [9], one can use Figure 4-17 and Eqn. 4.8 to calculate that the initial dose rate to the region of lining cells along the synovial surface is 0.055 cGy/s (200 rad/h); to the bone surface it is 0.003 cGy/s (9 rad/h). Integrating over time, the total dose to the lining cells is 18,000 cGy (from Eqn. 4.5); to the bone surface it is 1000 cGy.

The calculation assumes that all the ^{198}Au remains in the joint until decay. In practice, the potential for leakage from the joint via the lymphatic system must always be considered. Leakage however can be highly variable from joint to joint and from patient to patient. The calculations presented here therefore should be corrected for leakage on an individual basis. Continuing the sample calculation, Topp *et al.* [3] reported that for 18 knees the extra-articular spread of ^{198}Au at 24 h after injection varied from as low as 1% of the injected activity to as high as 34%. These data indicate that the biological half-life for removal of activity from the joint varied from 1700 h down to 40 h. For T_B equal to 1700 h, the absorbed dose estimates remain unchanged. For T_B equal to 40 h, on the other hand, the corrected absorbed dose estimates for the lining cells and bone surface are, respectively, 7000 cGy and 400 cGy, which represent a significant change.

As a second example, consider the injection of 74 MBq (2 mCi) ^{153}Sm into a smaller joint, *e.g.*, the wrist. From Figure 4-12, the absorbed dose factor for the lining cells region is 0.031 cGy-cm^2/MBq-s. If uniform distribution along 50 cm^2 of synovial surface is assumed, the initial dose rate to the lining cells is 0.05 cGy/s (170 rad/h), from Eqn. 4.8. Assuming no leakage, the total lining cells dose delivered over time is 11,000 cGy, from Eqn 4.5. Note that, in this example, the bone surface is not expected to receive any beta dose, since the low-energy beta-particles emitted by ^{153}Sm are not sufficiently energetic to penetrate the 1 mm thick layer of articular

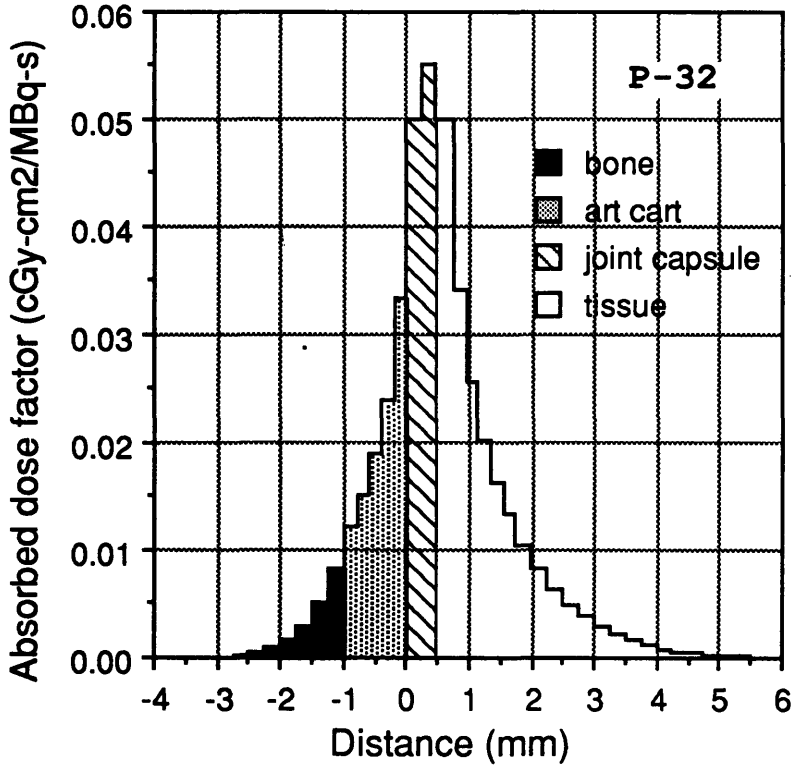

Figure 4-10: Absorbed dose factors versus distance in the joint model for ^{32}P.

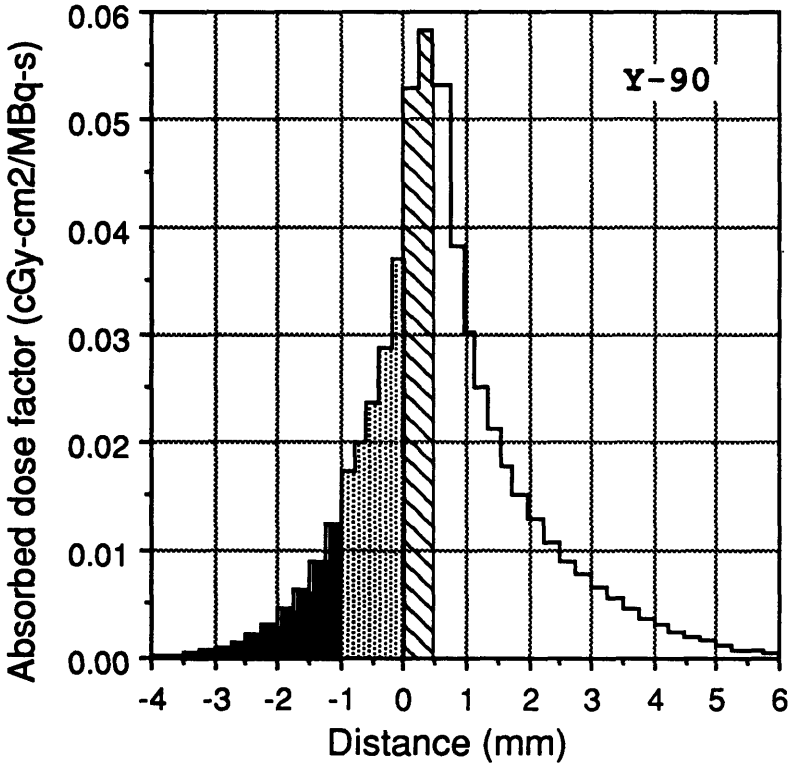

Figure 4-11: Absorbed dose factors versus distance in the joint model for ^{90}Y.

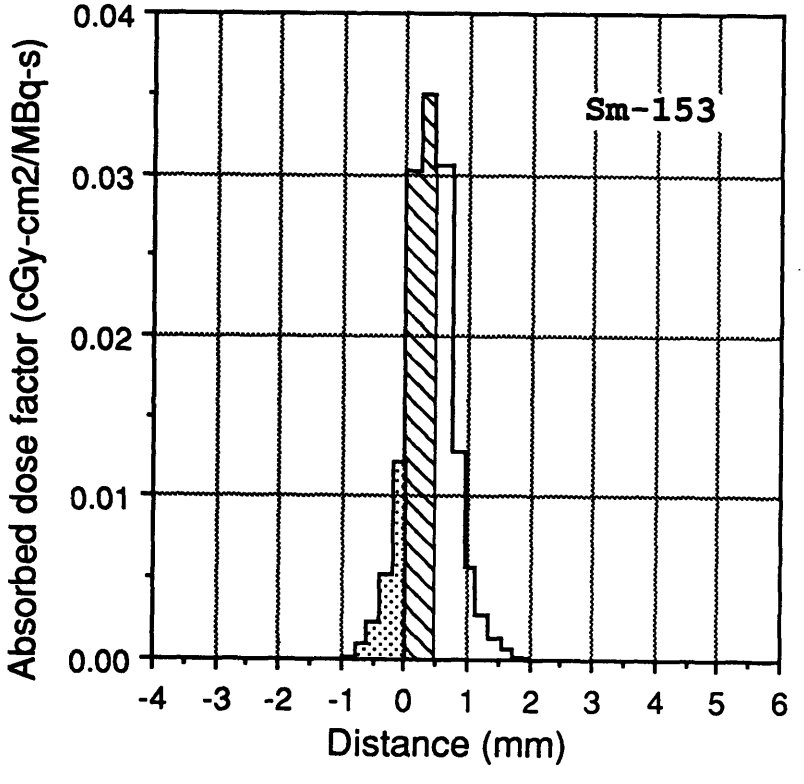

Figure 4-12: Absorbed dose factors versus distance in the joint model for ^{153}Sm.

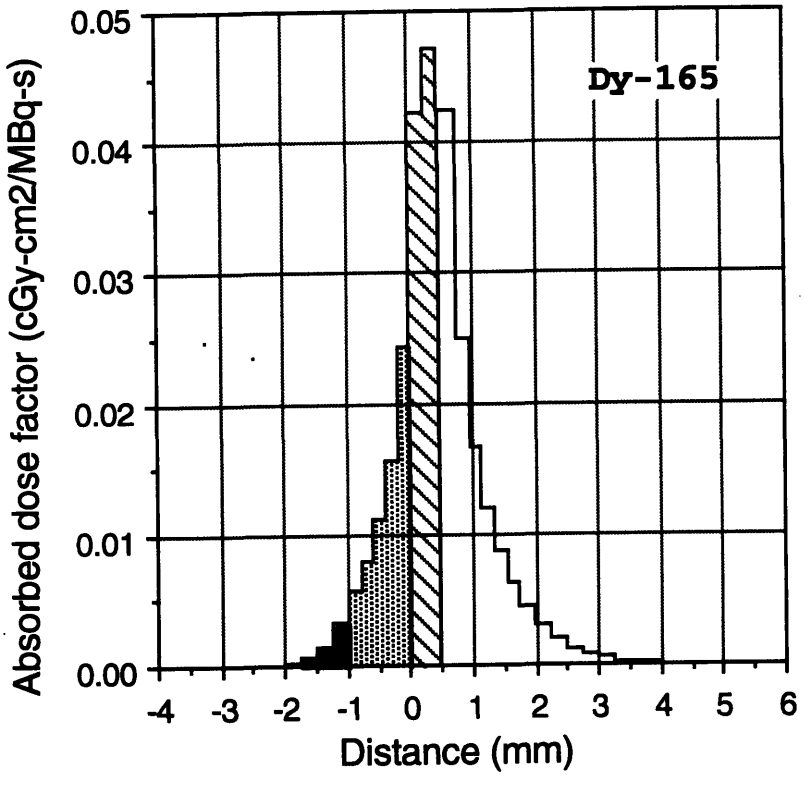

Figure 4-13: Absorbed dose factors versus distance in the joint model for ^{165}Dy.

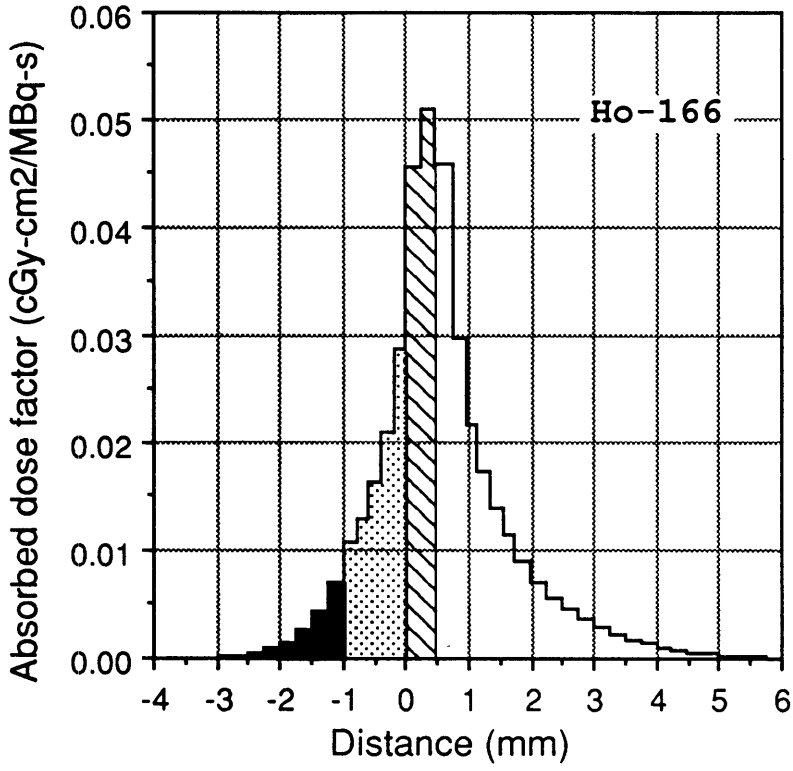

Figure 4-14: Absorbed dose factors versus distance in the joint model for ^{166}Ho.

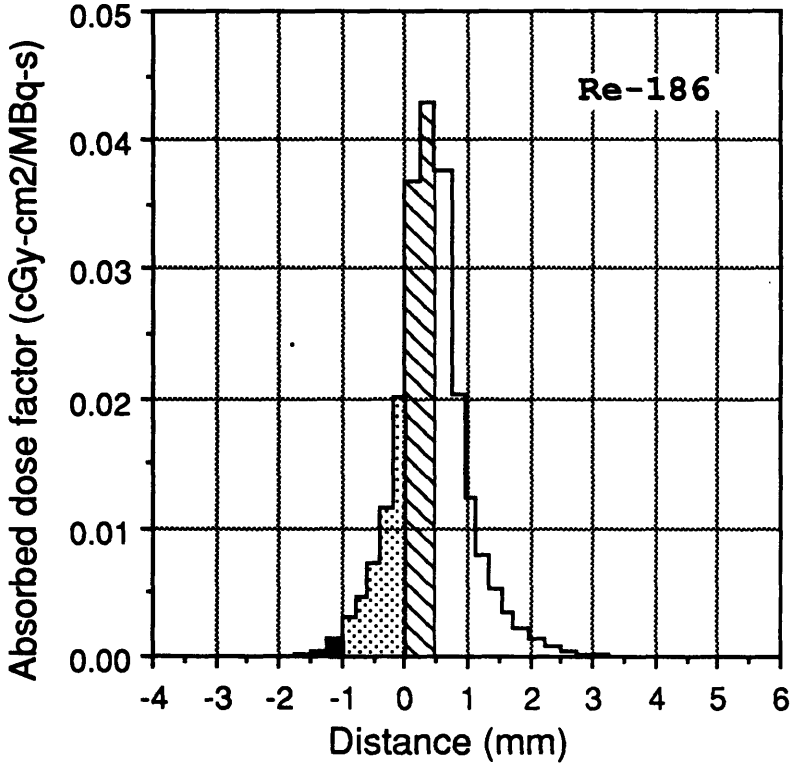

Figure 4-15: Absorbed dose factors versus distance in the joint model for ^{186}Re.

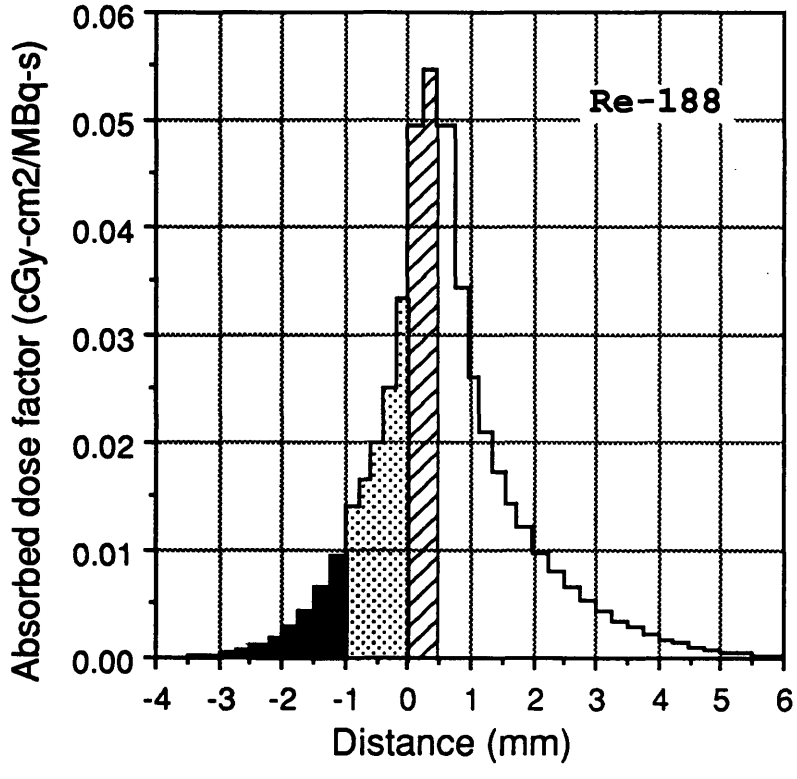

Figure 4-16: Absorbed dose factors versus distance in the joint model for ^{188}Re.

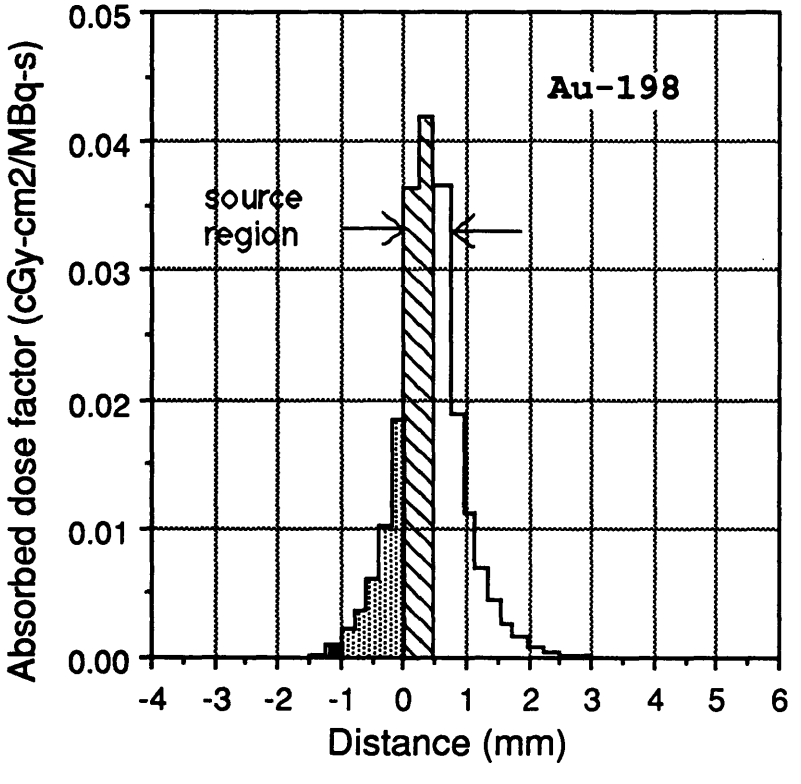

Figure 4-17: Absorbed dose factors versus distance in the joint model for ^{198}Au.

cartilage.

4.3.1 Absorbed dose factors versus distance

From the results presented in Figures 4-10 through 4-17, one can see that the plots of absorbed dose factors versus distance in the joint model can be described as having three distinct regions. One region (0.0 to 0.74 mm) is characterized as having dose factors which are significantly higher than those in the remaining regions. This is the radiation source region and, physically, it represents the joint capsule and lining cells regions found in all synovial joints. Because it is the source region, it can be expected to receive a beta dose significantly higher than that in other parts of the joint. Clinically, the high dose imparted to the lining cells may be advantageous, since it is the lining cells which are responsible for secreting proinflammatory cytokines and destructive enzymes thought to play a major role in bone and articular cartilage degradation (see Chapters 2 and 6). Killing the lining cells therefore may slow the development of bone and articular cartilage destruction, at least temporarily.

The second region in the plots includes, on one side of the source, the dose factors at distances between -1.0 and 0.0 mm and, on the other side, the factors at distances between 0.74 and 6.0 mm. Physically, these two areas represent, respectively, the articular cartilage and sub-synovium components in synovial joints. In both, the absorbed dose factors are seen to decrease exponentially with distance. The rate of decrease is influenced by the mean beta energy of each radionuclide.

The third region in the plots includes the dose factors at distances between -6.0 and -1.0 mm; it physically represents bone. As in the regions of articular cartilage and sub-synovium, the decrease in dose factors with distance in bone is seen to be exponential and dependent on the radionuclide's mean beta energy. The dose factors in this region are recognized as being distinct however due to the discontinuity at the bone-articular cartilage interface (at -1.0 mm). The discontinuity is due to differences in the stopping powers of the two absorbing media.

4.3.2 Backscatter

The concept of backscatter is useful for illustrating the effect of the presence of bone on beta dose distributions in radiation synovectomy. It has been defined as radiation scattered by bone back into the soft tissue from which it originated. For the joint model used here, it was found that the backscatter contribution to absorbed dose in nearby synovium is negligible. The 1 mm thick layer of articular cartilage at the bone surface was seen to absorb all backscattered radiation and, hence, prevent absorbed dose enhancement in synovium.

For 2 of the 8 radionuclides investigated however, minor absorbed dose enhance-

Table 4.5: Effect of advancing rheumatoid arthritis on absorbed dose deposition in radiation synovectomy.

Stage	Bone surface dose	Synovial dose at 2 mm	Synovial dose at 4 mm
1	17 Gy	6.7	0.47
2	16	6.9	0.51
3	15	7.1	0.55

ment was seen in the region of articular cartilage. Since the bone surface is located 1 mm away from the plane source region, backscatter becomes a consideration in radiation synovectomy only when the mean beta energy of the injected radionuclide is sufficient to allow a reasonable number of energetic electrons to reach the bone surface. Of the 8 radionuclides investigated, only ^{32}P and ^{90}Y decay with beta-particle emission energies sufficiently high. In both instances the enhancement effect was seen to be small however, increasing the absorbed dose in the bins of articular cartilage nearest the bone surface by only 3-4%.

4.3.3 Dosimetry and progression of rheumatoid arthritis

Effects of advancing rheumatoid arthritis on the extent and pattern of absorbed dose distributions in treated joints were examined by running additional simulations using models developed to represent rheumatoid joints at varying stages of disease. Results are presented in Table 4.5 for 37 MBq ^{90}Y uniformly distributed along 250 cm^2 synovium. Absorbed dose to the bone surface, synovium at 2 mm, and synovium at 4 mm are shown at disease stages 1, 2, and 3.

As the volume of joint fluid and the number of lining cells increase with advancing rheumatoid arthritis, the dosimetry can be said to improve. Progressing from the stage 1 joint to stages 2 and 3, absorbed dose to the bone surface is seen to decrease 14%, while dose to the synovium at a depth of 2 mm increases 6.0%.

4.4 Discussion

Calculation of beta dosimetry in radiation synovectomy is a difficult problem due to the complex geometry of synovial joints. Nonetheless several different approaches have been applied. Husak *et al.* [9], for instance, applied the beta dose point kernel method [12] to calculate beta dose distributions for ^{90}Y and ^{198}Au. Recognizing the fact that radionuclides injected into the joint are absorbed by the synovial surface,

their approach was to approximate the treated joint as a thin plane sources of uniform activity in a homogeneous soft tissue volume (see Section 1.1.1). Results show the dependence of absorbed dose on distance (up to 0.6 mm) from ^{90}Y and ^{198}Au sources having a thickness of 20, 30, or 40 μm. They found that at distances greater than 0.1 mm, absorbed dose to tissue is independent of the plane source thickness used in the calculation.

In the present work, the calculations of beta dose at depth in tissue reported by Husak *et al.* were compared with the **EGS4** Monte Carlo estimates of beta dose distributions in synovial joints. For ^{198}Au, for instance, Husak *et al.* calculated that 37 MBq (1 mCi) uniformly distributed on a synovial surface area of 250 cm^2 delivers an absorbed dose at 0.15 mm of approximately 1800 cGy (1800 rad), integrated over all time. The corresponding value of absorbed dose estimated using the dose factors for ^{198}Au shown in Figure 4-17 is 1820 cGy. For 37 MBq (1 mCi) ^{90}Y on a surface area of 250 cm^2, they reported an absorbed dose to tissue at 0.15 mm of approximately 2500 cGy. Using the dose factors in Figure 4-11, an absorbed dose of 2620 cGy is determined in the present work. Differences in the estimates of absorbed dose for the two approaches are 1% for ^{198}Au and 5% for ^{90}Y. Additional comparisons with Husak *et al.* of absorbed dose at depth are not made since their curves do not continue beyond 0.6 mm.

Rekonen *et al.* [46] used a related analytical approach to calculate the beta-particle dosimetry of ^{90}Y in radiation synovectomy. The calculations show (1) absorbed dose for ^{90}Y either: *a*) absorbed by the synovial surface (plane source) or *b*) suspended in the joint capsule (volume source); and (2) variation of absorbed dose with depth in tissue. In this case, the calculation of absorbed dose at depth is for 220 MBq (6 mCi) ^{90}Y uniformly distributed on an infinitely thin plane having an area of 150 cm^2. A homogeneous soft tissue volume again was assumed. Based on their approach, the absorbed dose at 1.0 mm from the plane source was calculated to equal approximately 12,000 cGy; at 2.5 mm, approximately 5000 cGy. Using the dose factors in Figure 4-11, the Monte Carlo approach presented here estimates an absorbed dose of 10,400 cGy in the bin 0.9-1.1 mm from the source, and 3300 cGy in the bin 2.3-2.5 mm from the source. Differences in the results for the two approaches are 13% (at a depth of 1.0 mm) and 34% (at a depth of 2.5 mm).

A different analytical approach was used by Topp *et al.* [3]. Their results, generated using the decay scheme of ^{198}Au, show the dependence of absorbed dose to synovium on both the amount of activity injected and the volume of fluid in the joint capsule. For a 25 cm^3 fluid volume, 300 MBq (8 mCi) ^{198}Au was reported to deliver 40,000 cGy to the synovial surface and 5720 cGy at a depth of 1 mm. For a 50 cm^3 fluid volume, the same administered activity was reported to deliver 20,000 cGy to the surface and 2860 cGy at 1 mm. When comparing these results to those obtained using Monte Carlo however, it is unclear as to how injected activity and fluid vol-

ume are best related to an areal concentration of activity. If it is assumed that the 300 MBq ^{198}Au is uniformly distributed throughout the joint capsule and lining cells regions (total thickness of 0.074 cm), then a 25 cm^3 fluid volume corresponds to a synovial surface area of 340 cm^2. The resulting doses estimated using the dose factors presented here are 10,700 cGy to the synovial surface and 2550 cGy at a depth of 1 mm. Differences in the results for the two approaches, in this case, are 73% (at the surface) and 55% (at a depth of 1 mm).

It is worth noting that the approach taken by Topp *et al.* has not accounted for either: (1) aspiration of joint fluid from the capsule before injection or (2) uptake of radioactivity by the lining cells after injection. Of the 3 analytical approaches discussed, that of Husak *et al.*, who have taken both these considerations into account and used beta dose point kernels to evaluate the dosimetry in radiation synovectomy, is believed to be the most accurate. However, their approach required approximating the joint as a homogeneous soft tissue volume. As a result, Husak *et al.* have not considered the radiation dose imparted to other, healthy, joint components located nearby, such as bone. Dose to bone is addressed next.

4.4.1 Backscatter calculations and absorbed dose to bone

A thin layer of articular cartilage completely lines the ends of articulating bony surfaces in all synovial joints. Although the thicknesses are not well documented, they can be expected to vary from 0.5 to 2-3 mm depending on the size of the joint [17, 18]. With the simulations reported here, a layer of articular cartilage only 1 mm thick was seen to be sufficient to prevent radiation backscattered off bone from reaching synovium. For ^{32}P and ^{90}Y however, minor absorbed dose enhancement was seen in the region of articular cartilage. Clinically, the enhancement is small enough that the potential for radiation damage in articular cartilage is not significantly *increased* by backscatter.

It is worth noting that articular cartilage has an elemental composition and density which closely resembles that of soft tissue and water (see Table 4.1). The presence of articular cartilage in synovial joints therefore acts to reduce the effects of tissue inhomogeneities on beta dosimetry in radiation synovectomy. In fact, for the low-energy beta emitters of interest in radiation synovectomy, the joint model developed for this work is essentially homogeneous. Agreement with the point kernel based calculations of absorbed dose at depth in a homogeneous soft tissue volume reported by Husak *et al.* substantiates this observation.

However, approximating the joint as a homogeneous soft tissue volume does not allow one to estimate the absorbed dose imparted to bone during radiation synovectomy. Absorbed dose to the bone surface (10 μm) is particularly of interest since the International Commission on Radiation Protection has identified this tissue region

Table 4.6: Bone surface (μm) beta dose expressed as a percentage of the beta dose imparted to the lining cells.

Radionuclide	Bone surface dose
^{32}P	16%
^{90}Y	25
^{153}Sm	< 0.01
^{165}Dy	0.7
^{166}Ho	15
^{186}Re	3.8
^{188}Re	19
^{198}Au	2.5

as one of two principal radiosensitive targets to be protected in procedures involving bone irradiation [13].

Referring to Figures 4-10 through 4-17, absorbed dose to bone is seen to be largely dependent on the injected radionuclide's mean beta energy, or penetration ability. Expressed as a percentage of the beta dose imparted to the lining cells, beta dose to the bone surface is seen in Table 4.6 to vary from 25% of the lining cells dose for ^{90}Y down to less than 0.01% for ^{153}Sm. The author knows of no previous attempt to evaluate the absorbed dose to non-target tissues in radiation synovectomy.

4.4.2 Dosimetry and rheumatoid arthritis progression

As with other therapies, clinical success in radiation synovectomy is known to depend largely on the extent of disease progression in the joint prior to treatment, with success becoming much less likely in joints with advanced symptoms of rheumatoid arthritis. Among other things, advanced rheumatoid arthritis is characterized by increased joint fluid volumes and increased numbers of lining cells. Combined, these two characteristics have the effect of extending the thickness of the radioactive source region. To determine whether the extended source could result in reduced likelihood for success in radiation synovectomy with advancing rheumatoid arthritis, additional simulations were made using **EGS4** and incorporating slight alterations in the joint model.

Reduced likelihood for success was found to be unrelated to the extended source, however, since the resulting beta dose distributions actually improved [10]. Dose to synovium increased with advancing rheumatoid arthritis, while dose to the bone surface decreased. The improvement is attributed to that fact that increased numbers

Table 4.7: Therapeutic and maximum ranges of the 8 radionuclides investigated.

Radionuclide	Therapeutic range	Maximum range
^{32}P	2.2 mm	7.9
^{90}Y	2.8	10.8
^{153}Sm	0.7	3.1
^{165}Dy	1.3	5.6
^{166}Ho	2.1	8.7
^{186}Re	1.0	4.5
^{188}Re	2.1	10.1
^{198}Au	0.9	3.9

of lining cells have the effect of absorbing more of the injected activity deeper into the synovium, and thus away from bone. The reduced likelihood for clinical success in joints with advanced symptoms of rheumatoid arthritis thus must be due to some other factor.

4.4.3 Therapeutic range

The dose factors presented here are intended to provide the information necessary for those interested in radionuclide selection, dose prescription, and resulting beta dose distributions in radiation synovectomy. Radionuclide selection, for instance, is based, at least in part, on an evaluation of the absorbed dose penetration of each of the radionuclides under consideration. In particular, one wants to ensure that the deepest limit of the target volume lies within a radionuclide's *therapeutic range* and that other, healthy, joint components located nearby are not subjected to an unnecessary radiation hazard. The therapeutic range is defined here as the synovial depth at which the percentage dose is equal to 10% of the maximum synovial dose, deposited at the synovial surface. While not a useful value for dosimetry purposes, the therapeutic range is an important parameter in radiation therapy.

Table 4.7 lists therapeutic and maximum ranges of the 8 radionuclides investigated here. In each case, the therapeutic range is seen to be much shorter than the corresponding maximum range. In addition, the 8 therapeutic ranges are seen to demonstrate considerably less variation between radionuclides than the 8 maximum ranges. Since it is the therapeutic range which determines the thickness of synovium that can be treated and not the maximum range, treatment volume variations between radionuclides are not large.

4.5 Conclusion

Beta-particle dosimetry of various radionuclides used in the treatment of rheumatoid arthritis was estimated using Monte Carlo radiation transport simulation. Absorbed dose factors (cGy-cm^2/MBq-s) were determined as a function of distance in a mathematical model of the rheumatoid joint, with dimensions in the model selected to correspond with those typically found in larger synovial joints, *e.g.*, the knee, shoulder, or hip. The presence of bone in the model was investigated to determine whether radiation backscatter enhances absorbed dose to synovium in radiation synovectomy. It was found that the layer of articular cartilage separating bone from synovium is sufficiently thick to prevent backscattered radiation from reaching the tissue. For 2 of the 8 radionuclides investigated however, minor absorbed dose enhancement (3-4%) was seen in the bins of articular cartilage closest to bone.

The absorbed dose factors presented here are intended to provide guidance for clinicians concerned with radionuclide selection and the amount of activity to administer in radiation synovectomy. Definite data on the absorbed dose required at depth in synovium for successful therapy have not been established. For a given areal concentration of injected radioactivity uniformly distributed throughout the joint capsule and along a surface layer of lining cells, however, absorbed dose to tissue (synovium), articular cartilage, and bone are easily estimated with the results shown in Figures 4-10 through 4-17.

The absorbed dose factors also provide information, previously unavailable, regarding the potential for radiation damage in other, healthy, parts of the joint, such as bone. Radiation damage to the bone surface (10 μm) is particularly of interest since this tissue volume has been identified as a radiosensitive target to be protected in procedures involving bone irradiation [13]. For the radionuclides investigated here, absorbed dose to bone was seen to vary from 25% of the synovial surface (or lining cells) dose for ^{90}Y down to 5% for ^{198}Au. Clinicians interested in radiation synovectomy therefore will want to ensure that a therapeutic radiation dose can be delivered to target synovium without subjecting other joint components to an unacceptable or unnecessary radiation hazard.

In the next Chapter, experimental beta dosimetry in radiation synovectomy is presented. In the experiments, reactor-produced radionuclides and radiachromic film dosimeters were used to measure absorbed dose distributions in both joint phantoms and the knees of fresh, human cadavers. The results are compared with the Monte Carlo estimates of beta dose distributions in treated joints discussed here.

Chapter 5

Experimental Beta Dosimetry

5.1 Introduction

In general, there are three methods for estimating absorbed dose distributions in radiation synovectomy or any other radiation therapy. These include: (1) direct measurement in humans, (2) extrapolation from measured data in animals, phantoms, and cadavers, and (3) calculations based on mathematical models.

In humans, the direct measurement of beta dose distributions in radiation synovectomy is possible but it presents severe difficulties. For instance, many of the radiation dosimeters commonly used today simply are too large to be inserted into human joints. And dosimeters which may be small enough for insertion present problems associated with their implantation, accurate positioning, and retrieval. For the purposes of dosimetry alone, the resulting inconvenience and discomfort to patients generally is considered to be excessive.

Since direct measurements in humans are so difficult to obtain, estimates of beta dose distributions in radiation synovectomy have come to rely on calculation instead of measurement. For example, Monte Carlo estimates of beta dosimetry in radiation synovectomy were presented in Chapter 4. The estimates were obtained using Monte Carlo radiation transport simulation to evaluate the extent and pattern of absorbed dose deposition in a mathematical model of the treated joint. In all, the beta dosimetry of 8 radionuclides was presented.

The purpose of this chapter is to present a series of experiments aimed at measuring beta dose distributions in joint phantoms and the knees of fresh, human cadavers. Radiachromic film dosimeters and 2 reactor-produced radionuclides, ^{165}Dy and ^{166}Ho, were used in the experiments.

The chapter begins with a discussion of the phantom experiments. Included are descriptions of the radiation dosimeters used to measure absorbed dose, the tissue substitutes used to build the phantoms, and the procedures used to prepare the

radioactive sources. Then the chapter continues with a discussion of the experiments conducted in the knees of cadavers. Results are presented and discussed for both sets of experiments.

5.2 Experiments in Phantoms

A phantom can be defined as a volume of tissue substitutes used to reproduce radiation absorption and scattering characteristics in order to measure dosimetric quantities at various locations. Tissue substitutes, in general, are intended to simulate either the body or a portion of the body with respect to: size, shape, position, mass density, and radiation interaction probabilities. For a given radiation type and energy, substitutes should absorb and scatter incident radiation to the same extent, within acceptable limits, as the irradiated tissues do.

In this section, use of synovial joint phantoms to measure depth-dose data that can be used to extrapolate predictions of beta dose distributions in radiation synovectomy is described. Results are compared with the dose estimates generated using Monte Carlo radiation transport simulation in a mathematical model of the joint (see Chapter 4).

5.2.1 Materials and methods

Tissue substitutes

When selecting a tissue substitute, ideally, one wants to choose a material which has radiation absorption and scattering properties which are the same as those of the relevant tissue. In practice, one tries to get as close to a match as possible.

In beta dosimetry, it is the mass scattering power T/ρ and the mass stopping powers for collisions S_{col}/ρ and bremsstrahlung production S_{rad}/ρ which should be similar over the energy interval of interest. The linear scattering power T of a material expresses the increase in the mean square angle of scattering for a given pathlength in the material, whereas the linear stopping power S expresses the energy lost by an electron in travelling a given pathlength in the material. For energies at which nuclear interactions can be neglected, the total linear stopping power S can be separated into two components:

$$S = S_{col} + S_{rad}. \tag{5.1}$$

The collision stopping power S_{col} includes all energy losses in collisions which directly produce knock-on electrons and atomic excitations. The radiative stopping power S_{rad} includes all energy losses of the primary electron which lead to the production of bremsstrahlung photons.

Table 5.1: Electron mass stopping powers (MeV-m^2/kg) and mass scattering powers (Radian^2-m^2/kg) for BONE. Adopted from *ICRU-44*.

Energy (MeV)	$(S/\rho)_{col}$	$(S/\rho)_{rad}$	S/ρ	T/ρ
0.020	1.14E+00	5.90E−04	1.14E+00	2.68E+02
0.040	6.76E−01	6.09E−04	6.77E−01	8.04E+01
0.060	5.06E−01	6.20E−04	5.06E−01	4.00E+01
0.080	4.16E−01	6.33E−04	4.17E−01	2.45E+01
0.200	2.46E−01	7.26E−04	2.47E−01	5.42E+00
0.400	1.90E−01	9.43E−04	1.91E−01	1.85E+00
0.600	1.73E−01	1.21E−03	1.74E−01	1.00E+00
0.800	1.66E−01	1.52E−03	1.68E−01	6.53E−01
1.000	1.63E−01	1.85E−03	1.65E−01	4.68E−01
2.000	1.62E−01	3.81E−03	1.66E−01	1.62E−01
3.000	1.64E−01	6.07E−03	1.70E−01	8.50E−02

Tissue substitutes selected for use in the joint phantom included aluminum and solid water (a specially formulated, commercially available plastic). The aluminum served as a substitute for bone, and the solid water served as a substitute for articular cartilage and soft tissue (synovium). Electron mass scattering and stopping power data for the three tissues—bone, articular cartilage, and soft tissue—and their two substitutes—aluminum and solid water—are shown in Tables 5.1 through 5.5 over the energy interval of interest [81].

Solid water. Solid water is an epoxy resin-based material specially formulated to have electron and photon absorption and scattering characteristics very close to those of water. Its material composition, elemental composition, and specific gravity are listed in Table 5.6 [84].

Use of water substitutes as soft tissue substitutes for the purposes of dosimetry in radiation therapy is not expected to introduce uncertainties in the absorbed dose estimates greater than 1%. Using a homogeneous, cubic, solid water phantom (30 cm × 30 cm × 30 cm) and a ^{60}Co source, Constantinou *et al.* measured depth-dose data within ±1% of that derived for a standard water phantom [85]. Solid water also has been shown to be superior to other commonly used water substitutes, *e.g.*, Lucite and polystyrene [84].

A single sheet of solid water (30 cm × 30 cm × 1 mm) was purchased from

Table 5.2: Electron mass stopping powers (MeV-m^2/kg) and mass scattering powers (Radian^2-m^2/kg) for ARTICULAR CARTILAGE. Adopted from *ICRU-44*.

Energy (MeV)	$(S/\rho)_{col}$	$(S/\rho)_{rad}$	S/ρ	T/ρ
0.020	1.29E+00	4.01E−04	1.29E+00	2.06E+02
0.040	7.61E−01	4.07E−04	7.62E−01	6.15E+01
0.060	5.68E−01	4.12E−04	5.68E−01	3.05E+01
0.080	4.66E−01	4.20E−04	4.66E−01	1.86E+01
0.200	2.74E−01	4.86E−04	2.74E−01	4.08E+00
0.400	2.11E−01	6.42E−04	2.11E−01	1.38E+00
0.600	1.92E−01	8.36E−04	1.93E−01	7.50E−01
0.800	1.85E−01	1.06E−03	1.86E−01	4.87E−01
1.000	1.81E−01	1.30E−03	1.82E−01	3.49E−01
2.000	1.79E−01	2.71E−03	1.81E−01	1.20E−01
3.000	1.81E−01	4.35E−03	1.85E−01	6.30E−02

Table 5.3: Electron mass stopping powers (MeV-m^2/kg) and mass scattering powers (Radian^2-m^2/kg) for SOFT TISSUE. Adopted from *ICRU-44*.

Energy (MeV)	$(S/\rho)_{col}$	$(S/\rho)_{rad}$	S/ρ	T/ρ
0.020	1.32E+00	3.94E−04	1.32E+00	2.05E+02
0.040	7.77E−01	3.99E−04	7.78E−01	6.09E+01
0.060	5.79E−01	4.04E−04	5.80E−01	3.02E+01
0.080	4.76E−01	4.12E−04	4.76E−01	1.84E+01
0.200	2.79E−01	4.77E−04	2.80E−01	4.04E+00
0.400	2.15E−01	6.31E−04	2.15E−01	1.37E+00
0.600	1.96E−01	8.22E−04	1.97E−01	7.42E−01
0.800	1.89E−01	1.04E−03	1.90E−01	4.82E−01
1.000	1.85E−01	1.28E−03	1.86E−01	3.45E−01
2.000	1.82E−01	2.67E−03	1.85E−01	1.19E−01
3.000	1.85E−01	4.29E−03	1.89E−01	6.23E−02

Table 5.4: Electron mass stopping powers (MeV-m^2/kg) and mass scattering powers (Radian^2-m^2/kg) for ALUMINUM. Adopted from *ICRU-44*.

Energy (MeV)	$(S/\rho)_{col}$	$(S/\rho)_{rad}$	S/ρ	T/ρ
0.020	9.84E−01	6.92E−04	9.85E−01	3.01E+02
0.040	5.91E−01	7.08E−04	5.92E−01	9.06E+01
0.060	4.44E−01	7.17E−04	4.45E−01	4.51E+01
0.080	3.66E−01	7.29E−04	3.67E−01	2.77E+01
0.200	2.17E−01	8.32E−04	2.18E−01	6.12E+00
0.400	1.68E−01	1.08E−03	1.69E−01	2.09E+00
0.600	1.54E−01	1.38E−03	1.55E−01	1.13E+00
0.800	1.49E−01	1.73E−03	1.50E−01	7.39E−01
1.000	1.47E−01	2.11E−03	1.49E−01	5.29E−01
2.000	1.48E−01	4.33E−03	1.52E−01	1.84E−01
3.000	1.51E−01	6.89E−03	1.58E−01	9.63E−02

Table 5.5: Electron mass stopping powers (MeV-m^2/kg) and mass scattering powers (Radian^2-m^2/kg) for SOLID WATER. Adopted from Constantinou *et al.*

Energy (MeV)	S/ρ	T/ρ
0.01	2.19E+00	6.03E+02
0.10	4.00E−01	1.11E+01
1.00	1.11E−01	3.04E−01

Table 5.6: Composition of solid water. Adopted from Constantinou *et al.*

	Percentage by weight
Components	epoxy CB4 (80.48%), polyethylene (10.00), calcium carbonate (5.77), phenolic microspheres (3.75)
Elements	H (8.09), C (67.22), N (2.40), O (19.84), Ca (2.32), Cl (0.13)
Specific gravity	1.015 ± 0.002

Radiation Research, Inc. for use in the joint phantom. The sheet was cut into 25 smaller slabs (each 6 cm × 6 cm × 1 mm), and these were used in the phantom as articular cartilage and soft tissue substitutes.

Articular cartilage, it should be noted, is a body tissue similar in composition to soft tissue, as shown in Table 4.1. It, too, is composed primarily of water (60-80% H_2O), and as a result its radiation absorption and scattering characteristics are well simulated with water substitutes such as solid water.

Aluminum. Aluminum is a rigid metallic solid which is easily machined into a variety of shapes. It is commonly used as a good substitute for bone in experimental radiation dosimetry [86, 87]. Several slabs of aluminum (each 10 cm × 10 cm × 1 mm) were purchased for use as bone substitutes in the phantom.

Joint phantom

The assembled joint phantom is illustrated in Figure 5-1. On one side of the radioactive source (described below), several 1 mm thick slabs of aluminum were stacked together and served as a substitute for bone. A single slab of solid water (1 mm thick) positioned between the aluminum slabs and the radioactive source served as an articular cartilage substitute, to mimic the thin layer of articular cartilage that caps the ends of the bones in all synovial joints. On the other side of the radioactive source, several 1 mm thick solid water slabs were stacked together and served as a substitute for soft tissue (synovium). In the phantom, distances are defined in relation to the leftmost solid water-radioactive source interface, as indicated in Figure 5-1.

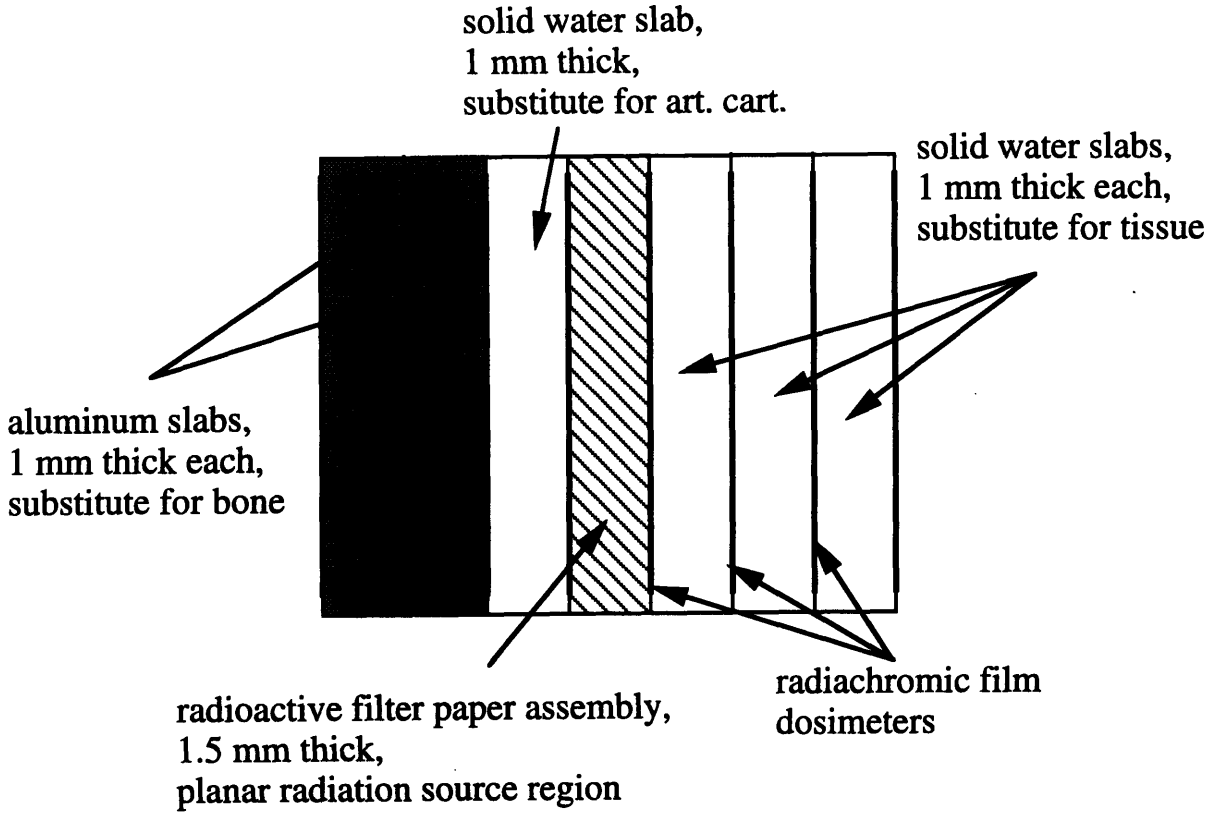

Figure 5-1: Phantom used to experimentally measure radiation absorbed dose penetration in synovial joints treated with radiation synovectomy. Distances are defined in relation to the leftmost solid water-radioactive source interface.

Radioactive source preparation

The phantom's radioactive source region is intended to mimic that of the treated joint. As mentioned in Chapters 2 and 4, rheumatoid joints to be treated with radiation synovectomy generally are aspirated of all fluid [17]. Radioactivity, held in a liquid suspension, then is injected into the joint capsule where it makes direct contact with inflamed synovium [1]. Phagocytic lining cells along the synovial surface quickly absorb radioactive particulate from the capsule. Autoradiographs of the tissue lining in knees injected with various radionuclides have shown a reasonably even distribution of radioactivity in these cells for several days after injection [2, 3, 4]. The ends of the articulating bony surfaces, capped with articular cartilage, do not absorb radioactive particulate however since the cells along these surfaces are not phagocytic [46]. The radioactive source region in treated joints thus can be described as including the fluid-filled joint capsule and the synovial lining cells. In the phantom experiments, planar radioactive sources of ^{165}Dy and ^{166}Ho were prepared to mimic this region.

^{165}Dy. Two planar sources of ^{165}Dy with initial radioactivity of the order 9000 MBq were prepared by dipping ten thin squares of cellulose filter paper, each 7.5 mg/cm^2 thick and 6×6 cm^2 in area, once each in a solution containing 1.75 mg Dy_2O_3 (stable, natural Dy) dissolved in 5.0 ml nitric acid (3% HNO_3). The soaked papers were dried in air by hanging them vertically but rotating each a few times in the vertical plane while still wet. The object of the change in the rotational position was to achieve greater uniformity in the distribution of dysprosium on the papers. Ten filter papers, each 7.5 mg/cm^2 thick, were used so that the density thickness of the phantom's source would approximates of treated joints. The density of cellulose is 0.5 g/cm^3.

When the papers had dried, they were stacked and stitched together at the four corners using a needle and thread. The dried filter paper assembly then was irradiated at the MIT Nuclear Reactor Laboratory (Cambridge, MA) for 54 min at full power (thermal neutron flux $\approx 7.5 \times 10^{12}$ neutrons/cm^2-s). Activation of stable ^{164}Dy on the papers resulted in the production of $\approx 8.6 \times 10^3$ MBq ^{165}Dy. After allowing 80 minutes decay time for radiation protection purposes, the filter paper assembly was inserted into the joint phantom. At the time of insertion, the activity of ^{165}Dy in the assembly was roughly equivalent to 5.0×10^3 MBq. This activity was allowed at least 10 half-lives to decay. ^{165}Dy has a 2.3 h half-life.

^{166}Ho. A planar source of ^{166}Ho with initial radioactivity of 250 MBq was prepared following the procedures described above for ^{165}Dy, with the following exceptions. One mg Ho_2O_3 (stable, natural Ho) was dissolved in 5.0 ml nitric acid (3% HNO_3), and the solution was used to soak the filter papers. In addition, the irradiation time was 6 h, instead of 54 min.

Activation of stable ^{165}Ho on the papers resulted in the production of 250 MBq ^{166}Ho. After allowing 2 h decay time for radiation protection purposes, the 240 MBq ^{166}Ho remaining on the papers was inserted into the joint phantom. The activity was allowed at least 10 half-lives to decay. ^{166}Ho has a 27 h half-life.

Dosimeters

Many types of detectors are available for measuring absorbed dose. The detector response can be any radiation-induced change in its physical, chemical, or biological properties, provided that the change can be quantified and is uniquely related to the radiation dose. Some of the more commonly used detectors include various gas ionization devices, thermoluminescence dosimeters (TLDs), film emulsions, liquid scintillators, chemical (Fricke) dosimeters, and solid-state diodes.

When choosing a detector for use in radiation dosimetry, important considerations to bear in mind include its size and elemental composition. Size is important in that the detector must be small enough to minimize perturbations in the particle fluence but large enough to undergo a sufficient number of interactions to yield a signal that can be read with precision. Elemental composition is important in that the detector's composition should be as similar as possible to that of the surrounding materials, again to minimize perturbations in the particle fluence.

The dosimeters used in this work were GafChromic DM1260 radiachromic film dosimeters purchased from Far West Technology, Inc. (Goleta, CA). The film is a thin, laminated-plastic material having radiation absorption properties similar to those of soft tissue. It consists of a very thin ($\approx$ 7 μm) radiachromic sensor coating (a proprietary substance) on a polyester film base ($\approx$ 100 μm). When exposed to ultraviolet or ionizing radiation with energy greater than 4 eV, the coating undergoes a radiation-induced color change by photoionization. The change, from colorless to deep blue, occurs gradually as a function of absorbed dose.

The photochemical reaction involved is a unimolecular decomposition of any one of a variety of aminotriphenyl methane dye derivatives. The decomposition is followed by an intramolecular electron rearrangement to form the stable and deeply colored corresponding dye [88, 89]. No processing is required to bring about this color change.

Some important dosimetric characteristics of the films include: a linear response to ionizing radiation over a wide range of doses; dose-rate independence; energy independence of response down to a few keV; an equivalent response to electrons and photons; low atomic number composition (primarily H, C, N, O); and the fact that the radiation-induced image is quite stable [90].

A major advantage of the radiachromic film dosimetry system is the straightforward manner in which the radiation response is analyzed. A reader designed specifically for standard radiachromic film dosimetry is a simple photometer, as shown in

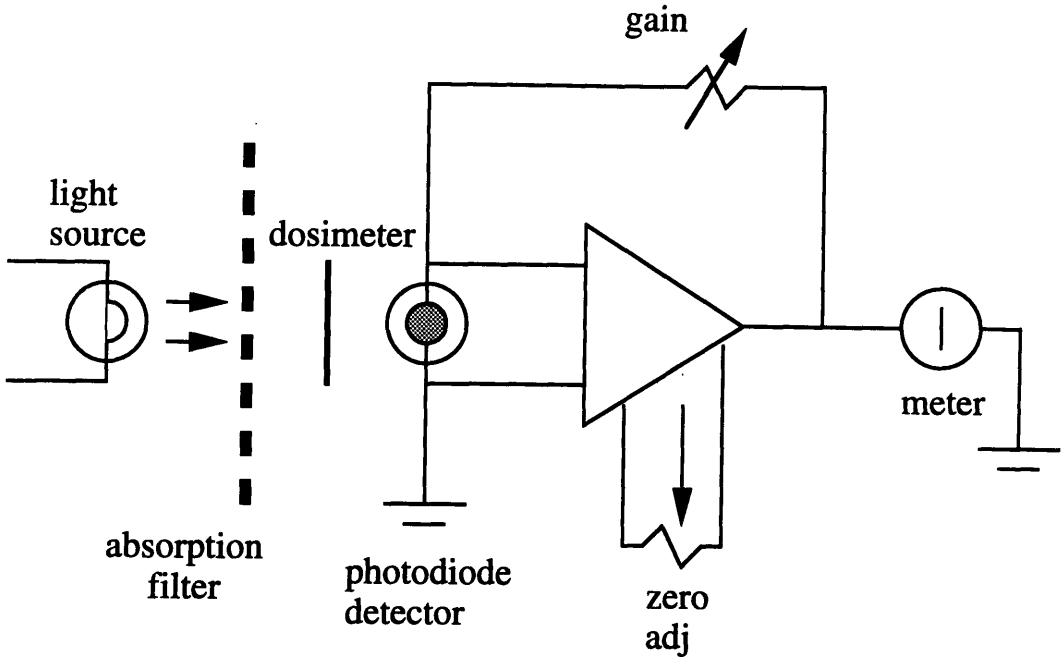

Figure 5-2: Block diagram of a simple radiachromic film dosimeter reader.

Figure 5-2. Light, filtered to the film's peak absorption wavelength, is transmitted through the dosimeter where it is received by a silicon photodiode and converted into an electrical signal. The signal is fed into a high input impedence operational amplifier, and the output is displayed on a meter as optical density OD. Optical density is related to transmission according to the following relation:

$$OD = \log \frac{T_0}{T} \tag{5.2}$$

where T_0 is 100% transmission and T is transmission after coloration. A calibration curve depicting the change in optical density ΔOD as a function of absorbed dose D is used to quantify the dose imparted to the dosimeters.

Portions of a 12.7 cm wide roll of GafChromic film were cut into 6 cm × 6 cm squares for insertion into the joint phantom. The size of the film squares is large enough so that four 1 cm × 1 cm samples cut from the center are separated from any edges by at least 1.5 times the range of the most energetic beta-particle emitted, a distance which is sufficiently large to prevent boundary, or edge, effects in the

measurements.

The cut film squares were sandwiched between the slabs of aluminum and solid water, as shown in Figure 5-1. Upon the insertion of a radioactive source, the films were used to measure the absorbed dose deposited at several depths in the phantom. Depths, or distances, in the phantom were defined in relation to the leftmost solid water-radioactive source interface, which is intended to represent the articular cartilage surface abutting the joint capsule.

Calibration. The calibration curve for the GafChromic film used in these experiments is shown in Figure 5-3. The curve was generated by first irradiating samples of the film with known radiation doses, then measuring the change in OD and plotting the results. The irradiations were conducted under controlled conditions using gamma radiation from a calibrated ^{60}Co source at the National Institute of Standards and Technology (Bethesda, MD). Samples of the film were sealed inside polymer-aluminum laminate packets, held between two 5.0 mm thick blocks of polystyrene, and exposed to 100, 200, 400, 700, or 1000 Gy. Estimates of uncertainty in the delivered doses are less than 3%.

The change in optical density then was measured for each of the irradiated dosimeters and used to calculate a calibration curve for the film. The calibration curve relating the absorbed dose D (Gy) to a measured change in optical density ΔOD is as follows:

$$D = 10.2(\Delta OD)^3 + 27.31(\Delta OD)^2 + 289.7\Delta OD. \quad (5.3)$$

All absorbed dose measurements in this work were obtained with a readout wavelength of 600 nm.

Analysis

After each of the radioactive sources was allowed 10 half-lives to decay, the joint phantoms were disassembled and the radiachromic film dosimeters were retrieved for analysis. Four 1 cm × 1 cm samples were cut from the center of each dosimeter. For each sample, the change in optical density ΔOD was measured and converted to an absorbed dose D using the calibration curve described above (see Eqn. 5.3).

5.2.2 Results

The phantom experiments were completed twice with ^{165}Dy sources and once with an ^{166}Ho source. The results are as follows.

^{165}Dy. Results of the two ^{165}Dy phantom experiments are shown in Table 5.7 as absorbed dose factors F_i (cGy-cm^2/MBq-s) at depth in the phantom. In each of the

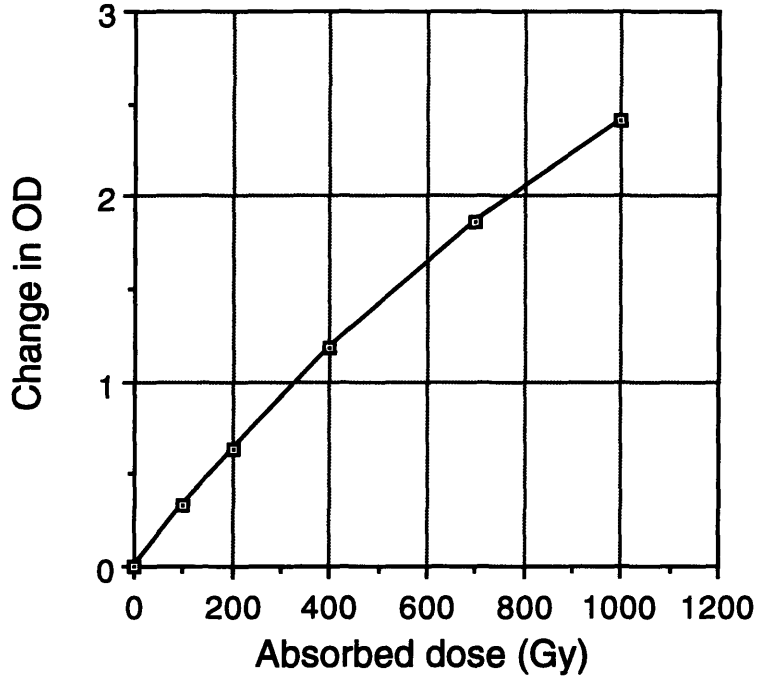

Figure 5-3: Calibration curve for the radiachromic film dosimeters used in these experiments.

experiments, the absorbed dose was measured at 5 different depths, or positions: -1.0 mm, 0.0 mm, 0.74 mm, 1.74 mm, 2.74 mm. Four absorbed dose measurements were obtained at each position, and the average dose was converted to an absorbed dose factor according to the following relation:

$$F_i = \frac{D_i \lambda S_{source}}{A}, \tag{5.4}$$

where F_i is the absorbed dose factor (cGy-cm^2/MBq-s), D_i is the absorbed dose (Gy), λ is the radionuclide's decay constant (s^{-1}), S_{source} is the surface area of the radioactive filter paper assembly (36 cm^2), and A is the amount of radioactivity (MBq) inserted into the phantom. In each of the two experiments, variations in measured doses at each of the 5 positions were seen to be small, typically less than 5%. The small variations were attributed to the high precision of the radiachromic film dosimeters and the ease with which planar ^{165}Dy sources of uniform activity can be made. The error associated with each of the factors shown in Table 5.7, however, is seen to be 15%. The increased errors associated with the factors are due to uncertainties in accurately knowing the amount of radioactivity A inserted into the phantom (see Section 5.2.3).

It is worth noting that dosimeters were not placed at the phantom position corresponding to the synovial surface in treated joints. This is a position which is located *inside* the radioactive source region. Including dosimeters there would have required dividing the source into 2 smaller regions and preparing each of the 2 halves individually. Upon assembling the phantom, a square of radiachromic film then could have been sandwiched between the 2 radioactive source halves and the entire source-film-source assembly inserted into the phantom. For radiation protection purposes, however, it was decided that the source handling time should be as short as possible, and the source was prepared as a single assembly.

In Figure 5-4, results of the two experiments are combined and compared with the Monte Carlo calculations of absorbed dose factors versus depth in the mathematical joint model.

^{166}Ho. Results of the ^{166}Ho phantom experiment are shown in Table 5.8 as absorbed dose factors F_i (cGy-cm^2/MBq-s) at depth in the phantom. In this case, absorbed dose was measured at 6 depths, or positions, in the phantom: -1.0 mm, 0.0 mm, 0.74 mm, 1.74 mm, 2.74 mm, and 3.74 mm. Four absorbed dose measurements were obtained at each position, and, again, the average dose was converted to an absorbed dose factor using Eqn. 5.4.

As in the ^{165}Dy experiments, variations in the measured doses at each of the 6 positions were seen to be small, on the order of 5%. The errors associated with the absorbed dose factors reported in Table 5.8 are seen to be much larger, however. Due

Table 5.7: Results of the depth-dose measurements for ^{165}Dy obtained using the joint phantom. The results are expressed as absorbed dose factors (cGy-cm^2/MBq-s) at depth in the phantom.

Phantom position	Factor trial 1	Factor trial 2
−1.0 mm, bone surface	$5.1 \times 10^{-3} \pm 15\%$	$4.4 \times 10^{-3} \pm 15\%$
0.0 mm, art cart surface	$3.9 \times 10^{-2} \pm 15\%$	$2.8 \times 10^{-2} \pm 15\%$
0.74 mm, synovium at 0.3 mm	$4.1 \times 10^{-2} \pm 15\%$	$2.8 \times 10^{-2} \pm 15\%$
1.74 mm, synovium at 1.3 mm	$4.8 \times 10^{-3} \pm 15\%$	$4.4 \times 10^{-3} \pm 15\%$
2.74 mm, synovium at 2.3 mm	$8.4 \times 10^{-4} \pm 15\%$	$8.2 \times 10^{-4} \pm 15\%$

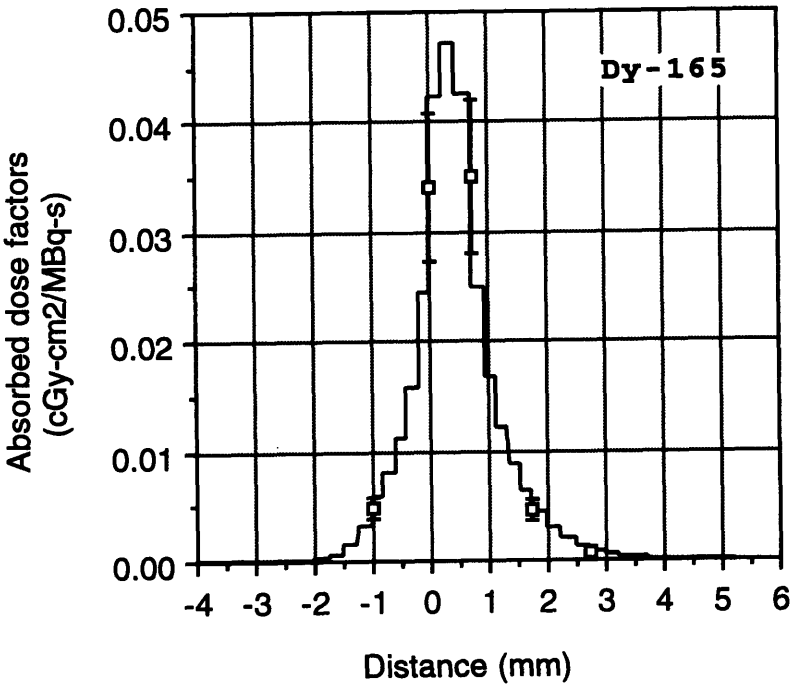

Figure 5-4: Comparison of the absorbed dose factors derived from measurements obtained using planar ^{165}Dy radioactive sources in the joint phantom with those obtained using Monte Carlo radiation transport simulation in a mathematical model of the joint.

Table 5.8: Results of the depth-dose measurements for ^{166}Ho obtained using the joint phantom. The results are expressed as absorbed dose factors (cGy-cm^2/MBq-s) at depth in the phantom.

Phantom position	Factor
−1.0 mm, bone surface	$7.1 \times 10^{-3} \pm 15\%$
0.0 mm, art cart surface	$3.3 \times 10^{-2} \pm 15\%$
0.74 mm, synovium at 0.3 mm	$3.9 \times 10^{-2} \pm 15\%$
1.74 mm, synovium at 1.3 mm	$8.3 \times 10^{-3} \pm 15\%$
2.74 mm, synovium at 2.3 mm	$3.2 \times 10^{-3} \pm 15\%$
3.74 mm, synovium at 3.3 mm	$1.1 \times 10^{-3} \pm 15\%$

to the uncertainty in accurately knowing the amount of ^{166}Ho radioactivity A inserted into the phantom, the errors associated with the factors were estimated to be 15%.

In Figure 5-5, results of the phantom experiments are compared with the Monte Carlo calculations of absorbed dose factors versus depth in the mathematical joint model.

5.2.3 Discussion

The measured phantom data presented above can be used to extrapolate radiation dose distributions in treated joints. For example, to estimate the beta dose D_i (cGy) imparted to the bone surface or to the synovium at a depth of 0.3 mm, one multiplies the appropriate absorbed dose factor F_i (cGy-cm^2/MBq-s) by the amount of injected activity A_0 (MBq) and divides the product by an estimate of the joint's total synovial surface area S_{syn} (cm^2) and the injected radionuclide's decay constant λ (s^{-1}), so that:

$$D_i = \frac{F_i A_0}{S_{syn} \lambda}. \tag{5.5}$$

Consider the injection of 10,000 MBq (270 mCi) ^{165}Dy into the knee. From Table 5.7, the average absorbed dose factor for the bone surface is 4.74×10^{-3} cGy-cm^2/MBq-s, and for the synovium at a depth of 0.3 mm it is 3.5×10^{-2} cGy-cm^2/MBq-s. Assuming uniform distribution of injected radioactivity, a total synovial surface area of 250 cm^2 (typical in the rheumatoid knee [17, 9]), and no leakage, the calculated absorbed dose to the bone surface is 2200±15% cGy; to the synovium at a depth of 0.3 mm, it is 17,000±15% cGy.

As mentioned above, the principal source of uncertainty associated with the esti-

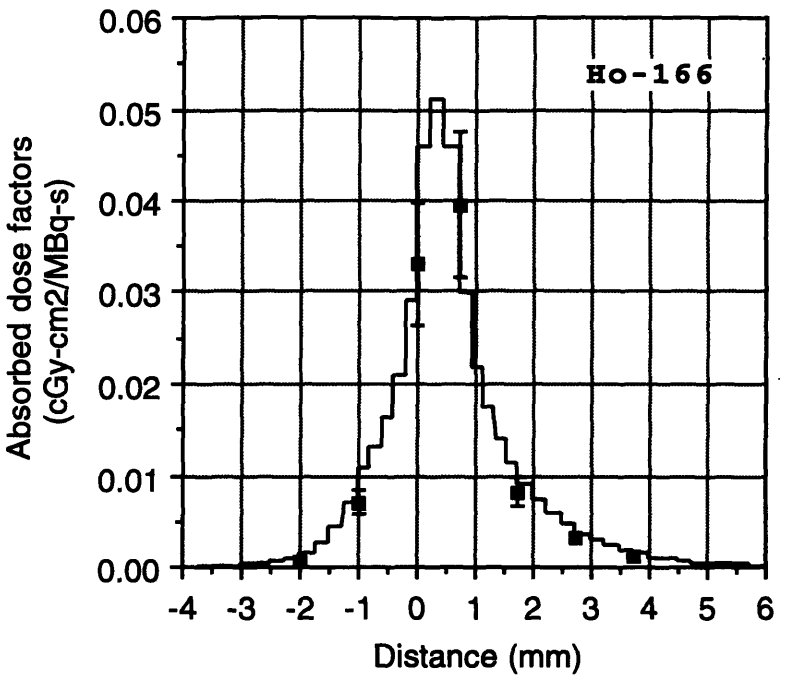

Figure 5-5: Comparison of the absorbed dose factors derived from measurements obtained using a planar ^{166}Ho radioactive source in the joint phantom with those obtained using Monte Carlo radiation transport simulation in a mathematical model of the joint.

mates is in accurately knowing the amount of radioactivity A inserted in the phantoms. When preparing the planar radioactive sources, uncertainties were introduced in accurately determining the number of target atoms dissolved in nitric acid, in ensuring that all the target atoms are dried onto the filter papers, and in accurately knowing the neutron flux used to activate the filter paper assembly (the flux certainly varies somewhat over the course of the irradiation). As a comparison, uncertainties associated with the absorbed dose measurements made using the radiachromic film dosimeters is on the order of 5%, or less.

Referring to Figures 5-4 and 5-5, results of both the ^{165}Dy and ^{166}Ho phantom experiments were seen to be in agreement with the corresponding Monte Carlo estimates of beta dose distributions in a mathematical model of the treated joint. Comparisons of the Monte Carlo estimates with experimental results are of interest since the EGS4 code originally was developed for high-energy transport and only recently was modified to extend its useful range to include lower energies. The agreement indicates that use of EGS4 to evaluate the dosimetry of low-energy electrons (< 2 MeV) in heterogeneous media is an acceptable application of the code. The agreement indicates more than this however. It also indicates that the results obtained here using Monte Carlo radiation transport simulation and experiments in joint phantoms with radiachromic film dosimeters and reactor-produced radionuclides are indeed accurate. This conclusion is an important one, as well, since the dosimetry of low energy beta-particles in heterogeneous media is a field recently receiving considerable attention [86, 91, 87, 92, 93, 94].

5.3 Experiments in Cadavers

In this section, use of the knees of fresh, human cadavers to measure absorbed dose at several positions in the joint is described. Each of the knees was injected with a therapeutic dose of ^{165}Dy ferric hydroxide macroaggregate which was prepared just as it would have been for a living patient [?].

As mentioned in Section 5.1, the implantation of detectors in humans is possible, but it entails risks and discomforts that generally are considered to be excessive for the purposes of dosimetry alone. The logistics for internal measurements with cadavers are less severe, but the procedure does have its drawbacks. For example, there are problems in assuring that the distribution of radioactivity in cadavers is representative of that in patients, since the lining cells and macrophages do not actively absorb injected radionuclides. It may be difficult to obtain enough cadaver material for several experiments. And the accurate positioning of radiation dosimeters in the joint often is difficult to accomplish. Nonetheless, the use of cadavers does offer possibilities for correlating measured and calculated doses that cannot be obtained in living patients.

5.3.1 Materials and methods

Cadavers

Four knees, cut from mid-thigh to mid-calf, were obtained from fresh, frozen cadavers at the Harvard Medical School (Boston, MA). None of the knees had evidence of structural joint changes associated with rheumatoid arthritis. Knees 3 and 4 were obtained from the same cadaver. In each of the specimens, the suprapatellar pouch was found to be intact and thus did not appear to present a path for leakage of injected radioactivity out of the joint.

Dosimeters

Radiachromic film dosimeters were cut into 1 cm × 4 cm strips and wrapped in clear plastic packing tape to prevent them from getting wet. The size of the strips was large enough to allow 3 absorbed dose measurements per strip.

Implantation

In each of the four knees, a 15 cm midline incision was made from a distal point just medial to the tibial tubercle to a proximal point along the thigh midline and superior to the patella. The medial subcutaneous tissue then was raised to reveal the medial retinaculum and the vastus medialis obliquus. The exposed quadriceps tendon was cleared of overlying fat, and a standard medial parapatellar arthrotomy was performed, *i.e.*, the joint capsule was cut open. Then the patellofemoral ligament was cut; the patella, everted; and the knee, flexed approximately 90°.

Next the radiachromic film dosimeters were stitched into 5 strategic locations throughout the joint capsule using silk sutures. The locations were: in the posterolateral corner adjacent to the popliteus hiatus, in the posteromedial corner just anterior to the posterior capsule, adjacent to the anterior cruciate ligament, in the lateral gutter of the suprapatellar pouch, and on the deep surface of the quadriceps tendon (as listed in Table 5.9). At the latter three sites, the films were secured with additional silk sutures. The knees were then closed and sewn tight at three separate layers.

Injection

A therapeutic dose of ^{165}Dy ferric hydroxide macroaggregate was prepared for injection following standard procedures [?]. The amount of prepared activity was measured using a Capintec dose calibrator.

Using a 3 cc syringe attached to a three-way stopcock, each of the knees was injected with radioactive ^{165}Dy through a superolateral arthrocentesis portal, and the

Table 5.9: Joint locations at which radiachromic dosimeters were positioned to measure absorbed dose in the knees of cadavers.

Joint location	Description
A	Posterolateral corner
B	Posteromedial corner
C	Adjacent to anterior cruciate ligament
D	Lateral gutter
E	Deep surface of quadriceps tendon

needle track was flushed with 1.5 ml saline. The knees then were manipulated through two complete ranges of motion in an effort to distribute the injected radioactivity as uniformly as possible. The knees were left alone for 24 h to allow time for the radioactive dysprosium to decay. ^{165}Dy has a 2.3 h half-life.

Gamma camera imaging

At 16 h after injection, planar images of the injected knees were obtained using a Picker Dyna gamma camera set to image the 90 keV ^{165}Dy gamma-ray with a 128 $\times$ 128 pixel matrix. The camera's collimator was rotated 180° and covered with an absorbent vinyl pad and positioned so that the knees could be placed directly on top of it for static images.

Analysis

At 24 h after injection, the knees were reopened, and the dosimeters were removed for analysis. The method used to analyze the dosimeters in the cadaver experiments was identical to that used in phantom experiments (see Section 5.2.1).

5.3.2 Results

Results of the 4 cadaver experiments are shown in Table 5.10 as average absorbed dose factors (cGy-cm^2/MBq-s) at the 5 joint locations listed in Table 5.9. In each of the 4 experiments, 3 absorbed dose measurements were obtained at each joint location. The average dose at each location then was converted to an average absorbed dose factor according to the following relation:

$$F_i = \frac{D_i \lambda S_{syn}}{A}, \tag{5.6}$$

Table 5.10: Results of the absorbed dose measurements made at several strategic locations in the knees of fresh, human cadavers. Each of the knees was injected with a therapeutic dose of ^{165}Dy ferric hydroxide macroaggregate. Results are listed as absorbed dose factors (cGy-cm^2/MBq-s).

Location	Factor knee 1	Factor knee 2	Factor knee 3	Factor knee 4
A	$2.3 \times 10^{-2} \pm 5\%$	$5.4 \times 10^{-3} \pm 20\%$	$3.0 \times 10^{-2} \pm 28\%$	$4.1 \times 10^{-2} \pm 9\%$
B	$2.5 \times 10^{-2} \pm 5\%$	0	$2.9 \times 10^{-2} \pm 10\%$	$1.9 \times 10^{-2} \pm 17\%$
C	$2.0 \times 10^{-2} \pm 6\%$	$3.3 \times 10^{-3} \pm 33\%$	$2.0 \times 10^{-2} \pm 5\%$	$3.6 \times 10^{-2} \pm 53\%$
D	$7.5 \times 10^{-2} \pm 5\%$	$3.1 \times 10^{-2} \pm 7\%$	$6.9 \times 10^{-2} \pm 15\%$	$6.0 \times 10^{-2} \pm 80\%$
E	$1.3 \times 10^{-2} \pm 11\%$	$1.0 \times 10^{-1} \pm 5\%$	$5.1 \times 10^{-2} \pm 13\%$	$5.0 \times 10^{-2} \pm 86\%$

where F_i is the average absorbed dose factor (cGy-cm^2/MBq-s), D_i is the average absorbed dose (Gy), λ is the decay constant for ^{165}Dy (8.37×10^{-5} s^{-1}), S_{syn} is an estimate of the total synovial surface area in the joint ($\approx$ 250 cm^2), and A is the amount of injected radioactivity (MBq). The standard deviation also was calculated. Errors reported in the table are equal to one standard deviation.

The errors associated with the reported factors are seen to range from 5 to 86%. In this case, the errors are due primarily to non-uniform distributions of radioactivity in the joints, which resulted in unequal irradiation of the 3 radiachromic film dosimeters at each of the 5 joint locations.

In Figure 5-6, results of the cadaver experiments are compared with the Monte Carlo calculations of absorbed dose factors versus depth in the mathematical joint model. It is important to note that none of the absorbed dose measurements obtained in the cadavers experiments was made at depth in tissue. Instead, each of the measurements was made at a point located on the synovial surface. As a consequence, all the results obtained in the cadaver experiments appear at the same position in the ^{165}Dy profile, on the synovial surface.

5.3.3 Discussion

Non-uniform distribution of injected radioactivity throughout treated joints is recognized as a problem in radiation synovectomy, since rheumatoid synovium which does not receive a therapeutic radiation dose may continue to promote the progression of rheumatoid arthritis in the joint and prevent the relief of symptoms in patients [1, 17, 9]. Regions of rheumatoid synovium located far from the point of injection

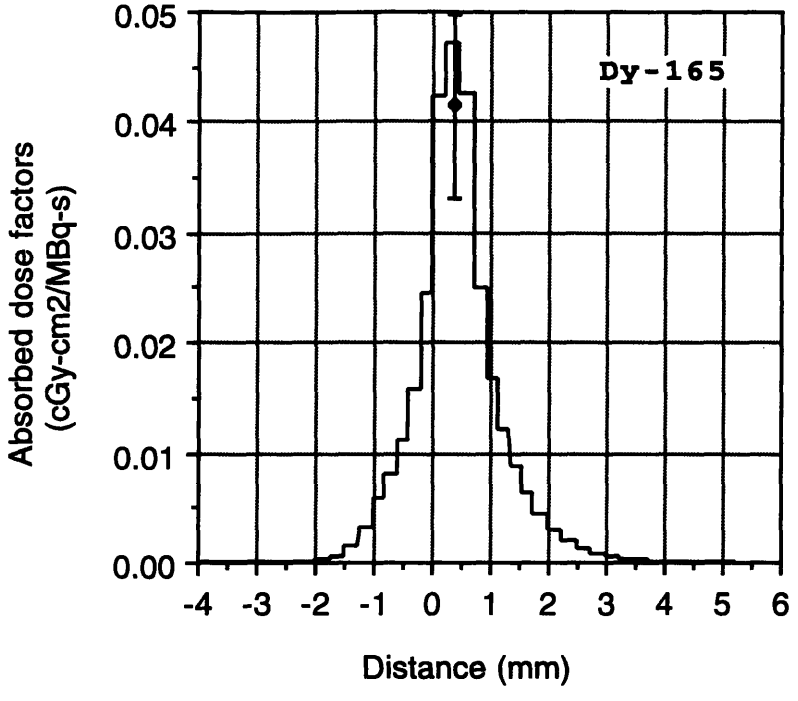

Figure 5-6: Comparison of the absorbed dose factors derived from measurements obtained in the knees of cadavers with the estimates of absorbed dose factors versus depth obtained using Monte Carlo radiation transport simulation in a mathematical model of the joint.

or in joint recesses are particularly of concern. Results of the cadaver experiments presented above provide a means of evaluating magnitude of the problem.

Referring to the results presented in Table 5.10, the distribution of injected radioactivity was seen to be non-uniform in each of the 4 cadaver experiments. If the distributions had been uniform, the 5 absorbed dose factors reported in any one of the 4 knees would have been equal to one another. Instead, the factors were seen to vary from location to location in all 4 knees, with differences as little as 4.1×10^{-2} cGy-cm^2/MBq-s in knee 4 to as large as 1.0×10^{-1} cGy-cm^2/MBq-s in knee 2. For the injection of 10,000 MBq (270 mCi) ^{165}Dy into a knee with a synovial surface area of 250 cm^2, the corresponding variations in absorbed dose are from as little as 20,000 cGy (in knee 4) to as much as 48,000 cGy (in knee 2). Gamma camera scans of the knees 16 h after injection confirmed the unequal distribution.

It is important to note that the distribution of injected radioactivity obtained in the knees of cadavers is *worse* that obtained in the knees of living patients. As described in Chapter 2, radioactivity injected into rheumatoid joints is absorbed by the surface layer of phagocytic lining cells. Autoradiographs of the synovial lining in *live* knees injected with various radionuclides have shown a reasonably even distribution of radioactivity in these cells for several days after injection [2, 3, 4]. In the knees of cadavers however, there is no phagocytic absorption of injected radioactivity since the lining cells and macrophages are dead. As a consequence, the radioactivity is free to move about within the joint and to settle in its lowest recesses. While non-uniform distribution of injected radioactivity may be a problem in live joints, the distribution is even worse in the joints of cadavers.

Combining the results of the 4 cadaver experiments and comparing them with the Monte Carlo calculation synovial surface dose in the joint model, the agreement was seen to be good. As in the phantom experiments, the agreement indicates that the results obtained here using Monte Carlo radiation transport simulation and experiments in the joints of cadavers are indeed accurate.

5.4 Conclusion

Estimates of beta-particle dosimetry in radiation synovectomy can be obtained either through calculation, *e.g.*, using beta dose point kernels (see Section 1.1.1) or Monte Carlo radiation transport simulation, or by experimental measurement in animals, phantoms, and cadavers. The direct measurement of absorbed dose distributions in the joints of patients is possible, but entails inconvenience, discomforts, and inaccuracies generally considered to be excessive.

In this chapter, experiments aimed at measuring beta dose distributions in joint phantoms and the knees of cadavers were described. One goal of the experiments was to obtain the depth-data necessary to extrapolate beta dose distributions in the

joints of patients treated with radiation synovectomy. These data were measured in the joint phantoms, and the results were presented in Table 5.7. Another goal of the experiments was to obtain the data necessary to estimate the distribution of injected radioactivity throughout treated joints. Using the knees of cadavers, these data also were measured, and the results were presented in Table 5.10.

In the next three chapters, use of the $^{10}B(n,\alpha)$ nuclear reaction as a probe to examine the pathology of rheumatoid arthritis is discussed. In Chapter 6, a rationale for the experiments is presented; and in Chapters 7, experiments aimed at determining the temporal and spatial distribution of ^{10}B in live samples of excised human rheumatoid synovium are described.

Chapter 6

Examining the Pathology of Rheumatoid Arthritis

6.1 Introduction

An unanswered question in the treatment of rheumatoid arthritis through synovectomy is: how much of the synovium must be removed or killed in order to arrest progression of the disease and provide the patient with symptomatic relief? For the most part, current treatments using low-energy beta-emitters or surgery can be described as attempting to remove the entire synovial membrane. Existing data suggest, however, that removal of only the surface layer of lining cells may be sufficient (see below).

It is the purpose of this chapter to present the rationale for a series of experiments aimed at answering the above question. The approach is to use the $^{10}B(n,\alpha)$ nuclear reaction as a probe to examine the fundamental pathology of rheumatoid arthritis and determine whether killing the synovial lining cells alone could arrest progression of the disease, or whether killing the entire synovium is required. This nuclear reaction was chosen specifically because the high LET, short range particles emitted are capable of producing significant amounts of radiation-induced damage limited only to boronated cells and their nearest neighbors. Provided one boron preparation can be used to deliver ^{10}B exclusively to the lining cells and a different boron preparation can be used to deliver ^{10}B to the entire synovium, the reaction can be used to selectively kill varying thicknesses of synovium. Various analytical techniques then can be used to evaluate the treatment's effects on the progression of rheumatoid arthritis, both *in vitro* and *in vivo*.

The chapter begins with a review of the data which support the hypothesis that killing the lining cells alone may be sufficient to temporarily arrest progression of rheumatoid arthritis and provide patients with symptomatic relief of the disease.

Then, the $^{10}B(n,\alpha)^{7}Li$ nuclear reaction is described, and the two boron preparations selected to boronate either the lining cells alone or the entire synovium are presented. Use of the reaction as a probe to examine the pathology of rheumatoid arthritis is described in Chapter 8.

6.2 Is Removal of the Lining Cells Sufficient?

As described in Chapter 2, rheumatoid arthritis is a chronic autoimmune disease of unknown origin affecting roughly 1% of the world's adult population [20]. Although rheumatoid arthritis has many clinical manifestations, its characteristic feature is persistent inflammation of the synovium. If left untreated, the inflammation leads eventually to complete destruction of bone and articular cartilage. The physical pain, deformation, and disability which result are enormous.

Treatments for rheumatoid arthritis traditionally are aimed at relieving the synovial inflammation, and there is a wide variety of drugs available which work for most patients. For joints unresponsive to traditional drug therapy, however, alternative treatments are required. In the past, several alternatives have been developed. These include surgery and radiation synovectomy, each of which is aimed at removing, or killing, the inflamed synovium with the expectation that regenerated tissue will be free of disease for 2 to 5 years and the pain and symptoms thereby temporarily alleviated (see Chapter 2). Both procedures aim to remove several mm of tissue.

As understanding of the pathology of rheumatoid arthritis increases, however, it appears that removal of the entire synovium may not be required to arrest progression of the disease and provide patients with symptomatic relief. Instead, removal of only the surface layer of lining cells may be sufficient. There are a number of reasons why this hypothesis has come into favor and these are discussed below.

Pathology of rheumatoid arthritis. Although the precise mechanisms through which bone and articular cartilage are destroyed by rheumatoid arthritis are not completely understood, most of the destruction is known to occur in juxtaposition to the pannus that spreads to cover the articular cartilages [23]. This vascular granulation tissue is composed of fibroblasts, small blood vessels, and numerous mononuclear cells. More importantly, however, along its surface reside large numbers of intensely active synovial lining cells [23]. As described in Section 2.3.2, these cells not only are engaged in rapid, neoplastic-like proliferation, but they also are responsible for secreting high levels of proinflammatory cytokines and destructive enzymes into the joint [23]. There is now a good deal of evidence to suggest that the secreted cytokines and enzymes go on to play a central role in the amplification and perpetuation of the chronic synovial inflammation and in the subsequent degradation of articular carti-

lage and bone [21]. It therefore seems reasonable to hypothesize that if the source of proinflammatory cytokines and destructive enzymes were removed, *i.e.*, the lining cells were killed, then the progression of rheumatoid arthritis in the joint would be arrested, at least temporarily.

Clinical experience. Over the past 40 years, clinical experience with radiation synovectomy has demonstrated that a wide variety of beta-emitting radionuclides can be used to slow progression of rheumatoid arthritis in treated joints and provide patients with symptomatic relief of the disease (see Section 2.4). Large differences in the decay energies of these radionuclides, however, result in significant variations in the thickness of synovium killed by each. Since the low energy beta-emitters appear to be as effective as those with substantially greater soft tissue penetration [8], it seems reasonable to conclude that the localized dose imparted by low energy emitters is sufficient to slow the progression of rheumatoid arthritis. For the most part, this localized dose is delivered to the first mm or so of synovium, a range which is sufficient to kill the surface layer of lining cells. The hypothesis, therefore, is that the localized dose imparted by the low energy emitters kills the true target, *i.e.*, the lining cells, and that deeper penetration is not required.

In addition, radiation synovectomy is known through clinical experience to be most effective in the earlier stages of rheumatoid arthritis [8]. In studies in which rheumatoid arthritis patients have been divided into groups exhibiting varying stages of the disease, patients treated at earlier stages invariably respond more favorably than those treated at later stages. Since the early stages of rheumatoid arthritis are characterized by large numbers of intensely active, proliferating lining cells with little joint damage, and the later stages of rheumatoid arthritis are characterized by fewer and less active lining cells but extensive cartilage damage, it seems reasonable to suppose that removing the lining cells (before the onset of cartilage destruction) is essential to producing favorable results in patients. Again, the hypothesis is that *only* the lining cells must be killed.

It is worth adding that radiation synovectomy has also been used *unsuccessfully* to control the symptoms of patients with osteoarthropathy [95, 96]. In these patients, symptoms have arisen due to advanced destruction of articular cartilage and bone-on-bone erosions; the surface layer of synovial lining cells in the affected joints is likely to be nonexistent and plays no central role in the progression of the disease. As a result, the radiation therapy provides no benefit.

Table 6.1: Thermal neutron capture cross section values of various nuclides.

Nuclide	Cross section
^{3}He	5,500 b
^{6}Li	953
^{10}B	3837
^{113}Cd	20,000
^{149}Sm	41,500
^{157}Gd	240,000
^{155}Gd	58,000
^{174}Hf	400
^{199}Hg	2,000
^{235}U	678

6.3 ^{10}B(n,α) Nuclear Reaction

There are a number of nuclides which have a natural affinity for absorbing thermal neutrons, *i.e.*, neutrons with kinetic energy $\approx$ 0.025 eV. This property, referred to as the thermal neutron capture cross section, is measured in barns, where 1 b = 10^{-24} cm^2. A short list of nuclides with high thermal neutron capture cross sections can be found in Table 6.1.

A naturally occurring isotope of boron, ^{10}B has one of the highest thermal neutron capture cross sections of the non-radioactive nuclides. Upon capturing a thermal neutron, the nuclide undergoes an (n,α) nuclear reaction and releases an α-particle and a recoiling ^{7}Li ion. In 94% of the reactions, a 0.48 MeV γ-ray is also released.

$$^{10}\mathrm{B} + \mathrm{n}_{th} \rightarrow \alpha + ^{7}\mathrm{Li} + (0.48\ \mathrm{MeV}\ \gamma\ \mathrm{in}\ 94\%\ \mathrm{of\ the\ reactions}) \qquad (6.1)$$

The nuclear reaction has a total Q value of 2.79 MeV. If the reaction proceeds without releasing a 0.48 MeV γ-ray, then its energy is divided between the two particles, such that the α-particle is released with 1.78 MeV kinetic energy, and the ^{7}Li ion is released with 1.01 MeV kinetic energy. On the other hand, if the reaction results in the emission of a 0.48 MeV γ-ray, then only 2.33 MeV is available to the particles; and the α-particle is released with 1.47 MeV kinetic energy, while the ^{7}Li ion is released with 0.84 MeV kinetic energy.

Both the particles released by the reaction are high LET, short range particles, *i.e.*, they give rise to closely spaced ionizations in sharply defined linear tracks that have a combined range in tissue of approximately 10-14 μm, a distance which is on

the order of a typical cell diameter. As a result, they are capable of generating large amounts of radiation-induced damage in boronated cells exposed to thermal neutrons and their nearest neighbors. In general, this damage is irreversible; and if the cell nucleus is involved, it could lead eventually to cell death.

The theoretical advantage of the reaction is that it is a two component, or binary, system. The first component consists of the delivery of ^{10}B to the target cells, while the second component involves the exposure of boronated cells to thermal neutrons. Combined, the two components provide a means to selectively deliver a therapeutic radiation dose limited only to boronated cells and their nearest neighbors.

Thermal neutron irradiation of the target cells, however, also involves the irradiation of other, non-target, tissues located in the target's vicinity. Although the thermal neutron capture cross sections of the elements normally found in the body's tissues are several orders of magnitude lower than that of ^{10}B (see Table 6.2), two of these elements, H and N, are present in such high concentrations that their capturing of neutrons contributes significantly to the total radiation absorbed dose imparted to *all* the exposed tissues. Thermal neutron capture in ^{1}H, for instance, results in an (n,γ) nuclear reaction and creates an extended source of deeply-penetrating photons capable of irradiating the entire body. Thermal neutron capture in ^{14}N, on the other hand, results in an (n,p) nuclear reaction, creates a source of high LET, short range protons in all the cells exposed to thermal neutrons.

To minimize this dose to non-target tissues, ^{10}B concentrations (parts per million or ppm) delivered to the target cells should be as large as possible so that the neutron fluence (n/cm^2) can be kept as small as possible. The result is to maximize the likelihood of inducing the $^{10}B(n,\alpha)^{7}Li$ nuclear reaction in target cells while minimizing that of the $^{14}N(n,p)^{14}C$ and $^{1}H(n,\gamma)^{2}H$ reactions in non-target tissues. It has been estimated that a target cell ^{10}B concentration of 50 ppm would result in an absorbed dose to the target cells that is over 7 times greater than that to surrounding, non-target tissues [97].

A major advantage of a binary system is that the two components can be managed independently of one another. For instance, the time interval between boron administration and thermal neutron irradiation can be chosen to optimize the boron concentration differential between target and non-target cells. In addition, the thermal neutron beam often can be collimated and directed to limit the exposure of non-target cells. The system thus can be manipulated to maximize the dose to target cells while minimizing that to non-target cells.

6.3.1 Two Boron Preparations

The two boron preparations chosen to selectively boronate either the lining cells alone or the entire synovium are, respectively, boron particulate and boric acid. The

Table 6.2: Thermal neutron capture cross section values of elements normally found in the body's tissues.

Element	Cross section
H	0.332 b
C	0.0037
N	1.75
O	0.0002
Na	0.536
Mg	0.069
P	0.19
S	0.52
Ca	0.44
Cl	33.8

rationale for choosing these two preparations is described below.

Boron particulate. As described in Chapter 2, type-A lining cells are phagocytic and have elongated bodies which send processes mostly toward the synovial surface where they emerge and are available to absorb foreign matter and waste from the synovial fluid. Boron particulate (*i.e.*, boron metal in particulate form) injected into the synovial fluid and large enough to be identified as foreign matter by these cells (1 nm to 5 μm) thus should be actively absorbed. Macrophages along the synovial surface also should be able to identify and phagocytize the particulate. As a result, it appears reasonable to hypothesize that high concentrations of ^{10}B, in particulate form, can be delivered to the type-A lining cells and macrophages. In Chapter 7, *in vitro* experiments aimed at verifying the above hypothesis and determining the temporal and spatial distributions of boron particulate uptake by the lining cells are described.

Boric acid. Use of the $^{10}B(n,\alpha)$ nuclear reaction to selectively kill the entire synovium also is of interest. Killing several mm of tissue however requires a reasonably uniform distribution of ^{10}B throughout the entire synovium. Boron particulate cannot be used to obtain such a distribution, since the cells capable of absorbing the particulate are not found in abundance throughout the entire synovium; they are found instead almost exclusively in a synovial surface layer less than 0.5 mm thick.

Use of boric acid, H_3BO_3, is proposed as an alternative. Boric acid is an inexpensive, non-toxic, water soluble compound which, like other water soluble compounds,

can be expected to rapidly and freely diffuse throughout the entire synovium. The experiments mentioned above and used to determine the temporal and spatial distribution of boron particulate uptake by the lining cells also were used to examine the diffusion of boric acid throughout the entire synovium. Results of the experiments are found in Chapter 7.

6.4 Conclusion

In this chapter, use of the $^{10}B(n,\alpha)^{7}Li$ nuclear reaction as a probe to examine the fundamental pathology of rheumatoid arthritis was presented. For various reasons, based on clinical experience and current understanding of the pathology of rheumatoid arthritis, it appears reasonable to hypothesize that complete removal, *i.e.*, killing, of the lining cells alone could stop the inflammatory response and prevent additional cytokine and enzyme secretion into the joint, at least temporarily. Two boron preparations (boron particulate and boric acid) thus were proposed as candidates to examine the effect of selectively killing the lining cells alone or the entire synovium. The $^{10}B(n,\alpha)$ reaction was chosen specifically because the high LET, short range particles emitted are capable of generating large amounts of radiation damage only in boronated cells exposed to thermal neutrons and their nearest neighbors. In general, this damage is irreversible; and if the cell nucleus is involved, it can lead eventually to cell death.

In the next chapter, experiments aimed at quantifying the temporal and spatial distribution of boron particulate and boric acid uptake in excised samples of human rheumatoid synovium are described. Prompt gamma neutron activation analysis was used to quantify the temporal distribution of ^{10}B uptake in the samples, while neutron induced alpha-track autoradiography was used to examine the spatial distribution.

Chapter 7

Temporal and Spatial Distribution of ^{10}B Uptake

7.1 Introduction

Before using the $^{10}B(n,\alpha)$ nuclear reaction to examine the effect of killing the lining cells alone versus the entire synovium, information regarding the distribution of ^{10}B in the synovium is needed. In particular, quantitative information regarding the temporal and spatial distribution of boron particulate and boric acid uptake is needed.

In this chapter, use of prompt gamma neutron activation analysis and neutron-induced alpha-track autoradiography to determine the temporal and spatial distribution of ^{10}B uptake in live, human rheumatoid synovium is described. The prompt gamma neutron activation analysis experiments are described first. Samples of human rheumatoid synovium were incubated for varying time periods *in vitro* with either boron particulate or boric acid. Then activation analysis was used to determine the bulk ^{10}B content of each sample. The neutron-induced alpha-track autoradiography experiments are described second. Again, samples of human rheumatoid synovium were incubated *in vitro* with either boron particulate or boric acid. Then the samples were sliced and autoradiography was used in an attempt to examine the spatial distribution of ^{10}B in each.

7.2 Prompt Gamma Neutron Activation Analysis

Neutron activation analysis, in general, is an analytical technique aimed at quantifying the elemental composition of some materials. The sample to be evaluated is exposed to a flux of neutrons, typically from a nuclear reactor. Since many atomic nu-

clei have high thermal neutron capture cross sections for (n,γ)-type nuclear reactions, the irradiation results in the production of a great variety of gamma-ray emitting radionuclides, each of which decays with a characteristic energy and half-life. Spectroscopic analysis of the emitted gamma-rays is used to identify radionuclides in the sample. Sometimes the product of a nuclear reaction has such a short half-life that the emitted gamma-rays can only be measured during the actual time of irradiation. When sample irradiation and spectroscopic analysis of the emitted gamma-rays are conducted simultaneously, the technique is called prompt gamma neutron activation analysis.

In prompt gamma neutron activation analysis, the activity of a given radionuclide, which is present only during irradiation, is given by the following expression:

$$A = N\phi\sigma, \tag{7.1}$$

where A is the activity (Bq), N is the number of target atoms, ϕ is the flux of thermal neutrons (n/cm^2-s), and σ is the thermal neutron capture cross section (cm^2).

While Eqn. 7.1 can be used to calculate N for a given thermal neutron flux ϕ, cross section σ, and absolute activity A, accuracy of the analysis is subject to a wide variety of errors, including variations in the thermal neutron flux and difficulties in determining the absolute activity of the sample. A simpler approach to determining N is based on a comparison of the sample's activity to that of a standard. The sample and standard are activated and measured under as nearly identical conditions as is possible. If the standard contains a known number N_s of the target atoms to be quantified, then the number of target atoms in the sample N_x is given by:

$$N_x = N_s\frac{A_x}{A_s}, \tag{7.2}$$

where A_x is the activity of the product radionuclide in the sample and A_s is the activity in the standard [98]. This relative approach was used in this work to determine the bulk ^{10}B content of samples of human rheumatoid synovium incubated *in vitro* with either boron particulate or boric acid (see Section 7.2.1).

MIT prompt gamma neutron activation analysis facility

A prompt gamma neutron activation analysis facility is operated at the MIT Nuclear Reactor Laboratory (Cambridge, MA) using a diffracted thermal neutron beam. The beam has been diffracted to result in significantly reduced numbers of fast neutrons and core gamma-rays at the sample position. As a consequence, very short sample-to-detector distances to be used during irradiation without overwhelming the detector. The short distances provide a means to compensate for the loss of thermal neutron

flux intensity due to diffraction. The resulting sensitivity of the facility, *i.e.*, the smallest concentration of target atoms it can be used to measure, exceeds that of similar, direct beam facilities operated at nuclear reactors twice as powerful as the MIT reactor [99].

A schematic diagram of the facility is shown in Figure 7-1. A well moderated beam of thermal neutrons emerging from the reactor's D_2O reflector is incident on a multilayered graphite monochromator. The monochromator is composed of 3 thin ($\approx$ 3 mm) pyrolytic graphite crystals which have been aligned to diffract the incident beam by 21°. The reflected neutrons have 0.0143 eV kinetic energy. To further reduce contamination of the diffracted beam by fast neutrons and gamma-rays, a single sapphire crystal (15 cm long $\times$ 5 cm diameter) is positioned downstream of the monochromator. The crystal transmits 80% of the 0.0143 eV neutrons while transmitting less than 1% of the epithermal neutrons, 0.5% of the fast neutrons, and 3 to 20% of the gamma-rays in the energy range 1 to 6 MeV, respectively. Collimators are used downstream of the crystal to define the final beam shape. At the sample position (0.9 m from the monochromator), the emerging beam of 0.0143 eV neutrons has a flux of 6×10^6 n/cm^2-s and a diameter of $\approx$ 1-2 cm.

A 122 cm^3 n-type solid state Ge detector views the sample at a 90° angle. To reduce the damaging effects of stray neutrons and the background count of scattered gamma-rays, the sides of the detector are shielded by at least 7.5 cm lead and 4 cm lithium carbonate. The sample-facing end of the detector is shielded from stray neutrons by 1.25 cm lithium carbonate, enriched in ^{6}Li. The resulting background count rates are sufficiently low to allow the detector to be positioned very close to the sample, $\approx$ 4 cm away.

A multichannel analyzer (MCA) is used for spectroscopic analysis of the prompt gamma-rays. The MCA is a Canberra Series 85 analyzer with 4096 channels.

Prompt gamma neutron activation analysis of ^{10}B

Use of prompt gamma neutron activation analysis to determine the ^{10}B content of materials has been reported by others [100, 101, 102, 103]. The prompt gamma-ray detected is the 478 keV gamma-ray emitted from the excited state of ^{7}Li in 93.5% of $^{10}B(n,\alpha)$ nuclear reactions. Advantages of the technique include the fact that the bulk ^{10}B content of material samples can be determined regardless of the chemical form of the boron. Prompt gamma neutron activation analysis also is non-destructive, resulting in no observable changes to the samples.

7.2.1 Materials and Methods

Samples of human rheumatoid synovium were incubated for varying time periods with either boron particulate or boric acid. Then prompt gamma neutron activation

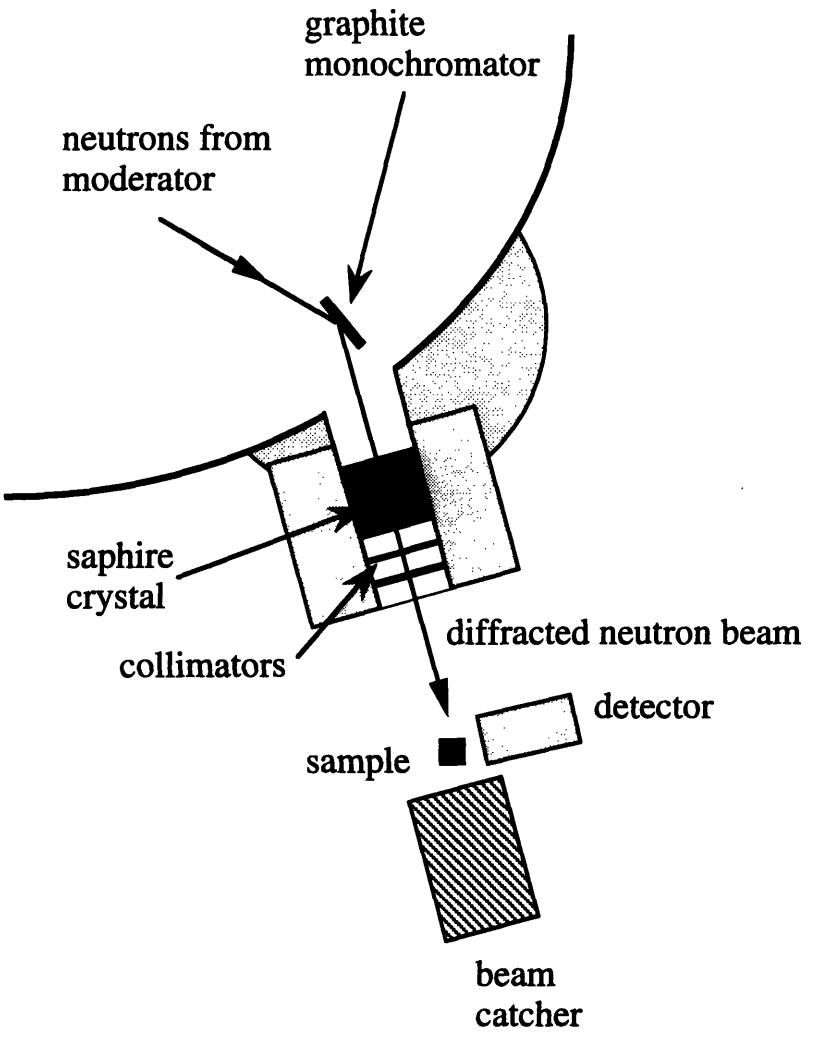

Figure 7-1: Schematic diagram of the prompt gamma neutron activation analysis facility operated at MIT. The facility uses a diffracted thermal neutron beam to reduce the numbers of fast neutrons and gamma-rays at the sample position.

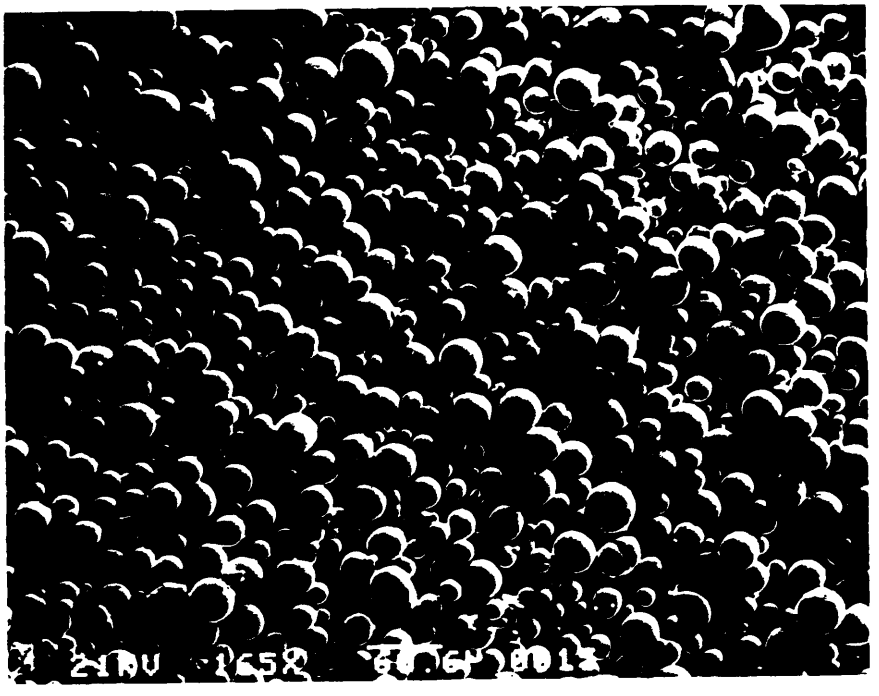

Figure 7-2: Scanning electron micrograph of the boron particulate. Magnification 165×. A 60 μm bar at the bottom of the micrograph can be used to estimate the size distribution of the particles.

analysis was used to determine the bulk ^{10}B content of each sample.

The boron particulate is 99.9% boron metal, enriched in ^{10}B (94%). As shown in Figures 7-2 and 7-3, the particles are spherical and have a wide distribution of sizes. The larger particles are seen to be nearly 40 μm in diameter, while the smaller particles are less than 5 μm. The average-sized particle is estimated to have a diameter of $\approx$ 15 μm.

The boric acid was prepared by dissolving H_3BO_3 in deionized water. The H_3BO_3 used is Standard Reference Material 951, as certified by the National Bureau of Standards (Washington, D.C.). It was prepared by the JT Baker Company (Phillipsburg, NJ) for the Argonne National Laboratory (Argonne, IL) and is 19.827% ^{10}B. For these experiments, a 400 ppm-^{10}B boric acid solution was prepared by dissolving 310 mg H_3BO_3 per ml deionized water.

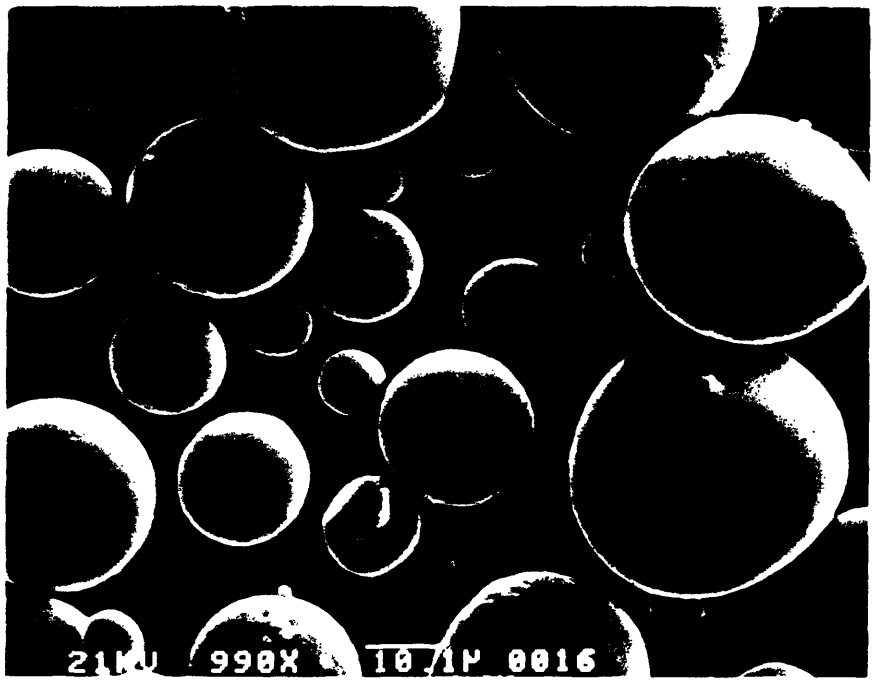

Figure 7-3: Scanning electron micrograph of the boron particulate taken at a higher magnification 1000×.

Incubation

Boron particulate. Live, human rheumatoid synovium was obtained from the operating room at Brigham and Women's Hospital (Boston, MA) and cut into several samples, each $\approx$ 0.3-0.4 g. The samples were divided into the following groups:

1. 4 samples sprinkled with 10 mg particulate and incubated in medium for 1 h
2. 4 samples sprinkled with 10 mg particulate and incubated in medium for 24 h
3. 4 samples incubated in medium for 24 h, then sprinkled with 10 mg particulate and incubated in fresh medium for 1 h
4. 2 samples incubated in medium for 24 h as controls.

The incubation medium was RPMI 1640 cell culture medium, which is 1% penicillin streptomycin and 10% fetal bovine serum, and has been heat inactivated. After incubation, each of the samples was rinsed of excess particulate for about 1 min using a gentle stream of saline solution. The rinsed samples then were sealed in teflon vials for activation analysis.

Boric acid. The 400 ppm-^{10}B boric acid solution was mixed with RPMI cell culture medium to yield a boronated incubation medium having a ^{10}B concentration of 90 ppm. Samples of live, human rheumatoid synovium were obtained and cut into samples as described above, but divided into the following groups:

1. 4 samples incubated in boronated medium for 1 h
2. 4 samples incubated in boronated medium for 4 h
3. 4 samples incubated in boronated medium for 24 h
4. 2 samples incubated in medium (non-boronated) for 24 h as controls.

After incubation, each of the samples was rinsed of excess boron for about 1 min using a gentle stream of saline solution. The rinsed samples then were sealed in teflon vials for activation analysis.

Analysis

Calibration curve. Standard solutions of 20, 40, and 50 ppm-^{10}B boric acid were prepared and packaged in teflon vials for comparison with the samples. A calibration curve was constructed as follows.

An empty teflon vial was analyzed at the MIT prompt gamma neutron activation analysis facility to determine the background count rate of gamma-rays resulting from

the $^{1}H(n,\gamma)$ nuclear reaction. To determine the background count rate of gamma-rays resulting from the ^{10}B neutron capture reaction, a teflon vial filled with deionized water was analyzed. The boron contents of deionized water and soft tissue were assumed to be reasonably similar. Each of the standard solutions then was analyzed to determine its count rates of ^{1}H and ^{10}B gamma-rays.

The concentration of ^{10}B in the standards was plotted versus the following ratio:

$$\frac{B_x - B_{bg}}{H_x - H_{bg}}, \tag{7.3}$$

where B_x and H_x are, respectively, the ^{10}B and ^{1}H count rates of the sample and B_{bg} and H_{bg} are, respectively, the background count rates of ^{10}B and ^{1}H. The ratio is directly proportional to the absolute activity of ^{10}B induced in each standard.

A sample calibration curve is shown in Figure 7-4. The ratio of ^{10}B to ^{1}H count rates has been used to reduce the effects of inconsistent sample positioning in the beam, any variations in the thermal neutron flux over the course of the analysis, and to avoid having to determine the absolute activity A of each sample.

Sample analysis. To analyze the samples of boronated synovium, each was irradiated for 300 s to determine the count rates of ^{10}B and ^{1}H gamma-rays. Then, the ratio defined above was calculated and used with the calibration curve to estimate the bulk ^{10}B content of each sample.

7.2.2 Results

Results of the experiments are presented in Tables 7.1 and 7.2 as average bulk ^{10}B concentrations in each of the 8 groups of samples delineated above.

Boron particulate. For the samples incubated with boron particulate, a substantial amount of boron uptake is seen to occur within the first hour of incubation, resulting in an average bulk ^{10}B concentration of 860±29% ppm. With 24 h of incubation, the absorption of the particulate is seen to continue, and the average bulk ^{10}B concentration increases to 2300±70% ppm. In the control samples, which were incubated for 24 h in medium alone, the average bulk ^{10}B concentration is less than 1 ppm.

It also is of interest to have an indication of how long the excised synovium can be expected to remain active *in vitro*. With this question in mind, an additional group of samples first was incubated in medium for 24 h, then sprinkled with boron particulate and incubated in fresh medium for 1 h, and finally rinsed and packaged for analysis. The results show an average bulk ^{10}B concentration in this group of 1500±33% ppm.

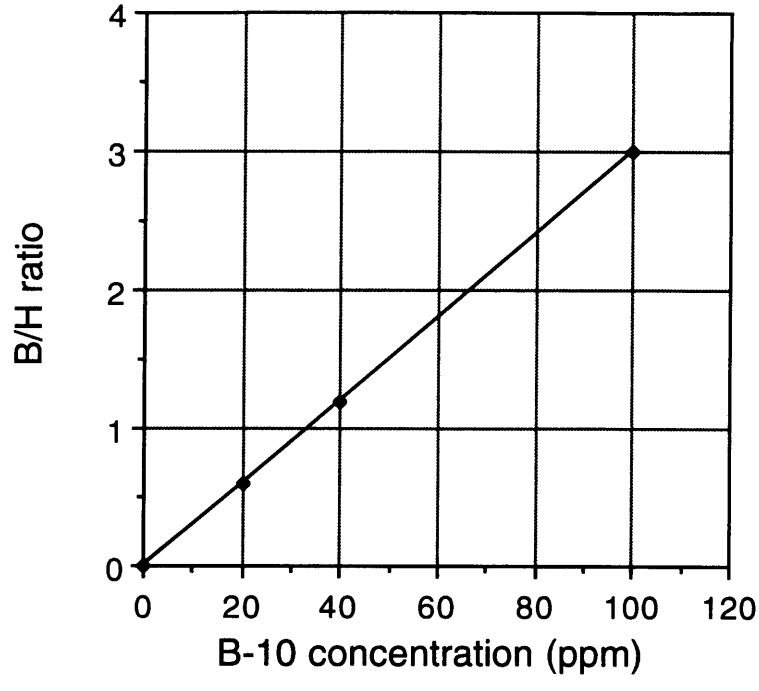

Figure 7-4: A sample calibration curve for the analysis of bulk ^{10}B content at the MIT prompt gamma neutron activation analysis facility.

Table 7.1: Temporal distribution of bulk BORON PARTICULATE uptake in human rheumatoid synovium.

Group	^{10}B Concentration
1 h incubation with B particulate	860±29% ppm
24 h incubation with B particulate	2300±70%
24 h incubation and then 1 h incubation with B particulate	1500±33%
24 h incubation in medium only (control)	<1

Table 7.2: Temporal distribution of bulk BORIC ACID uptake in human rheumatoid synovium.

Group	^{10}B Concentration
1 h incubation in boronated medium	40±15% ppm
4 h incubation in boronated medium	41±15%
24 h incubation in boronated medium	52±15%
24 h incubation in non-boronated medium (control)	<1

The excised synovium thus can be expected to remain active for at least 24 h.

Boric acid. For the samples incubated with boric acid, substantial absorption again is seen in the samples incubated for only 1 h. Samples incubated in boronated medium (90 ppm ^{10}B) for 1 h demonstrate an average bulk ^{10}B concentration of 40±15% ppm. With 4 h of incubation in the boronated medium, the average bulk ^{10}B concentration remains nearly constant at 41±15% ppm. With a much longer incubation time of 24 h, however, it is seen to increase to 52±15% ppm. The control samples, incubated for 24 h in non-boronated medium, have an average bulk ^{10}B concentration of less than 1 ppm.

It is important to realize that the concentrations reported above are *bulk* concentrations of ^{10}B in the analyzed samples. Information regarding the spatial distribution of ^{10}B in the samples is not included. Instead, the reported bulk concentrations essentially reveal the relative number of ^{10}B atoms in the entire irradiation volume, averaged over that volume and over the number of samples in each group. Experiments aimed at determining the spatial distribution of ^{10}B in the samples are presented in the next section.

7.3 Neutron-induced Alpha-track Autoradiography

Autoradiography, in general, is an established imaging technique which has been developed to quantify the spatial distribution of various radionuclides in sliced material samples [104, 105, 106]. Typically, the sample slice is placed against an x-ray film. Then, as the radionuclide in the slice decays, radiation emitted from the slice interacts with the layer of silver bromide in the film. After the film is developed, a map of the distribution of radionuclides in the sample is displayed, with dark areas of the film corresponding to radioactivity in the sample [107]. However, this procedure can only be used to examine the spatial distribution of *radio*nuclides. To examine the spatial distribution of non-radioactive nuclides, *e.g.*, ^{10}B, other techniques are required.

In some cases, it is possible to label the non-radioactive nuclide of interest with tritium and to use beta-autoradiography to examine the distribution of tritium in the sample slices [108]. In other cases, it is possible to mount the sample slice on a detector and irradiate the assembly with thermal neutrons to induce (n,α)-type nuclear reactions in the slice [109, 110, 101]. Some of the emitted alpha-particles will emerge from the slice in the direction of the detector and create tracks of stress points in it. By chemical etching, these tracks can be transformed into pits that are visible with the aid of an optical microscope. The latter technique is called neutron-induced alpha-track autoradiography, and this technique was used here in an attempt to examine the spatial distribution of ^{10}B in samples of human rheumatoid synovium incubated *in vitro* with either boron particulate or boric acid (see Section 7.3.1).

Neutron-induced alpha-track autoradiography of ^{10}B

In neutron-induced alpha-track autoradiography of ^{10}B, alpha-particles emitted from the ^{10}B(n,α) nuclear reaction are recorded in a track-etch detector [111]. By chemical etching, pits visible with the aid of an optical microscope are formed at the sites where alpha-particles have passed through the detector material and created stress point tracks in it. The size of each pit depends on the amount of energy deposited by the alpha-particles and on the etching techniques that are used (*e.g.*, time, temperature, etchant, etc.) [112]. To determine quantitative information regarding the spatial distribution of ^{10}B in the samples, the number of tracks in a region of known area can be counted and compared with the numbers obtained from standard specimens of known ^{10}B concentration, prepared in the same manner as the samples [113].

Suitable track-etch detectors for neutron-induced alpha-track autoradiography include cellulose nitrate LR 115 type 1 films (Kodak) [114] and polycarbonate CR 39 plates (allyl diglycol carbonate, American Acrylics and Plastic, CT). Both track-etch detectors are insensitive to gamma-rays and beta-particles, which eliminates the need

to distinguish between different types of tracks. However, both detectors are sensitive to protons with less than 400 keV kinetic energy, such as those produced by the $^{14}N(n,p)^{14}C$ nuclear reaction. The cellulose nitrate films have the added disadvantage of containing N so that protons emitted from the neutron capture reaction in N in the detector itself can interfere with the evaluation. CR 39, on the other hand, contains no N. CR 39 thus is the track-etch detector used here in an attempt to examine the spatial distribution of ^{10}B in boronated synovium.

7.3.1 Materials and Methods

Samples of human rheumatoid synovium were incubated with either boron particulate or boric acid. Then the samples were sliced using a cryostatic mycrotome. When a slice to be imaged was obtained, it was mounted directly onto a polycarbonate CR 39 track-etch detector for irradiation. The very next slice then was mounted onto a glass slide for staining. Neutron-induced alpha-track autoradiography was used in an attempt to examine the spatial distribution of ^{10}B in the slices mounted on CR 39, while the slices mounted on glass slides were stained for histological analysis. Superimposition of the etched tracks and stained tissue slices then could be used to examine the spatial distribution of ^{10}B in the samples [115].

The boron particulate, as described in Chapter 7, is 99.9% boron metal, enriched in ^{10}B (94%). As shown in Figures 7-2 and 7-3, the particles are spherical and have a wide distribution of sizes, ranging from 5 to 40 μm. The average-sized particle is estimated to have a diameter of $\approx$ 15 μm.

The boric acid was prepared by dissolving H_3BO_3 in deionized water. As described in Chapter 7, the H_3BO_3 used is Standard Reference Material 951, as certified by the National Bureau of Standards (Washington, D.C.). For these experiments, a 400 ppm-^{10}B boric acid solution was prepared by dissolving 310 mg H_3BO_3 per ml deionized water. The boric acid solution then was mixed with RPMI cell culture medium to yield a boronated incubation medium with a ^{10}B concentration of 90 ppm.

Sample incubation and slicing

Live, human rheumatoid synovium was obtained from the operating room at Brigham and Women's Hospital (Boston, MA) and cut into several samples, each $\approx$ 0.3-0.4 g. The samples were divided into the following groups:

1. 3 samples sprinkled with 10 mg boron particulate and incubated in medium for 2 h
2. 3 samples incubated in boronated medium (boric acid and medium) for 2 h
3. 3 samples incubated in medium only (control)

The incubation medium was RPMI 1640 cell culture medium, which is 1% penicillin streptomycin and 10% fetal bovine serum, and has been heat inactivated. After incubation, each of the samples was rinsed of excess boron for about 1 min using a gentle stream of saline solution. Then samples were frozen, to fix the spatial distribution of ^{10}B in the synovium, and embedded in Optical Cutting Temperature compound (Miles, Inc., Diagnostic Division, Elkhart, IN).

Using a cryostatic microtome, the frozen samples were cut into 10 μm slices. When a slice to be imaged was obtained, it was mounted directly onto a polycarbonate CR 39 track-etch detector for irradiation, and the very next slice was mounted onto a glass slide for staining.

Neutron irradiation

The slices mounted on CR 39 track-etch detectors were packed in dry ice and irradiated at the MIT Nuclear Reactor Laboratory (Cambridge, MA) for 15 min at 100 kW in beam port position 1PH1. The capture of thermal neutrons by ^{10}B in the slices resulted in the emission of alpha-particles and recoiling ^{7}Li ions from the ^{10}B disintegration sites. Some of the emitted particles emerge from the slice in the direction of the detector and create tracks of stress points in it.

Etching

The polycarbonate CR 39 detectors were etched by soaking for 18 min in 6.5 N NaOH at 70 °C. Pits were formed in the detectors at the sites of stress point tracks produced by particles emerging from the slices during irradiation.

Staining

The sample slices mounted on glass slides were stained with hematoxylin-eosin, following a standard procedure that has been used for over a century to stain cell membranes and nuclei.

Analysis

The spatial distribution of pits was correlated to the stained sample slices using the superimposition technique [115]. Micrographs of both the etched detectors and the stained slices were obtained and scanned into a computer. Then the digitized images were superimposed to reveal the spatial distribution of ^{10}B in the samples.

7.3.2 Results

Virtually no tracks were found on any of the CR 39 track-etch detectors. As a consequence, information regarding the spatial distribution of ^{10}B in the samples of boronated synovium was not obtained. There are a number of possible reasons why tracks were not formed on the detectors, and these are discussed in the next section.

7.4 Discussion

Before using the $^{10}B(n,\alpha)$ nuclear reaction to examine the effect of killing the lining cells alone versus the entire synovium, quantitative information regarding ^{10}B uptake in human rheumatoid synovium is needed. Prompt gamma neutron activation analysis was used to obtain the temporal distribution of ^{10}B uptake in synovial samples incubated *in vitro* with either boron particulate or boric acid. Neutron-induced alpha-track autoradiography was used in an attempt to obtain the spatial distribution of ^{10}B uptake in the samples.

Prompt gamma neutron activation analysis

Prompt gamma neutron activation analysis was used to demonstrate and quantify the bulk uptake of boron particulate and boric acid as a function of time in excised samples of live, human rheumatoid synovium. The results indicate that for both boron preparations a substantial amount of uptake occurs within the first hour of incubation, and the uptake increases gradually with time, over the next 24 h. For instance, in the samples incubated with boron particulate, the average bulk ^{10}B concentration at the end of the first hour was nearly 1000 ppm. At the end of 24 h, the average bulk ^{10}B concentration increased to roughly 2000 ppm. In the samples incubated with boric acid (90 ppm-^{10}B boronated incubation medium), the average bulk ^{10}B concentration at the end of the first hour was roughly 40 ppm, nearly half that of the incubation medium. At the end of 24 h, the average bulk ^{10}B concentration increased to roughly 50 ppm.

For the boron particulate experiments, variations associated with the measured concentrations in each of the 4 sample groups were seen to be high, $\approx$ 30-70%. Principal sources of the variations included difficulties in obtaining hearty explants of actively inflamed, human rheumatoid synovium and in ensuring that the dissected samples included an active layer of synovial lining cells. If the samples are not sufficiently active or if the layer is not included, then the uptake of boron particulate by the target cells (*i.e.*, the lining cells) clearly will be affected. Most of the uncertainty in the measured ^{10}B concentrations in the boron particulate experiments is believed to be due to these two problems. As a comparison, uncertainties associated with the

activation analysis of the samples are on the order of 10%, or less [99].

For the boric acid experiments, uncertainties associated with the measured concentrations are seen to be significantly smaller, $\approx$ 15%. In this case, the difficulties encountered in the boron particulate experiments are less important, since the uptake of boric acid relies on passive diffusion rather than active phagocytosis. As a consequence, it is less critical in the boric acid experiments for the synovial samples to be active or to include a layer of lining cells.

Neutron-induced alpha-track autoradiography

Neutron-induced alpha-track autoradiography was used in an attempt to examine the spatial distribution of ^{10}B uptake in samples of excised human rheumatoid synovium incubated with either boron particulate or boric acid. The results, unfortunately, did not reveal the desired information. Instead, virtually no alpha-particle tracks were seen on any of the CR 39 track-etch detectors.

For the boron particulate experiments, possible explanations of the result include the following. As described above, the uptake of particulate matter in synovium is the result of phagocytic absorption by the type-A lining cells and macrophages. If the synovial samples used were not sufficiently hearty or if an active layer of lining cells was not included, then the uptake of boron particulate by the synovium clearly would have been affected. Also, the 10 μm slice size was too small to allow some of the particles to be included in the slices. In this case, tracks may not have been visible because boron had not been absorbed or because some of the particulate had been removed during slicing.

For the boric acid experiments however, the above explanations are not relevant since the uptake of boric acid relies on passive diffusion and the size of the "particles" is too small for them to have been removed from the samples during slicing. Other possible explanations are as follows. First, the boronated incubation medium may not have been prepared as intended. Although unlikely, it is possible that boric acid was not added to the incubation medium. Second, Neutrons may not have been available at the sample position during irradiation. In the past, other researchers using the beam port position 1PH1 to examine the spatial distribution of ^{10}B in sliced tissue samples using neutron-induced alpha-track autoradiography also saw no tracks [116]. With the aid of gold foils, they determined that the thermal neutron flux at the sample position was substantially lower than it should have been and efforts were made to correct the correct the problem. Third, the etching techniques used may have been inadequate to transform stress point tracks to microscopically visible pits, *i.e.*, the etching time, temperature, and etchant strength may have been inadequate.

7.5 Conclusion

In this chapter, the uptake of ^{10}B in excised samples of human rheumatoid synovium was demonstrated and quantified. Prompt gamma neutron activation analysis was used to examine the temporal distribution of ^{10}B uptake in the samples. For both boron particulate and boric acid, substantial bulk uptake after 1 h of incubation was observed; and over the next 24 h, the uptake was shown to increase gradually.

Information regarding the spatial distribution of ^{10}B in the samples was not obtained. For the uptake of boron particulate, which is expected to be limited to type-A lining cells and macrophages (see Section 6.3.1), variations in the spatial distribution of ^{10}B in the samples are hypothesized to be quite large. High concentrations of ^{10}B are hypothesized to arise in the lining cells and macrophages, for instance, with very little, if any, ^{10}B in other cells of the sample. A bulk ^{10}B concentration of 1000 ppm thus may correspond to a synovial surface concentration of several 1000s of ppm, with little, or no, ^{10}B elsewhere in the sample. For the uptake of boric acid, on the other hand, a uniform spatial distribution of ^{10}B is hypothesized to arise throughout the entire synovium. Unfortunately, data supporting the hypotheses were not obtained.

Chapter 8

Conclusion

The aims of this thesis were: to evaluate beta-particle dosimetry in radiation synovectomy using Monte Carlo radiation transport simulation, experiments in joint phantoms, and experiments in the knees of cadavers; to provide a rationale for the use of the $^{10}B(n,\alpha)$ nuclear reaction to examine the pathology of rheumatoid arthritis; and to determine the temporal and spatial distribution of ^{10}B uptake in excised samples of live, human rheumatoid synovium.

Evaluating beta-particle dosimetry in radiation synovectomy is a difficult problem for a variety of reasons. The approach taken in this thesis was to evaluate the dosimetry in 3 different ways: through Monte Carlo simulation of radiation transport in a mathematical model of the rheumatoid joint, through experiments in joint phantoms using radiachromic film dosimeters and reactor-produced radionuclides, and through experiments in the knees of fresh, human cadavers using radiachromic film dosimeters and reactor-produced ^{165}Dy. Results of the evaluation are reviewed below.

Following the evaluation of beta-particle dosimetry in radiation synovectomy, the second half of this thesis was devoted to the use of the $^{10}B(n,\alpha)$ nuclear reaction to examine the pathology of rheumatoid arthritis. As described in Chapter 6, there is a variety of data which support the hypothesis that killing the surface layer of synovial lining cells in rheumatoid joints is sufficient to temporarily arrest the progression of rheumatoid arthritis in the joint and provide patients with symptomatic relief of the disease. The proposed approach is to use the $^{10}B(n,\alpha)$ nuclear reaction as a probe to determine whether killing the lining cells alone could arrest progression of rheumatoid arthritis, or whether killing the entire synovium is required. While the question itself was not answered in this thesis, necessary information regarding the uptake of ^{10}B in human rheumatoid synovium was obtained and is reviewed here.

8.1 Beta-particle Dosimetry in Radiation Synovectomy

Beta-particle dosimetry in rheumatoid synovial joints is a difficult problem for a variety of reasons. These include the physical difficulties associated with the beta-dosimetry of low-energy electrons in heterogeneous media and the biological and anatomical difficulties associated with the non-uniform distribution of lining cells in rheumatoid joints and the non-uniform distribution of radioactivity within them; leakage of radioactivity from the joint, which may be variable; area of the surface of the synovial membrane over which the administered activity is distributed, etc. [9]. The approach taken in these thesis was first to idealize the biological and anatomical factors since they are so highly variable and difficult to determine on a patient by patient basis. Then Monte Carlo calculations were coupled with experiments in joint phantoms and the knees of cadavers to address the physical difficulties and complete an accurate evaluation of the dosimetry for the idealized system.

8.1.1 Monte Carlo calculations

As described in Chapter 4, the evaluation began with a series of Monte Carlo calculations of beta dose distributions in a mathematical model of the treated joint. The Monte Carlo method has proved to be a powerful and versatile tool useful for solving a wide variety of problems. In particular, the method provides an economical and accurate technique for estimating absorbed dose distributions in irradiated media. With the aid of Monte Carlo, these distributions typically can be calculated for any source-to-target configuration, in any simulation geometry, and for any characterized radiation source. An added advantage of the method is that users of Monte Carlo codes also may have the option of "turning off" the simulation of certain types of interactions and manipulating geometry or material specifications, in order to investigate their individual contributions to dosimetry in the problem at hand.

Results of the Monte Carlo calculations completed in this thesis were presented as absorbed dose factors (cGy-cm^2/MBq-s) at depth in bone, articular cartilage, the fluid-filled joint capsule, and synovium, and can be used to extrapolate beta dose distributions in treated joints. Effects of the presence of bone in the joint and extension of the radiation source region (due to increased volumes of joint fluid and numbers of lining cells) on dosimetry also were evaluated. Radiation backscatter due to the presence of bone was seen to be minimal and not to contribute dose to the synovium. Extension of the source was seen to result in increases in synovial dose at depth and decreases in the bone surface dose. This finding was attributed to the fact that the increased numbers of lining cells resulted in spatial distributions of radioactivity deeper into the synovium, and thus away from bone.

The results of the evaluation are intended to provide guidance for clinicians concerned with radionuclide selection and the amount of radioactivity to administer in radiation synovectomy. Definite data on the absorbed dose required at depth in synovium for successful therapy have not been established. For a given areal concentration of injected radioactivity uniformly distributed throughout the joint capsule and along a surface layer of lining cells, however, absorbed dose to tissue (synovium), articular cartilage, and bone are easily estimated with the results shown in Figures 4-10 through 4-17.

Absorbed dose to the bone surface is particularly of interest since the International Commission on Radiation Protection has identified this tissue region as one of two principal radiosensitive targets to be protected in procedures involving bone irradiation [13]. Considering the fact that it may be necessary to kill only the surface layer of lining cells in rheumatoid joints to arrest the progression of rheumatoid arthritis and provide patients with symptomatic relief of the disease, use of the lower-energy beta-emitters (*e.g.*, ^{153}Sm, ^{165}Dy, ^{169}Er, and ^{186}Re) may be best in radiation synovectomy since these radionuclides present a significantly lower radiation hazard to bone than the higher-energy beta-emitters when administered in quantities sufficient to deliver therapeutic doses to the lining.

8.1.2 Experimental dosimetry

Next, evaluation of the dosimetry continued with a series of experiments conducted in joint phantoms and the knees of cadavers using radiachromic film dosimeters and reactor-produced radionuclides. The experiments were of interest because suitability of the **EGS4** Monte Carlo radiation transport code to evaluate the dosimetry of low-energy electrons (less than 2 MeV) in heterogeneous media has not been extensively tested.

As described in Chapter 3, the **EGS** code originally was developed to simulate high-energy electron and photon transport and only recently was modified to extend its useful range to include lower energies. Because of its high-energy origin, where forward scattering dominates, **EGS** has been described as suffering from a number of inherent "weaknesses" associated with the condensed history transport of low-energy electrons: multiple scattering according to the theory of Móliere, bremsstrahlung differential in energy only, and a simple treatment of low-energy electrons and photons, as compared with **ETRAN**. As a consequence, during recent years low-energy electron transport in **EGS4** has been improved, mainly through the inclusion of user-defined restrictions in step-sizes (variable name **ESTEPE**) to yield a more accurate system [63]. Other additions include electron transport down to 10s of keV, Rayleigh scattering, and bremsstrahlung differential in angle, as well as energy.

In the present work, the aim of the experiments was to obtain the measured data

necessary to verify the accuracy of the resulting EGS4 electron transport code package, *i.e.*, the default version of EGS4 with the inclusion of the improvements named above. Results of the experiments indicated that the Monte Carlo calculations of beta-particle dosimetry in a model of the rheumatoid joint were indeed accurate. Use of the EGS4 code to evaluate the dosimetry of low-energy electrons in heterogeneous media thus, in this case, is an acceptable application of the code.

8.2 Use of the $^{10}B(n,\alpha)$ Nuclear Reaction to Examine the Pathology of Rheumatoid Arthritis

In the remainder of this thesis, the focus was shifted from beta-particle dosimetry in radiation synovectomy to use of the $^{10}B(n,\alpha)$ nuclear reaction as a probe to examine the pathology of rheumatoid arthritis and determine whether killing the surface layer of lining cells in synovial joints is sufficient to arrest progression of the disease. The proposed approach is to use two different boron preparations (boron particulate and boric acid) to selectively boronate either the lining cells alone or the entire synovium. The $^{10}B(n,\alpha)$ nuclear reaction then can be used to selectively damage and kill only the boronated cells and their nearest neighbors. The $^{10}B(n,\alpha)$ nuclear reaction was chosen specifically because the range of the emitted particles is short, on the order of 10 μm, a distance which closely approximates the diameter of typical cells.

While the above question was not answered in this thesis, preliminary studies of ^{10}B uptake in excised samples of human rheumatoid synovium were completed. Prompt gamma neutron activation analysis of the samples indicated that substantial amounts of both boron preparations are absorbed within the first hour of incubation and the absorption increases gradually over the next 24 h. Neutron-induced alpha-track autoradiography to obtain spatial information regarding the distribution of ^{10}B in the samples was attempted but was unsuccessful. A number of possible explanations for the result were given in Chapter 7. In spite of the lack of spatial information, the preliminary studies did demonstrate the uptake of both boron particulate and boric acid in the synovial samples. And this observation represents the starting point for variety of *in vitro* and *in vivo* experiments aimed at answering the above question. The experiments are described below.

8.3 Recommendations for Future Work

Future work first should be aimed at repeating the neutron-induced alpha-track autoradiography experiments to examine the spatial distribution of boron particulate

and boric acid uptake by excised samples of human rheumatoid synovium. To avoid the problem of removing boron particulate from the samples during slicing, smaller particles (less than 10 μm in diameter) should be purchased and used in the experiments.

Once the autoradiography has been completed, then *in vitro* and *in vivo* experiments aimed at determining the thickness of rheumatoid synovium which must be removed to arrest progression of rheumatoid arthritis should be conducted. The possible development of neutron capture therapy as a novel treatment for rheumatoid arthritis also should be investigated. Each of these recommendations is discussed in this section.

8.3.1 Examining the pathology of rheumatoid arthritis

Work presented in the second half of this thesis was aimed at obtaining the preliminary data necessary to begin an examination of the pathology of rheumatoid arthritis using the ^{10}B(n,α) nuclear reaction as a probe. In particular, it is of interest to determine whether killing the surface layer of synovial lining cells in rheumatoid joints is sufficient to temporarily arrest the progression of rheumatoid arthritis, or whether killing the entire synovium is required.

In vitro experiments

Using boron particulate and boric acid, the effect of killing the lining cells alone versus the entire synovium could be examined *in vitro* using samples of live, human rheumatoid synovium obtained from the operating room. The procedure is as follows.

Samples of rheumatoid synovium are incubated for varying time periods with either boron particulate or boronated incubation medium (*i.e.*, boric acid and cell culture medium). After incubation, the samples are rinsed of any excess boron and irradiated with thermal neutrons to induce the ^{10}B(n,α) nuclear reaction.

Effects of the treatment are analyzed by co-incubating the treated samples with articular cartilage explants and later examining the explants for signs of cytokine-induced degradation. Articular cartilage explants co-incubated with active rheumatoid synovium have been shown to degrade over time, whereas explants co-incubated with either healthy synovium or inactivated synovium do not degrade [117]. The extent of cartilage degradation is quantified by measuring the proteoglycan content of the incubation medium. Articular cartilage dissolved *in vitro* by active rheumatoid synovium has been shown to release large amounts of proteoglycan into the incubation medium, and methods of quantifying the released amount are available [117]. Proteoglycan content of the incubation medium thus can be used to determine whether or not killing either the lining cells alone or the entire synovium arrests the destruction of articular cartilage *in vitro*. Provided *in vitro* experiments indicate that the

$^{10}B(n,\alpha)$ nuclear reaction can be used to arrest destruction of the articular cartilage explants, then *in vivo* experiments should be performed to verify the results in the intact organism.

Irradiation parameters. Monte Carlo radiation transport simulation could be used to determine the irradiation parameters required to deliver a therapeutic radiation dose to the boronated cells and their nearest neighbors without subjecting the remaining cells to an unacceptable radiation hazard.

Monte Carlo radiation transport simulation is used extensively in neutron capture therapy research (see below), both for the design of suitable neutron beams and the evaluation of radiation dosimetry. The Monte Carlo code most commonly used is **MCNP** (**M**onte **C**arlo for **N**eutron and **P**hoton **T**ransport) [118], which generally considered to be the most sophisticated code of its kind. Using **MCNP**, irradiation parameters, such as the irradiation time required to deliver a therapeutic absorbed dose to boronated cells for a given flux of thermal or epithermal neutrons, could be determined. Radiation dose imparted to other, non-boronated, cells also could be calculated.

In vivo experiments.

To verify *in vitro* results in the intact organism, an antigen-induced arthritis model in rabbits could be used [7, 8], again with boron particulate and boric acid, to examine the effect of killing the lining cells alone or the entire synovium. The procedure is as follows.

Mature, male New Zealand white rabbits are injected subcutaneously on two separate occasions with 10 0.1 ml shots of ovalbumin in Freund's complete adjuvant (10 mg/ml). The shots are delivered to various locations on the animal's back. The two sets of 10 injections are to be separated by 3 weeks [119].

Three weeks after the second set of injections, the animal is considered to be "sensitized," and a single 5 mg shot of ovalbumin directly into the knee is used to induce a monoarticular arthritis. The reaction develops within hours of induction, and acute synovial inflammation develops within 3 to 4 days. After 2 weeks, the antigen-induced arthritis model progresses to a chronic synovial inflammation. If left untreated, osteophyte formation and articular cartilage destruction are evident within 2 months [119].

Next, the two boron preparations are injected directly into the arthritic rabbit knees. After allowing optimal time for uptake and flushing the joints of excess boron, the boronated joints then are irradiated with an external beam of thermal neutrons. At various endpoints after irradiation, the rabbits are sacrificed, and their knees are dissected and histologically analyzed to assess the effects of killing either the lining cells alone or the entire synovium.

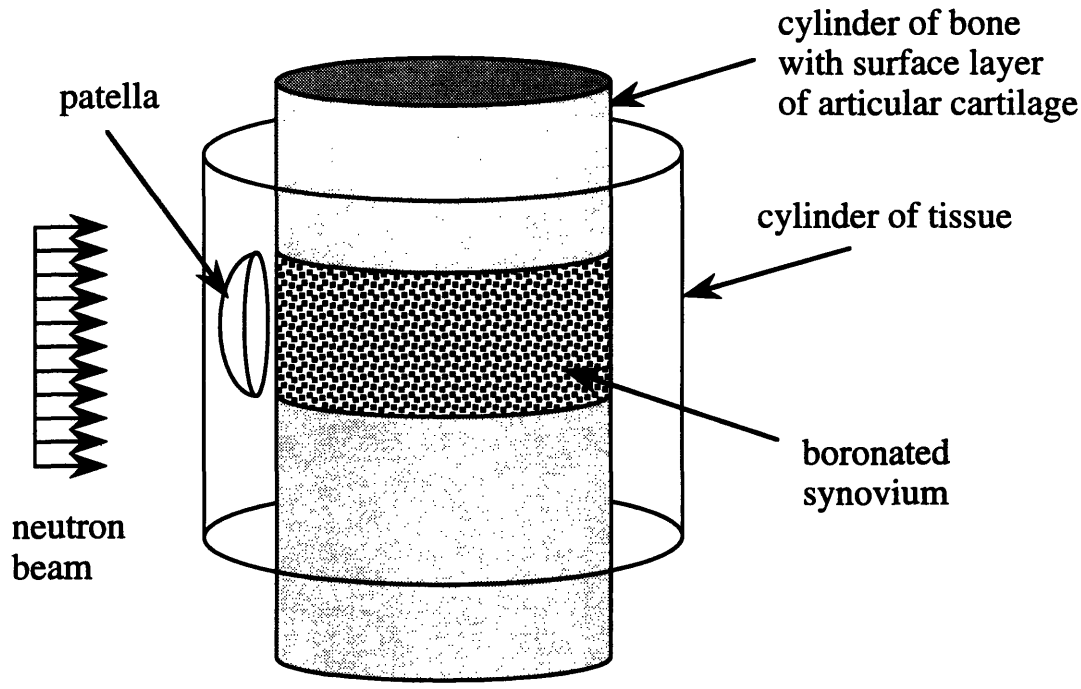

Figure 8-1: Mathematical joint model which could be used to evaluate various ir-radiation parameters required to deliver therapeutic synovial doses in as short an irradiation time as is possible.

Irradiation parameters. Again, MCNP could be used to determine the irradiation parameters required to optimize the resulting absorbed dose distributions in treated joints. A simple, cylindrical joint model (such as that shown in Fig. 8-1) could be used in the simulations. In the model, varying concentrations of ^{10}B could be specified in the boronated lining cells region and used to investigate its effect on absorbed dose distributions in the treated joint.

Neutron Capture Therapy for Rheumatoid Arthritis

If the above experiments indicate that the $^{10}B(n,\alpha)$ experiment can be used to arrest progression of rheumatoid arthritis, then development of neutron capture therapy as a novel treatment for the disease should be considered. Like radiation synovectomy, neutron capture therapy is a radiation therapy currently being developed for use in

the US.

Neutron capture therapy research has been aimed primarily at the destruction of brain tumors [120]. The approach has been to inject patients with stable boron compounds in solution which are carried though the patient by physiological pathways to the tumor site where they are expected to be preferentially absorbed and concentrated in the tumor. After allowing time for maximal tumor-to-healthy brain and tumor-to-blood ratios of boron concentration to be achieved, the tumor site then is irradiated with an external beam of thermal or epithermal neutrons. Epithermal neutron beams are sometimes used to account for the loss of neutrons in tissue, since they generally are required to penetrate several cm of brain before reaching the tumor. Upon reaching the boronated tumor, some of the neutrons are captured by ^{10}B nuclei and induce the (n,α) nuclear reaction. Both the particles released by the reaction are high LET, short range particles, *i.e.*, they give rise to closely spaced ionizations in sharply defined linear tracks that have a combined range in tissue of approximately 10-14 μm, a distance which is on the order of a typical cell diameter. As a result, they are capable of generating large amounts of radiation-induced damage in boronated tumor cells exposed to thermal neutrons, and their nearest neighbors. In general, this radiation damage is irreversible; and if the cell nucleus is involved, it eventually may lead to cell death.

A major advantage of the procedure is the fact that as soon as the neutron beam is shut off, the nuclear reactions are no longer induced and irradiation of the patient is complete. In patients treated with radionuclide therapy, on the other hand, irradiation is not as easily controlled. Radioactive emissions continue to irradiate these patients internally for as long as the radionuclide remains in the body. As mentioned in Section 2.4, the chief obstacle to wide-spread acceptance of radiation synovectomy is concern of excessive extraarticular irradiation due to leakage of injected radioactivity away from the joint. Internal irradiation of the liver, spleen, and draining inguinal lymph nodes are particularly of concern. While use of neutron capture therapy in the treatment rheumatoid arthritis would not avoid all extraarticular irradiation, concerns of subjecting patients to an unnecessary radiation hazard clearly could be reduced, particularly if the neutron beam is well collimated and aimed directly at the treated joint and if high concentrations of ^{10}B can be achieved in the target cells. The envisioned procedure is as follows.

8.3.2 Procedure

Rheumatoid joints to be treated with neutron capture therapy are injected with either boron particulate or boric acid in solution, depending on whether the lining cells alone or the entire synovium is to be killed. After allowing time for ^{10}B uptake by the target cells, any remaining boron solution is aspirated from the joint. The joint

capsule then is flushed once or twice to rinse the cartilagenous surfaces of any excess boron. Depending on the size of the joint, it is irradiated with an external beam of either thermal or epithermal neutrons. Desired radiobiological effects of the treatment include complete destruction of the cells responsible for promoting the progression of rheumatoid arthritis in the joint with the expectation that regenerated tissue will be free of disease for 2 to 5 years, and the pain and symptoms thereby alleviated, as in radiation synovectomy.

It is important to note that based on the preliminary studies of bulk ^{10}B uptake reported here, the ^{10}B concentrations obtained in the synovium (either the lining cells alone or the entire synovium) should be substantially higher (20 to 40 times higher) than those obtained in the treatment of brain tumors [120]. The irradiation time required to deliver a therapeutic dose to the synovium thus is expected to be significantly shorter (less than 5% of that required for the treatment of brain tumors). As a consequence, the radiation dose imparted to other, non-target, tissues by thermal neutron capture in H and N (see Section 6.3) would be substantially reduced (by 95% or more).

Bibliography

[1] Harbert JC. *Nuclear Medicine Therapy.* Thieme Medical, New York, 1987.

[2] Webb FWS, Lowe J, and Bluestone R. Uptake of colloidal radioactive yttrium by synovial membrane. *Ann Rheum Dis*, 28:300–302, 1969.

[3] Topp JR and Cross EG. The treatment of persistent knee effusions with intra-articular radioactive gold. *CMA J*, 102:709–714, 1970.

[4] Winston MA, Bluestone R, Cracchiolo A, and Blahd WH. Radioisotope synovectomy with ^{32}P-chromic phosphate: kinetic studies. *J Nucl Med*, 14:886–889, 1973.

[5] Bowen BM, Darracott J, Garnett ES, and Tomlinson RH. Yttrium-90 citrate colloid for radioisotope synovectomy. *Am J Hosp Pharm*, 32:1027–1030, 1975.

[6] National Council on Radiation Protection and Measurements. *NCRP-108: Conceptual Basis for Calculations of Absorbed-dose Distributions*, 1991.

[7] Shortkroff S, Jones AG, and Sledge CB. Radiation synovectomy. In *Advances in Metals in Medicine*, volume 1, pages 155–186. JAI Press, 1993.

[8] Deutsch E, Brodack JW, and Deutsch KF. Radiation synovectomy revisited. *Eur J Nucl Med*, 20:1113–1127, 1993.

[9] Husak V, Wiederman M, and Kral M. Absorbed dose due to beta-rays from radioactive colloids in radiation synovectomy. *Phys Med Bio*, 18:848–854, 1973.

[10] Johnson LS and Yanch JC. Absorbed dose profiles for radionuclides of frequent use in radiation synovectomy. *Arthritis Rheum*, 34:1521–1530, 1991.

[11] Johnson LS and Yanch JC. Calculation of beta dosimetry in radiation synovectomy using Monte Carlo simulation (EGS4). *Med Phys*, 20:747–754, 1993.

[12] Berger MJ. Distribution of absorbed dose around point sources of electrons and beta particles in water and other media. *J Nucl Med*, 12:NM/MIRD Pamphlet 7, 1971.

[13] International Commission on Radiation Protection. *ICRP-26: Recommendations of the ICRP*, 1977.

[14] Prestwich WV, Nunes J, and Kwok CS. Beta dose point kernels for radionuclides of potential use in radioimmunotherapy. *J Nucl Med*, 30:1036–1046, 1989.

[15] Simpkin DJ and Mackie TR. EGS4 Monte Carlo determination of the beta dose kernel in water. *Med Phys*, 17:179–186, 1990.

[16] Stevens A and Lowe J. *Histology.* Gower Med. Pub., New York, 1992.

[17] Private communication with S Shortkroff.

[18] Private communication with Dr C Reiners.

[19] Krstić RV. *Human Microscopic Anatomy.* Springer-Verlag, New York, 1991.

[20] Cotran RS, Kumar V, and Robbins SL. *Robbins Pathologic Basis of Disease.* WB Saunders, Philadelphia, 4th edition, 1989.

[21] Harris ED. Rheumatoid arthritis, pathophysiology and implications for therapy. *N Engl J Med*, 322:1277–1289, 1993.

[22] Arnett FC, Edworthy SM, and Bloch DA. American Rheumatism Association 1987 revised criteria for the classification of rheumatoid arthritis. *Arthritis Rheum*, 31:315–324, 1988.

[23] Lipsky PE. Rheumatoid arthritis. In Petersdorf RG, editor, *Harrison's Principles of Internal Medicine*, pages 1437–1443. McGraw-Hill, New York, 1990.

[24] Mori M. A review of knee joint synovectomy in rheumatoid arthritis with theoretical and technical considerations. *Ann Chir Gynaecol*, 74:40–47, 1985.

[25] English RJ, Zalutsky J, Venkatesan P, and Sledge CB. Therapeutic application of dysprosium-165 FHMA in the treatment of rheumtoid knee effusions. *J Nucl Med Tech*, 14:18–20, 1986.

[26] Sledge CB, Zuckerman JD, Zalutsky MR, Atcher RW, Shortkroff S, Lionberger DR, Rose HA, Hurson BJ, Lankenner PA, Anderson RJ, and Bloomer WA. Treatment of rheumatoid synovitis of the knee with intraarticular injection of dysprosium-165 ferric hydroxide macroaggregates. *Arth Rheum*, 69:153–159, 1986.

[27] Vella M, Zuckerman JD, Shortkroff S, Venkatesan P, and Sledge CB. Repeat radiation synovectomy with dysprosium-165 ferric hydroxide macroaggregates in rheumatoid knees unresponsive to initial injection. *Arthritis Rheum*, 31:789–792, 1988.

[28] Noble J, Jones AG, Davis MA, Sledge CB, Kramer RI, and Livni E. Leakage of radioactive particle systems from a synovial joint studied with a gamma camera: its application to radiation synovectomy. *J Bone Joint Surg Am*, 65:381–389, 1983.

[29] Sledge CB, Noble J, Hnatowich DJ, Kramer R, and Shortkroff S. Experimental radiation synovectomy by 165-Dy ferric hydroxide macroaggregate. *Arthritis Rheum*, 20:1334–1342, 1977.

[30] Shortkroff S, Mahmood A, Sledge CB, Jones AG, Brodack JW, Chinen LK, Deutsch E, and Deutsch KF. Studies on Ho-166 labeled hydroxyapatite: a new agent for radiation synovectomy. *J Nucl Med*, 33:937, 1992.

[31] Brodack JW, Chinen LK, Deutsch E, and Deutsch KF. Studies on the radiolabeling of hydroxyapatite particles for use as radiation synovectomy agents. *J Nucl Med*, 33:980, 1992.

[32] Fellinger K and Schmid J. Die Lokale Behandlung der rheumatischen Erkrankungen. *Wien Z Inn Med*, 33:351, 1952.

[33] Ansell BM, Crook A, Mallard JR, and Bywaters EGL. Evaluation of intra-articular colloidal gold Au-198 in the treatment of persistent knee effusions. *Ann Rheum Dis*, 22:435–439, 1963.

[34] Virkkunen M, Krusius FE, and Heiskanen T. Experiences of intra-articular administration of radioactive gold. *Acta Rheum Scand*, 13:81–91, 1967.

[35] Ahlberg A, Mikulowsky P, and Odelberg-Johnson O. Intra-articular injection of radioactive gold in treatment of chronic synovial effusion of the knee. *Acta Rheum Scand*, 15:81–89, 1969.

[36] Prichard HL, Bridgman MB, and Bleehen NM. An investigation of radioactive yttrium for the treatment of chronic knee effusions. *Br J Radiol*, 43:466–470, 1970.

[37] Williams ED, Caughey DE, Hurley PJ, and John MB. Distribution of yttrium 90 ferric hydroxide colloid and gold 198 colloid after injection into knee. *Ann Rheum Dis*, 35:516–520, 1976.

[38] Oka M and Hypen M. Radiation synovectomy: results in rheumatoid knee effusions treated with radioactive yttrium. *Scand J Rheum*, 3:33–38, 1974.

[39] Menkes CJ, Aignan M, and Galmiche B. Le traitement des rhumatismes par les synoviortheses. *Rheumatologie*, 2:61, 1971.

[40] Oka M, Rekonen A, Ruotsi A, and Seppala O. Intraarticular injection of Y-90 resin colloid in the treatment of rheumatoid knee joint effusions. *Acta Rheum Scand*, 17:148–160, 1971.

[41] Onetti CM, Gutierrez E, Hliba E, and Aguirre CR. Synoviorthesis with ^{32}P-colloidal chromic phosphate in rheumatoid arthritis—clinical, histopathologic, and arthrographic changes. *J Rheum*, 9:229–238, 1982.

[42] Zuckerman JD, Sledge CB, Shortkroff S, and Venkatesan P. Treatment of rheumatoid arthritis using radiopharmaceuticals. *Int J Radiat Appl Instrum Part B*, 14:211–218, 1987.

[43] Sledge CB, Zuckerman JD, Shortkroff S, Zalutsky MR, Venkatesan P, Snyder MA, and Barret WP. Synovectomy of the rheumatoid knee using intraarticular injection of dysprosium-165 ferric hydroxide macroaggregates. *J Bone Joint Surg Am*, 69:970–975, 1987.

[44] William ED, Caughey DE, Hurley PJ, and John MB. Distribution of yttrium-90 ferric hydroxide colloid and gold-198 after injection into knee. *Ann Rheum Dis*, 35:516–520, 1976.

[45] Kolarz G and Bergmann H. Body radiation dosage after synoviorthesis. In Kolarz G and Thumb N, editors, *Methods of Nuclear Medicine in Rheumatology*, pages 183–219. Schattauer, New York, 1982.

[46] Ingrand J. Characteristics of radioisotopes for intra-articular therapy. *Ann Rheum Dis*, 32 Suppl:3–9, 1973.

[47] Cross WG, Ing H, Freedman O, and Mainville J. *AECL-7617: Tables of Beta-ray Dose Distributions in Water, Air, and Other Media.* Chalk River Nuclear Laboratories, Ontario, Canada, 1982.

[48] Berger MJ. Distribution of absorbed dose around point sources of electrons and beta particles in water and other media. *J Nucl Med*, 12:MIRD Pamphlet No. 7, 1971.

[49] McCracken DD. The Monte Carlo method. *Scientific American*, 192:90–96, 1955.

[50] Raeside DE. Monte Carlo principles and applications. *Phys Med Bio*, 21:181–197, 1976.

[51] Wood J. *Computational Methods in Reactor Shielding.* Pergamon Press, New York, 1982.

[52] Jansson B. *Random Number Generators.* Almqvist and Wiksell, Stockholm, 1966.

[53] Naylor TH, Balintfy JL, Burdick DS, and Chu K. *Computer Simulation Techniques.* Wiley, New York, 1966.

[54] Nelson WR, Hirayama H, and Rogers DWO. *SLAC-265: The EGS4 Code System.* Stanford Linear Accelerator Center, Stanford, CA, 1985.

[55] Berger MJ and Seltzer SM. *NBS 9836 and 9837: Electron and Photon Transport Programs: I. Introduction and Notes on Program DATAPAC 4; II. Notes on Program ETRAN-15.* National Bureau of Standards, Gaithersburg, MD, 1968.

[56] Halbleib JA and Mehlhorn TA. *Sand 84-0573: ITS, The Integrated TIGER Series of Coupled Electron-Photon Monte Carlo Transport Codes.* Sandia National Laboratory, Sandia, 1984.

[57] Rogers DWO and Bielajew AF. A comparison of EGS and ETRAN. In Jenkins TM, Nelson WR, and Rindi A, editors, *Monte Carlo Transport of Electrons and Photons*, pages 323–342. Plenum Press, New York, 1987.

[58] Goudsmit S and Saunderson JL. Multiple scattering of electrons. *Phys Rev*, 57:568, 1940.

[59] Moliére G. Theorie der Streuung schneller geladener Teilchen I: Einzelstreuung am abgeschirmten Coulombfeld. *Z Naturforsch*, 2A:133, 1947.

[60] Moliére G. Theorie der Streuung schneller geladener Teilchen II: Mehrfach- und Vielfachstreuung. *Z Naturforsch*, 3A:78, 1947.

[61] Bethe HA. Moliére's theory of multiple scattering. *Phys Rev*, 89:1256, 1953.

[62] Berger MJ. Monte Carlo calculation of the penetration and diffusion of fast charged particles. In Alder B, Fernbach S, and Rotenberg M, editors, *Methods in Computational Physics*, volume 1, pages 135–215. Academic Press, New York, 1963.

[63] Rogers DWO. Low-energy electron transport with EGS. *Nucl Instr Meth*, A227:535–548, 1984.

[64] Bielajew AF and Rogers DWO. PRESTA: the parameter reduced electron-step transport algorithm for electron Monte Carlo transport. *Nucl Instr Meth*, B18:165–181, 1987.

[65] Møller C. Zur Theorie des Durchgang schneller Elektronen durch Materie. *Ann Physik*, 14:568, 1932.

[66] Bethe HA. Theory of passage of swift corpuscular rays through matter. *Ann Physik*, 5:325, 1930.

[67] Bloch F. Stopping power of atoms with several electrons. *Z für Physik*, 81:363, 1933.

[68] Sternheimer RM. Density effect for the ionization loss of charged particles. *Phys Rev*, 145:247, 1966.

[69] Sternheimer RM. Density effect for the ionization loss of charged particles. II. *Phys Rev*, 164:349, 1967.

[70] International Commission on Radiation Units and Measurements. *ICRU-37: Stopping Powers for Electrons and Positrons*, 1984.

[71] Rogers DWO, Duane S, Bielajew AF, and Nelson WR. *PIRS-0177: Use of ICRU-37 Radiative Stopping Powers in the EGS4 System.* National Research Council of Canada, Ottawa, Canada, 1989.

[72] Berger MJ. ETRAN–experimental benchmarks. In Jenkins TM, Nelson WR, and Rindi A, editors, *Monte Carlo Transport of Electrons and Photons*, pages 183–219. Plenum Press, New York, 1987.

[73] Seltzer SM. Electron-photon Monte Carlo calculations: the ETRAN code. *Int J Radiat Appl Instrum*, A42:917–941, 1991.

[74] Bethe HA and Heitler W. On the stopping of fast particles and on the creation of positive electrons. *Proc Roy Soc*, A146:83, 1934.

[75] Davies H, Bethe HA, and Maximon. Theory of bremsstrahlung and pair production. *Phys Rev*, 93:788, 1954.

[76] Butcher JC and Messel H. Electron number distribution in electron-photon showers in air and aluminum absorbers. *Nucl Phys*, 20:15, 1960.

[77] Koch HW and Motz JW. Bremsstrahlung cross section formulas and related data. *Rev Mod Phys*, 31:920, 1959.

[78] Bielajew AF, Mohan R, and Chui CS. *PIRS-0203: Improved bremsstrahlung photon angular sampling in the EGS4 code system.* National Research Council of Canada, Ottawa, Canada, 1989.

[79] Johnson LS and Palmer M. *WCBICL-2: LEGS1.4 User Code.* Whitaker College Biomedical Imaging and Computation Laboratory, Cambridge, MA, 1993.

[80] Finerty JC and Cowdry EV. *A Textbook of Histology.* Lea and Feabiger, Philadelphia, 1960.

[81] International Commission on Radiation Units and Measurements. *ICRU-44: Tissue Substitutes in Radiation Dosimetry and Measurement*, 1989.

[82] Hogan OH, Zigman PE, and Mackin JL. *Beta Spectra II. Spectra of Individual Negatron Emitters.* United States Radiological Defense Laboratory, San Francisco, 1964.

[83] Loevinger R and Berman M. A revised schema for calculating the absorbed dose from biologically distributed radionuclides. *J Nucl Med*, 16:NM/MIRD Pamphlet 1, 1975.

[84] Constantinou C, Attix FH, and Paliwal BR. A solid water phantom material for radiotherapy x-ray and γ-ray beam calibrations. *Med Phys*, 9:436–441, 1982.

[85] Constantinou C. *Tissue Substitutes for Particulate Radiations and Their Use in Radiation Dosimetry and Radiotherapy.* Phd thesis, University of London, 1978.

[86] Nunes J, Prestwich WV, and Kwok CS. Experimental determination of ^{32}P dose backscatter factors at and near soft-tissue boundaries. *Med Phys*, 20:223–231, 1993.

[87] Kwok CS, Irfan M, Woo MK, and Prestwich WV. Effect of tissue inhomogeneity on beta dose distribution of ^{32}P. *Med Phys*, 14:98–104, 1987.

[88] Chalkley L. Phototrophy. *Chem Rev*, 6:217, 1929.

[89] McLaughlin WL and Chalkley L. Measurement of radiation dose distributions with photochromic materials. *Radiology*, 84:124, 1965.

[90] Humpherys KC and Kantz AD. Radiachromic: a radiation-monitoring system. *Radiat Phys Chem*, 9:737–747, 1977.

[91] Kwok CS, Bialobzyski PJ, and Yu SK. Effect of tissue inhomogeneity on dose distribution of continuous activity of low-energy electrons in bone marrow cavities with different topologies. *Med Phys*, 18:533–541, 1991.

[92] Farahani M, Eichmiller FC, and McLaughlin WL. Measurement of absorbed doses near metal and dental material interfaces irradiated by x- and gamma-ray therapy beams. *Phys Med Bio*, 35:369–385, 1990.

[93] Johnson JC, Langhorst SM, Loyalka SK, Volkert WA, and Ketrring AR. Calculation of radiation dose at a bone-to-marrow interface using Monte Carlo modeling techniques (EGS4). *J Nucl Med*, 33:623–628, 1992.

[94] Ahlberg A, Mikulowsky P, and Odelberg-Johnson O. Dosimetry considerations of bone-seeking radionuclides for marrow ablation. *Med Phys*, 20:1089–1096, 1993.

[95] Hnatowich DJ, Kramer RI, Sledge CB, Noble J, and Shortkroff S. Dysprosium-165 ferric hydroxide macroaggregates for radiation synovectomy. *J Nucl Med*, 19:303–308, 1978.

[96] Will R, Laing B, Edelman J, Lovegrove F, and Surveyor I. Comparison of two ytrrium-90 regimens in inflammatory and osteoarthropathies. *Ann Rheum Dis*, 51:262–265, 1992.

[97] Tananka S, Ueo T, and Ohnishi N. Clinical effects of radiation synovectomy. *J West Pac Orthop Assoc*, 15:83–92, 1978.

[98] Javid M, Brownell GL, and Sweet WH. The possible use of neutron-capture isotopes such as boron-10 in the treatment of neoplasms. II. computation of the radiation energy and estimates of effects in normal and neoplastic brain. *J Clin Invest*, 31:603–610, 1952.

[99] Tölgyessy J and Kryš M. *Radioanalytical Chemistry.* John Wiley and Sons, New York, 1989.

[100] Harling OK, Chabeuf JM, Lambert F, and Yasuda G. A prompt gamma neutron activation analysis facility using a diffracted beam. *Nucl Instr Meth*, B 83:557–562, 1993.

[101] Fleischer RL and Price PB. *Science*, 140:1221, 1963.

[102] Fairchild RG, Gabel D, Laster BH, Greenberg D, Kiszenick W, and Micca PL. Microanalytical techniques for boron analysis using the ^{10}b(n,α)^{7}li reaction. *Med Phys*, 13:50–56, 1986.

[103] Failey MP, Anderson DL, Zoller WH, Gordon GE, and Lindstrom RM. *Anal Chem*, 51:2209, 1979.

[104] Gladney ES, Jurney BT, and Curtis DB. *Anal Chem*, 48:271, 1976.

[105] Rogers A. *Techniques of Autoradiography.* Elsivier Scientific, New York, 1973.

[106] Boyd GA. *Autoradiography in Biology and Medicine.* Academic Press, New York, 1973.

[107] Gahan PB. *Autoradiography for Biologists.* Academic Press, New York, 1972.

[108] Shih JA and Brugger RM. Neutron autoradiography of trace amounts of gadolinium. *Nucl Tech*, 98:217–223, 1991.

[109] Zervas NT and Soloway AH. The microscopic distribution of water soluble compounds by autoradiography. *J Neuropathol Exp Neurol*, 23:151–155, 1964.

[110] Mayr G, Bruner HD, and Brucer M. Boron detection in tissues using the (n,α) reaction. *Nucleonics*, 11:Oct 21, 1953.

[111] Abe M, Amano K, Kitamura K, Tateishi J, and Hatanaka H. Boron distribution analysis by alpha-autoradiography. *J Nucl Med*, 27:677–684, 1986.

[112] Thellier M, Laurent-Pettersson M, Martini F, and Ripoll C. Biological applications of neutron capture radiography. *Neutron News*, 2:26–30, 1991.

[113] Durani SA and Bull RK. *Solid State Nuclear Track Detection: Principles, Methods and Applications.* Plenum, New York, 1987.

[114] Gabel D, Holstein H, Larsson B, Gille L, Ericson G, Sacker D, Som P, and Fairchild RG. Quantitative neutron capture radiography for studying the biodistribution of tumour-seeking boron-containing compounds. *Cancer Res*, 47:5451–5454, 1987.

[115] Larsson B, Gabel D, and Borner HG. *Phys Med Bio*, 29:361, 1984.

[116] Amano K and Sweet WH. Alpha-autoradiography of ^{10}b compound distribution in tissue by use of superimposition. *Nippon Acta Radiol*, 33:267–272, 1973.

[117] Private communication with Dr G Solares.

[118] Yodlowski ML, Hubbard JR, Kispert J, Keller K, Sledge CB, and Steinberg JJ. Antibody to interleukin 1 inhibits the cartilage degradative and thymocyte proliferative actions of rheumatoid synovial culture medium. *J Rheumatol*, 17:1600–1607, 1990.

[119] Thompson WL. *LA 7396-M: MCNP–A General Monte Carlo Code for Neutron and Photon Transport. A Summary.* Los Alamos National Laboratory, Los Alamos, NM, 1979.

[120] Dumonde DC and Glynn LE. The production of arthritis in rabbits by an immunological reaction to fibrin. *Br J Exp Pathol*, 43:373–383, 1962.

[121] Barth RF, Soloway AH, and Fairchild RG. Boron neutron capture therapy of cancer. *Cancer Res*, 50:1061–1070, 1990.